Transport of Polarized helions in Injector Synchrotrons for the future electron-ion collider project at the Brookhaven National Laboratory

Kiel Hock

THÈSE

Pour obtenir le grade de

DOCTEUR DE L'UNIVERSITÉ GRENOBLE ALPES

Spécialité : Physique Subatomique et Astroparticules

Arrêté ministériel : 25 mai 2016

Présentée par

Kiel HOCK

Thèse dirigée par **François MÉOT,** Ingénieur-HDR à BNL
et codirigée par **Johann COLLOT**, Professeur à l'UGA
et co-encadrée par **Huang HAIXIN**, Physicien à BNL
préparée au sein du **Laboratoire National de Brookhaven**
dans **l'École Doctorale de Physique de Grenoble**

Transport d'hélium-3 polarisé dans les injecteurs synchrotrons pour le projet de collisionneur électrons-ions (EIC) au Laboratoire National de Brookhaven

Transport of Polarized helions in Injector Synchrotrons for the future electron-ion collider project at the Brookhaven National Laboratory

Thèse soutenue publiquement le **8 octobre 2021**,
devant le jury composé de :

Monsieur Christophe Furget
PROFESSEUR DES UNIVERSITÉS, Université Grenoble Alpes, Président
Monsieur Philippe Piot
PROFESSEUR DES UNIVERSITÉS, Northern Illinois University, Rapporteur
Monsieur Andreas Lehrach
PROFESSEUR Associé, RWTH Aachen University, Rapporteur
Monsieur Chuyu Liu
PHYSICIEN, Brookhaven National Laboratory, Examinateur
Monsieur Patrick Puzo
PROFESSEUR DES UNIVERSITÉS, Université Paris Saclay, Examinateur

Abstract

Polarized helion collisions are part of future physics programs at the EIC [1, 2]. The spin of helion is prepared to provide a polarized neutron bound with an unpolarized proton pair. This spin state facilitates polarized neutron collisions to allow further study of the spin contribution of quarks to the total angular momentum of the nucleon, and will play a part in helping solve the Spin Puzzle [3]. With an anomolous magnetic moment 2.34 times larger than that of protons, helions will encounter many more depolarizing resonances as they are accelerated through to the top collision energy. To maximize polarization transmission through the RHIC injectors it is desired to extract helions from the AGS Booster at $|G\gamma| = 10.5$, avoiding the $|G\gamma| = 0 + \nu_y$ depolarizing resonance in AGS and minimizing optical defects from the two AGS partial snakes, where $|G\gamma|$ is the spin tune.

Extraction at $|G\gamma| = 10.5$ will cause helions to cross the $|G\gamma|$=5, 6, 7, 8, 9, and 10 imperfection resonances, and $|G\gamma| = 12 - \nu_y$ and $|G\gamma| = 6 + \nu_y$ intrinsic resonances. An AC dipole has been installed in the AGS Booster to induce a spin flip through the two intrinsic resonances. An AC dipole enhances the strength of the intrinsic resonances by inducing vertical betatron oscillations that cause large vertical excursion of the bunch through the horizontal fields of the quadrupoles. An experimental study with Au beam confirmed that the available aperture is sufficient to accommodate these large amplitude vertical betatron oscillations.

Simulations for helions crossing the aforementioned resonances have been performed and display the effectiveness of the AC dipole at spin-flipping in the Booster. Due to the rapid acceleration of the Booster, the AC dipole tune will change as much as 0.0028 over the course of an AC dipole cycle, which changes the amplitude of these betatron oscillations over the course of the cycle. Through simulation, it is shown that the varying betatron amplitude does not dilute the spin-flip efficiency of the AC dipole. Sextupoles are used to provide control over the tune spread, whereas RF-dual harmonics are used to control the bunch length, and to reduce the momentum spread.

Polarized protons can be used to cross an intrinsic resonance which has similar machine requirements to helions which provides a convenient proof of principle experiment

for the AGS Booster AC dipole while the polarized helion source is being constructed. Beam dynamics studies were performed with unpolarized protons and showed a strong agreement with theory and simulations. These studies also showed that protons could be driven at the maximum amplitude allowed by the power amplifier without generating beam loss with nominal separation between AC dipole and betatron tunes, and resulted in no dilution of the emittance.

Experimental results from polarized protons crossing $|G\gamma| = 0 + \nu_y$ showed the strength of the resonance matches those from the numerical model. However, due to feed down in the sextupoles at extraction, the coherent amplitude of the driven oscillations of the protons was reduced. This reduced amplitude required a reduction in the vertical beam size to reach a full spin-flip through the resonance. The model was adjusted to reflect the experiment and showed good agreement which had departed from the idealized model. Given the results from the experiment, the Booster model is confirmed to be accurate and thus the AC dipole will be able to spin-flip helions through the two intrinsic resonances.

Acknowledgements

I would like to thank my director François Méot who has not only been a great mentor, but also pushed me to work at my highest level. My co-director, Johann Collot, who closely monitored my progress and provided fruitful recommendations on my technical writing. My co-adviser, Haixin Huang, who provided his knowledge and experiences with the AGS AC dipole, and was also available to assist when I was working operations shifts.

Andreas Lehrach and Philippe Piot for taking the time to review my thesis, to provide their suggestions, and to attend the defense. Thank you to the President, Christophe Furget, and the jurors Chuyu Liu and Patrick Puzo for offering their time to participate as members of my defense board.

Thomas Roser who supported the work and always provided knowledge from his experience with the AGS AC dipole. Wolfram Fischer support for this project was unwavering and took great effort in ensuring the AC dipole experiment would work in seamlessly with the operation of the RHIC complex. Joseph Tuozzolo for overseeing the mechanical design and installation.

Keith Zeno who is a true master of the injectors. Like many other experiments, the positive results documented in this thesis are owed to Keith's meticulous setup work. Vincent Schoefer for his participation in the 24/7 study of the Booster AC dipole. Anatoli Zelenski who prepared the OPPIS source ahead of schedule for the AC dipole studies in the Booster.

Nicholaos Tsoupas who not only did numerical modelling for the AC dipole design, but also provided his knowledge and experience in accelerators during the development of the Zgoubi Booster model.

To my former group leader, Peter Ingrassia, who was incredibly supportive of my pursuits and endeavors. Greg Marr, my current group leader, who picked up Peter's reigns.

Matthew Panniccia for his development of the upgraded Booster BPM system and assistance in commissioning the system with the upgraded tune meters. Peter Oddo for his electrical design of the AC dipole. Anthony Curcio for installation and testing of both

the BPM and AC dipole.

And to my wife, Caroline.

List of Symbols

- α, resonance crossing speed.
- α_x/α_y, horizontal and vertical alpha functions.
- β, ratio of velocity to the speed of light.
- β_x/β_y, horizontal and vertical beta functions.
- γ, Lorentz factor.
- γ_x/γ_y, horizontal and vertical gamma functions.
- δ_m, resonance proximity parameter.
- δ_p, the relative momentum error, $(p - p_o)/p_o$.
- ϵ_K, resonance strength.
- ε, Courant-Snyder invariant.
- η, slip factor.
- λ, wavelength.
- θ, bend angle from magnet.
- μ, magnetic moment.
- ν_x/ν_y, horizontal and vertical betatron tunes.
- ν_m, tune modulated by AC dipole.
- ν_s, spin tune.
- Q_x/Q_y, horizontal and vertical fractional betatron tunes.
- ξ_x/ξ_y, horizontal and vertical chromaticities.
- ρ, radius of curvature.
- σ_x/σ_y, horizontal and vertical beam widths.
- ϕ_{RF}, RF phase.
- ϕ_x/ϕ_y, horizontal and vertical betatron phase advances.
- χ_c/χ_w, spin rotation angle from cold and warm snakes in % of 180^o.
- $\vec{B}$, magnetic field.
- C, ring circumference.
- c, speed of light.
- $\vec{E}$, electric field.
- f_{rev}, revolution frequency.
- f_{RF}, RF frequency.
- G, anomolous g-factor.
- g, Landé g-factor.
- h, harmonic number.
- h_{RF}, RF harmonic number.
- $\hbar$, reduced Planck constant.
- $\mathcal{L}$, Luminosity.
- N_1/N_2, number of particles in colliding bunch #1 and bunch #2.
- N_b, number of bunches.
- $N_\uparrow/N_\downarrow$, number of particles with spin up and spin down.
- m_o, rest mass.
- M_n, transport matrix of element n.
- P, periodicity of the accelerator.
- p, particle momentum.
- p_o, reference momentum.
- Q_s, synchrotron tune.
- q, particle charge.
- r, radius of accelerator.
- $\vec{S}$, the spin vector.
- u, nucleon count.
- V_{RF}, RF cavity voltage.
- v, particle velocity.

Contents

List of Figures

List of Tables

Chapter 1

Introduction

The first signs of a discrete nuclear angular momentum were seen by Alfred Landé in 1921, although at the time he did not know to describe the splitting of energy levels in a magnetic field, known as the Zeeman effect [4]. His model for the Zeeman effect using angular momentum was developed in 1925. In 1922, the Stern-Gerlach experiment showed that this angular momentum was discrete [5]. Discrete angular momentum known as spin was proposed by Uhlenbeck and Goudsmith [6]. The quantum mechanical formulation of nuclear spin was developed by Pauli after the concept was introduced, and eventually spin became the fourth quantum number [6]. Applications of spin encompass various fields including medical imaging, biological and chemical sciences, as well as atomic and nuclear physics.

The proton is a spin-1/2 particle that has spin values of $\pm\hbar/2$. The proton is comprised of valence quarks (two up quarks and one down quark), pairs of sea quarks, and gluons; all of which contribute to the total spin of the proton. Understanding how the spin of quarks and gluons contribute to the spin of the proton, or other hadrons such as helions, at various energies is the motivation for polarized beam physics programs at the Relativistic Heavy Ion Collider (RHIC). The data from RHIC, and expected data from the Electron Ion Collider (EIC), contribute to solving the "Proton Spin Puzzle" [3].

Polarized helion collisions are desired for polarized spin studies at RHIC and the future EIC project [1]. These helions will have a prepared spin state that produces a

polarized neutron bound to unpolarized proton pairs. The helions and their neutrons are also spin-1/2 particles, facilitating collisions of polarized neutrons to further study the origins of spin and the contribution of gluons and quarks spins to the total nuclear angular momentum of the neutron, since the proton and neutron are both spin-1/2 particles but have a different valence quark composition (up up down, and up down down). The polarized neutron data may help better understand the nucleon spin puzzle. The error associated with these measurements will be greatly reduced with the EIC [7].

This thesis provides an overview of the transport of polarized helions in the RHIC injector complex with an emphasis on the Booster. Polarization transport in the Booster will utilize the AC dipole to induce a 100% spin flip through intrinsic resonances and orbit harmonic correctors for 100% transmission through imperfection resonances, while quantifying the dynamics of increasing the AGS injection energy. A spin-flip is the act of enhancing a strong resonance so instead of having a partial rotation from the vertical axis and resulting in polarization loss, the spin will rotate completely to avoid any loss in polarization.

1.1 RHIC and EIC Accelerator Complex

RHIC was commissioned in 2000 and is the only polarized proton collider. The RHIC accelerator complex consists of four beam sources, two injector synchrotrons, and RHIC itself. The layout of the RHIC complex is shown in Fig. 1.1 (top). The EIC will be built on the present RHIC accelerator complex, using the same injectors and having an electron storage ring built in the RHIC tunnels which will operate as a collider ring as seen in Fig. 1.1 (bottom) [2]. Of the three beam sources, ions are available from the Electron Beam Ion Source (EBIS) and the Tandem Van de Graaff accelerators. The other two sources produce H^{-1} ions and are available by the Optically Pumped Polarized Ion Source (OPPIS) or the high-intensity source via the 200 MeV LINAC [8]. The beams produced by these sources are injected at various energies (depending on the source being used) into the Booster which then accelerates particles to extraction into

the Alternating Gradient Synchrotron (AGS) or for fixed target experiments at the NASA Space Radiation Laboratory (NSRL). Beam in the AGS is accelerated and extracted into RHIC, where it is used for collisions at any of its six Interaction Points (IP), primarily at the two detectors: Solenoidal Tracker At RHIC (STAR) and Pioneering High Energy Nuclear Interaction eXperiment (PHENIX). At interaction points (IPs) where collisions are not desired, the two beams are separated to avoid collisions.

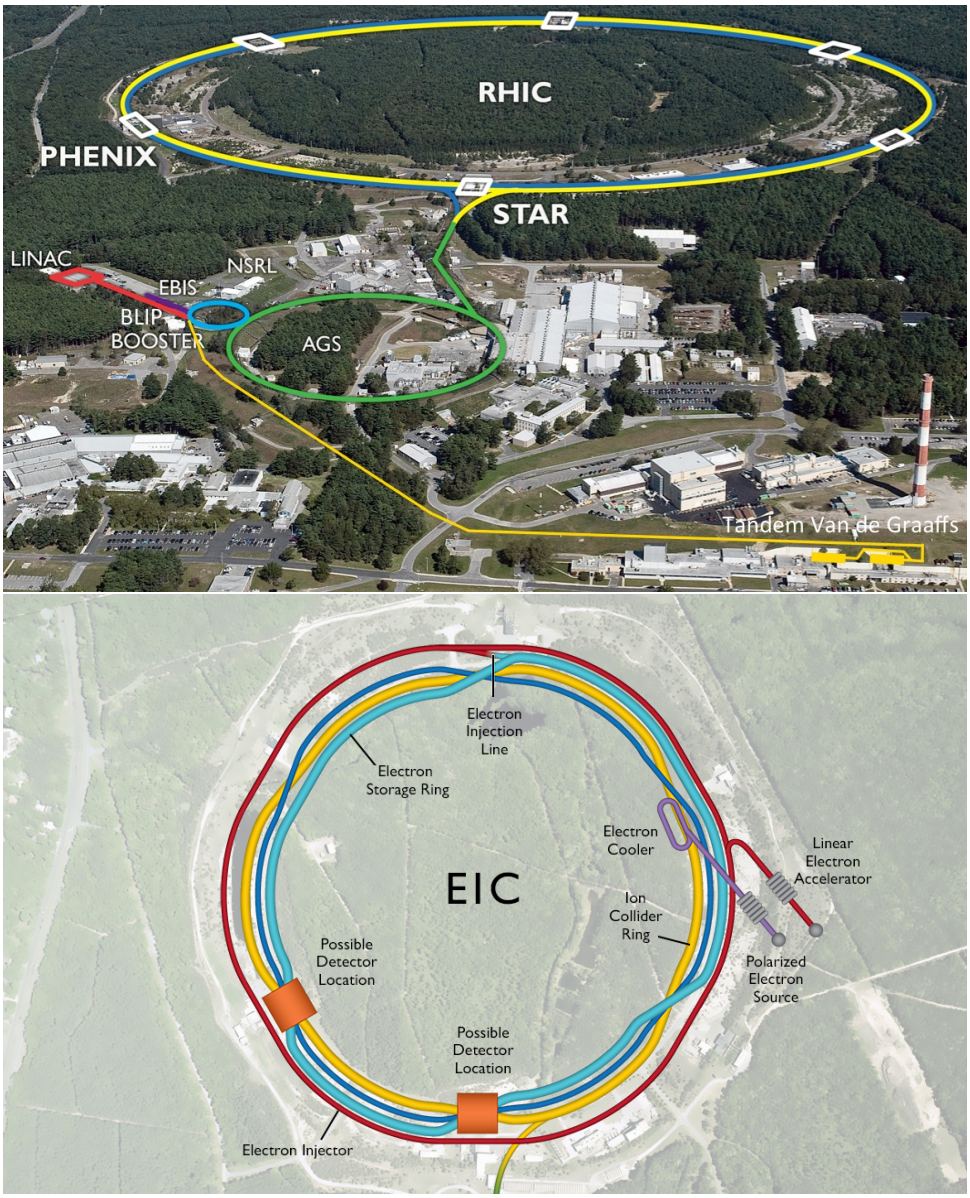

Figure 1.1: Aerial view of the RHIC accelerator complex (top) and the updated EIC complex that utilize the existing injectors (bottom).

The primary function of a particle collider is to provide particle collisions centered on a detector. The likelihood of a collision occurring is proportional to the luminosity which

is defined as

$$\mathcal{L} = \frac{N_1 N_2 f_{rev} N_b}{4\pi\sigma_x\sigma_y} \tag{1.1.1}$$

where N_1 and N_2 are the intensities of the two colliding bunches, N_b is the number of bunches, f_{rev} is the revolution frequency, and σ_x and σ_y are the transverse beam sizes. The revolution frequency is,

$$f_{rev} = v/C \tag{1.1.2}$$

where $C = 2\pi r$ is the circumference of the ring, r its average radius, and v is the particle speed. The luminosity is a key performance feature for colliders. Because of the high speed of the bunches ($\beta \sim 1$, where $\beta = v/c$ is the ratio of velocity to speed of light, c), increasing f_{rev} is impractical. N_b is primarily constrained by the harmonic of RF used in the collider, and would require installation of higher harmonic cavities to allow a higher bunch count. There are additional constraints to the number of bunches, such as the rise time of injection and abort kickers. Maximizing N_1 and N_2 for colliding bunches has its limits including: limitations on the ion sources, efficiency of the injector accelerators (which has interplay with space-charge effects), and beam-beam tune shifts for colliding bunches [9]. Increasing intensity per bunch while minimizing the transverse beam size are the parameters optimized during daily operation in order to maximize $\mathcal{L}$ (Eq. 1.1.1). The optimization of these parameters starts at the sources and continues through the whole accelerator chain.

The analyzing power of a detector for polarized collisions is proportional to the polarization squared, for transversely polarized bunched ion collisions; whereas longitudinally polarized bunched polarized ions collisions follows the polarization to the fourth (Eq. 1.1.3). This is known as the figure of merit (FOM) [10],

$$FOM = P^4 \int \mathcal{L}\, dt \tag{1.1.3}$$

where P is the beam polarization, defined as the ensemble average projection of spins on the stable spin direction. The beam polarization for a S=1/2 particle is the relative number of particles in the spin-up (+1/2) state, $N_\uparrow$, compared to the spin-down (-1/2)

state, $N_{\downarrow}$, and is defined as,

$$P = \frac{N_{\uparrow} - N_{\downarrow}}{N_{\uparrow} + N_{\downarrow}}. \tag{1.1.4}$$

Because of Eq. 1.1.3, maximizing the polarization transmission through the acceleration chain is paramount. The required per bunch intensity and polarization of helion for EIC is 1×10^{11} ions and 70% polarization, respectively. Unpolarized helions from EBIS were used in RHIC during Run14 with an intensity of 0.38×10^{11}.

1.1.1 Polarized proton and helion sources

The production of polarized protons by the OPPIS begins with hydrogen that are stripped of their electrons using electron cyclotron resonance (ECR) to generate the proton plasma [8]. The protons then enter a vapor of polarized electrons where the electrons are captured, forming hydrogen. The electrons in the vapor are polarized by optically pumping Rb using a 795 nm laser in a strong magnetic field, to excite transitions between energy levels and corresponding spin states. Transitioning an electron between two energies separated by ΔE requires laser light that satisfies

$$\Delta E = \frac{hc}{\lambda} \tag{1.1.5}$$

where h is the Planck constant and λ is the wavelength of the laser light. The protons bound with the polarized electrons pass through a field reversal region which, via hyperfine interaction, transfers the spin from the electron to the proton which is known as the Sona transition [11]. The proton spin polarized hydrogen pass through a sodium cell that binds an additional electron to the proton, forming H-. This extra electron provides the necessary charge to be accelerated in the 200 MeV LINAC and into the Booster. Upon entering the Booster, the two electrons are removed by a stripping foil, producing polarized protons. The injection of protons takes 200-300 μs, with a revolution period of

$$T_{rev} = \frac{1}{f_{rev}} \tag{1.1.6}$$

T_{rev}=1.2 μs resulting in each proton passing through the stripping foil on many turns. As measured by the polarimeter in the High Energy Beam Transport line, the source delivers P=80% during typical conditions.

Polarized helions will be produced by an upgrade of the EBIS [12]. EBIS is presently capable of providing an array of different ions for injection into the Booster, ranging from helium to Uranium. This upgrade will extend the length of the electron trap, producing approximately 50% more beam and have a dedicated section for the production of polarized helions. The helions are polarized using a technique known as metastability exchange optical pumping (MEOP) [13]. The atom is excited out of its ground state via RF excitation and optically pumped with a 1083 nm laser to the desired 2P state, which simultaneously polarizes ground-state atoms via hyperfine coupling. This technique produces polarized helion beams up to 90%. After polarization, EBIS strips electrons off through electron-electron collisions [14]. The produced ions are accelerated, primarily by a fixed frequency LINAC at 2 MeV/u, where u is the nucleon count, and transported to the Booster via the EBIS to Booster (EtB) transport line. Polarized helions will leave the EBIS fully stripped of their electrons.

Table 1.1: Table of parameters for protons and helions.

	protons	helions
m_o [MeV]	938.272088	2808.391607
u	1	3
q [e]	1	2
G	1.792847351	-4.184153686

1.1.2 Booster

The Booster is the first synchrotron accelerator in the RHIC accelerator chain that receives species from the various sources, see Fig. 1.1. It was turned on in 1991 to serve as an injector for the AGS, and provide Slow Extracted Beam (SEB) to fixed target experiments. Prior to the installation of the Booster, the heaviest ion AGS could accelerate was ^{28}Si because of the AGS vacuum. After the installation of the Booster, the AGS has accelerated any ion requested by the RHIC physics program (present maximum of

^{238}U, provided by EBIS, during the RHIC run in 2012) which is due to Booster's superior vacuum (10^3 improvement over the AGS vacuum) [15]. The improved vacuum reduces the cross section of an electron being stripped off or captured by the heavy ions being accelerated.

The Booster has a circumference of 201.78 m, which is one quarter the length of the AGS (807.12m) and one nineteenth the circumference of RHIC (3833.85 m). The Booster is made up of a series of focusing and defocusing quadrupole magnets, a pair of which is a FODO cell, with the letter O predestining the space between the quadrupole pairs which is often a drift space, and is discussed in detail in Sec. 1.2. A FODO half-cell refers to an instance where the FO and DO are treated separately. The superperiodicity of the Booster is P=6, labeled A through F on Fig. 1.2. These 6 superperiods each contain 8 FODO half-cells (numbered 1 through 8), with 6 main dipoles (at the 1, 2, 4, 5, 7 and 8 locations), 4 vertical correctors (at the odd numbered locations), and 4 horizontal correctors (at the even numbered locations). The majority of the drift spaces are where the main dipole magnets are seated. Every third and sixth FODO half-cell drift section is void of main dipoles to house instrumentation packages, RF accelerating cavities, and injection and extraction kickers. The A3 and B3 straight sections house the main RF cavities, and sections A6 and B6 house the low frequency RF cavities. Each dipole is a 10 degree sector bend that is 2.42 m in magnetic length with a radius of curvature of ρ=13.866 m. The main quadrupoles have six windings, five from the main magnet power supply and one additional winding from either the horizontal or vertical tune trim supplies. In addition there are two chromaticity supplies for the ring sextupoles.

During a single AGS cycle there is always more than one fast Booster cycle. The first fast cycle is not used for beam but to get the magnets on the same hysteresis cycle. For polarized protons a single pulse is injected into the Booster where it is scraped (purposefully placed at a limiting aperture to shape the beam through beam loss) to reduce its size and then injected into AGS, as seen on the GPM (General Purpose Monitor) in Fig. 1.3.

As these polarized particles are accelerated through the chain of accelerators, up to the

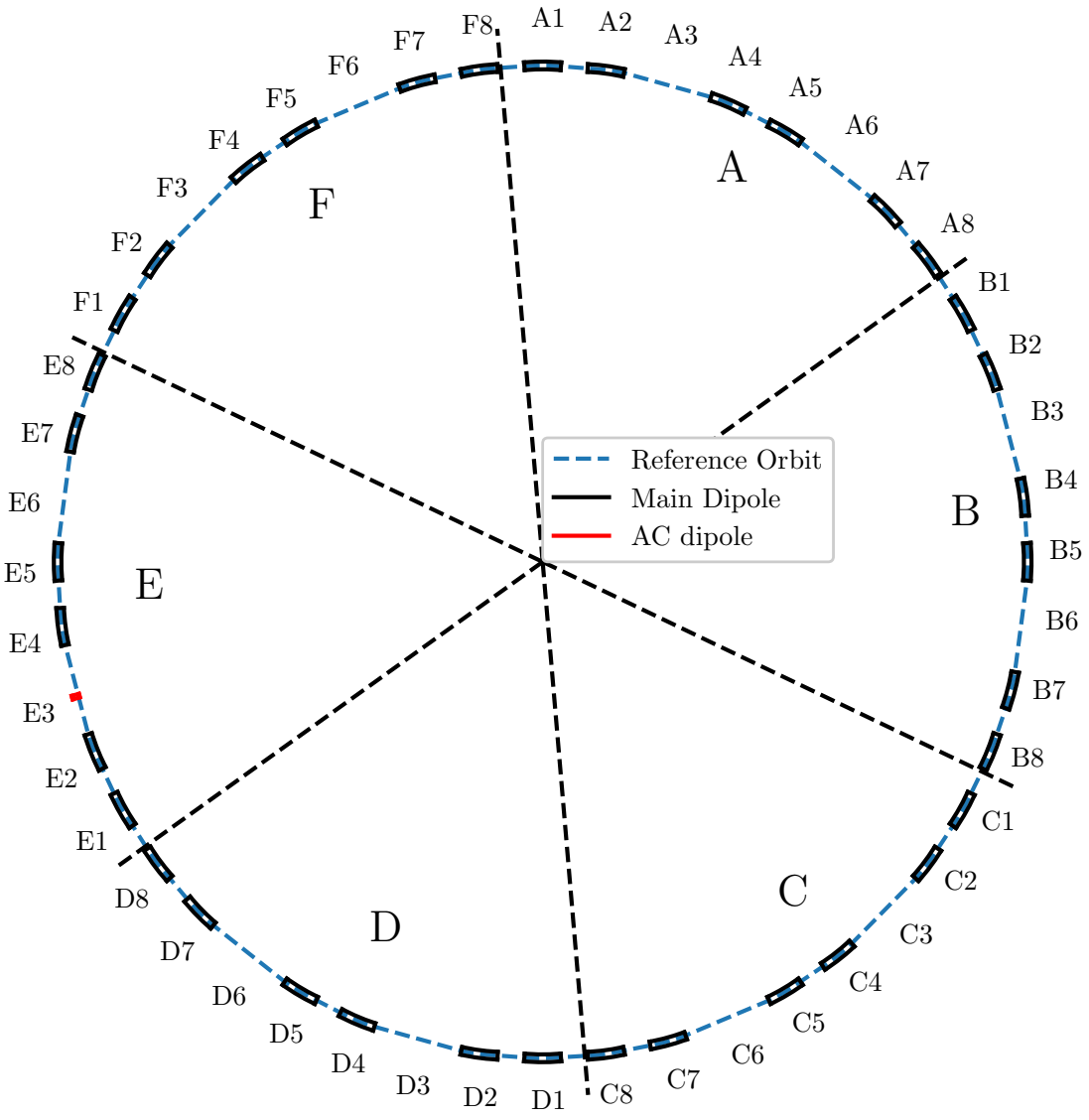

Figure 1.2: Layout of the Booster showing the six superperiods (A to F), the main dipoles, and the AC dipole.

maximum energy of RHIC and the future EIC, there are a number of spin depolarizing resonances with the possibility of significant polarization loss that must be corrected or compensated for. The need for a polarization preservation device in the Booster for helions, when one is not needed for protons, arises from the presence of intrinsic resonances in the $G\gamma$ range from injection to extraction [16–18]. The Booster AC dipole is being installed to allow 100% polarization transmission through two of these depolarizing spin resonances, discussed in Sec. 1.3.

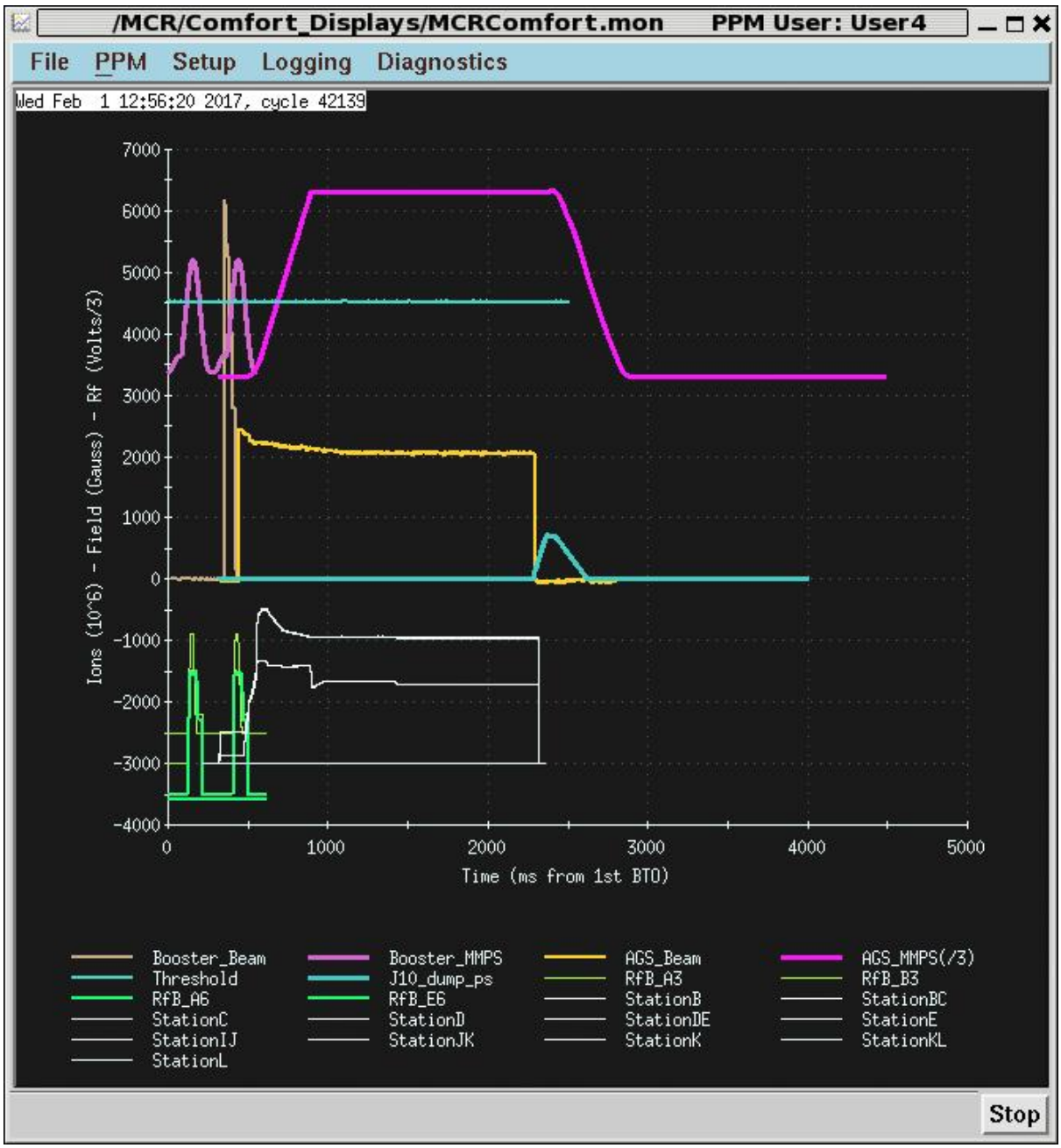

Figure 1.3: Snapshot of polarized proton SuperCycle with two fast Booster pulses followed by the AGS cycle.

1.1.3 AGS

The next injector is the AGS built in 1960 [19], which along with the Proton Synchrotron (PS) at CERN, were the first accelerator design to utilize the concept of strong focusing. The AGS achieves this with alternating dipole magnets with pole tips rolled relative to each other, as seen in Fig. 1.4. This symmetry between the pole tips provided a strong focusing gradient and provided net focusing in both transverse planes [20]. The AGS

has 240 combined function dipoles distributed equally in 12 superperiods labeled A to L. There are two tune quadrupole and two chromaticity sextupole families. At its inception, the AGS was used for fixed target experiments which led to the discovery of two new particles (the J/ψ and the muon neutrino), and charge-parity (CP) violation [21–23].

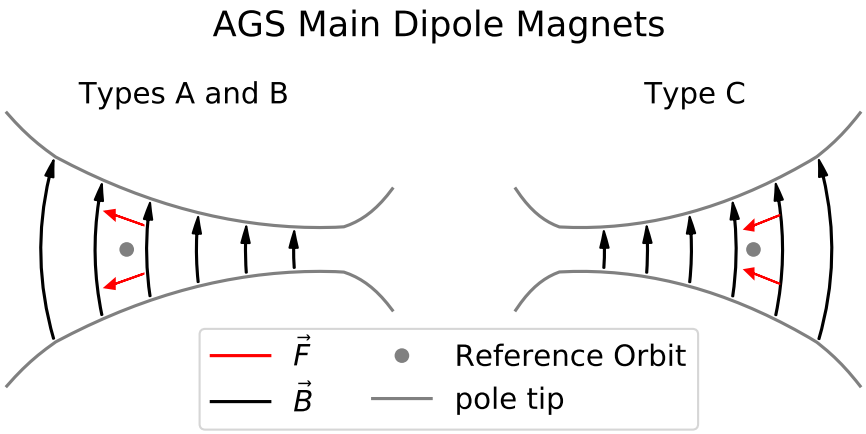

Figure 1.4: Cartoon of AGS main magnet dipole pole tips with high inhomogeneity producing high gradient fields, and reference particle coming out of the page.

After the successful acceleration of polarized protons to 12 GeV, with P=69% and 4.3×10^{10} protons, at the Zero Gradient Synchrotron (ZGS) at Argonne National Laboratory in 1973, efforts were made to accelerate polarized protons at AGS through the 1980s [24, 25]. Initial efforts used harmonic correctors to correct the 40 imperfection resonances (Sec. 1.3.1) and the fast tune jump method to overcome the intrinsic resonances (Sec. 1.3.4.1) and achieved P=40% [26, 27]. The AGS now uses two partial helical dipoles to overcome both vertical imperfection resonances and vertical intrinsic resonances and a slow tune jump to overcome horizontal imperfection resonances. This will be discussed in Section 1.3.4 [28, 29].

1.1.4 Polarimetry

Polarimeters are used to measure the polarization of ion species throughout the complex. There is one at the end of the LINAC for measuring polarization of beams that will be injected into the Booster, one in the AGS, and five in RHIC. The Booster lacks a polarimeter, so all polarized studies involving the Booster rely on measurements taken in

the AGS at injection. The AGS polarimeter, along with four of the five in RHIC, measure the asymmetry that arises from elastic scattering of polarized protons off carbons in the Coulomb Nuclear Interference (CNI) region [30]. The polarimeter has a thin carbon target that sweeps through the beam. The asymmetry of the ejected carbons are detected with silicon strip detectors. The analyzing power is determined by [31, 32],

$$A_N = \frac{1}{P}\frac{\sqrt{N_L^{\uparrow}N_R^{\downarrow}} - \sqrt{N_L^{\downarrow}N_R^{\uparrow}}}{\sqrt{N_L^{\uparrow}N_R^{\downarrow}} + \sqrt{N_L^{\downarrow}N_R^{\uparrow}}} \tag{1.1.7}$$

where $\mathrm{N_L^{\uparrow}}$ is the number of events where the proton is ejected to the left Si detector and the carbon is ejected to the right, with polarization $\uparrow$, and $\mathrm{N_R^{\downarrow}}$ is the number of events where the proton is ejected to the right Si detector and the carbon is ejected to the left, with polarization $\downarrow$.

1.2 Accelerator Physics

This section deals with the part of accelerator physics which is relevant to this thesis. The force on a particle in an accelerator that induces its motion is the Lorentz force which, is defined as [33]

$$\frac{d\vec{p}}{dt} = q(\vec{E} + \vec{v} \times \vec{B}), \tag{1.2.1}$$

where $\vec{p} = \gamma m\vec{v}$ is the momentum, γ is the Lorentz factor, $\vec{v} = d\vec{r}/dt$ is the velocity, q is the charge of the particle that is moving in electric field $\vec{E}$ and magnetic field $\vec{B}$. Magnetic fields are used to steer particles onto the desired path, where electric fields are primarily used to add energy to the particles.

The Frénet-Serret coordinate system, Fig. 1.5, is commonly used to parameterize the motion of particles and follows a reference orbit that is centered through magnets. It consists of three axes with the origin on the reference orbit: the longitudinal axis, $\vec{s}$; the binormal component which is the vertical axis, $\vec{y}$, and the normal component which is the horizontal axis, $\vec{x}$. The magnetic field can be expanded into the Frénet-Serret

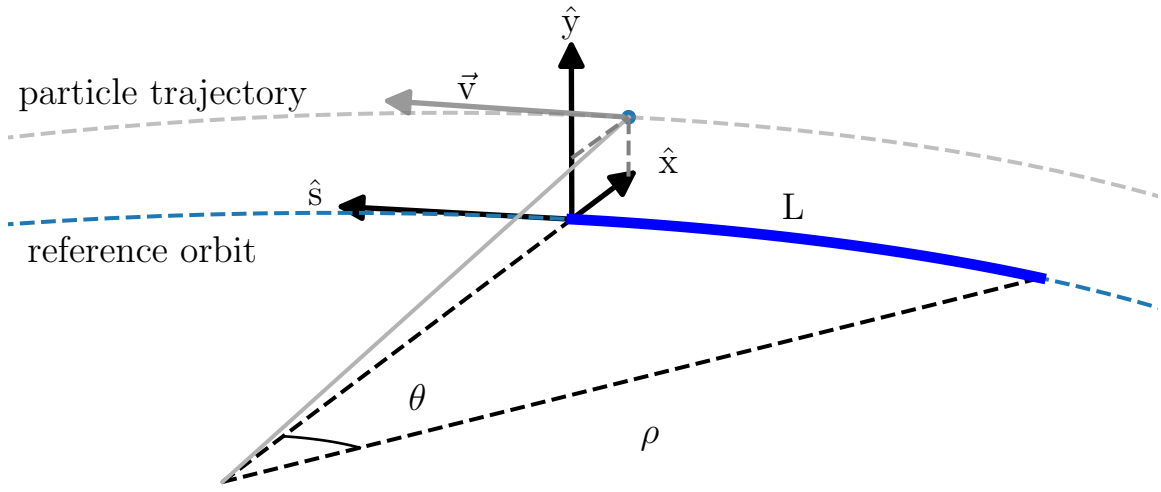

Figure 1.5: Frénet-Serret coordinate system from the reference trajectory. The curved path of distance L has a radius of curvature ρ and a change in angle θ. The Frénet-Serret coordinates are shown from the reference orbit, x, y, s and a displaced particle with velocity $\vec{v}$.

coordinates,

$$\vec{B} = B_x\hat{x} + B_y\hat{y} + B_s\hat{s} \tag{1.2.2}$$

where B_x, B_y and B_s are the horizontal, vertical and longitudinal field components, and $\hat{x}$, $\hat{y}$, and $\hat{s}$ are the unit vectors for the horizontal, vertical, and longitudinal axes. Each of these components can be Taylor expanded, for example B_y is

$$B_y = B_0 + B_1 x + B_2 x^2 + ... \tag{1.2.3}$$

where B_0 is the dipole field, B_1 is the quadrupole field gradient, and B_2 is the sextupole field. The electric field is

$$\vec{E} = E_x\hat{x} + E_y\hat{y} + E_s\hat{s} \tag{1.2.4}$$

and similarly E_x, E_y, and E_s are the horizontal, vertical and longitudinal field components which can also be expanded as in Eq. 1.2.3.

The rigidity of the beam is the relation between the magnetic field of a guiding magnet, B, and the resulting radius of curvature, ρ, for a reference particle with a given momentum, p_o. It is defined as,

$$B\rho = \frac{p_o}{q}. \tag{1.2.5}$$

Particles in a bunch may have a displacement from the reference orbit, transverse and longitudinal. Due to these displacements, they undergo oscillations around the reference orbit. The transverse dynamics, longitudinal dynamics, and spin dynamics in a synchrotron pertinent to the RHIC injector complex will be reviewed.

1.2.1 Transverse Dynamics

The series of periodic magnetic elements that are strung together to form the accelerator is known as the lattice. The horizontal and vertical equations of motion in the Frénet-Serret coordinate system are given by Hill's equation [34]

$$\frac{d^2x}{ds^2} + K_x(s)x = 0, \ \frac{d^2y}{ds^2} + K_y(s)y = 0 \tag{1.2.6}$$

where $K_x(s)$ is the horizontal field index at location s which may contain many orders of field components. For a linear system

$$\mathrm{K_x(s)} = 1/\rho(\mathrm{s})^2 \mp \mathrm{K_1(s)}, \mathrm{K_y(s)} = \pm \mathrm{K_1(s)} \tag{1.2.7}$$

and

$$\mathrm{K_1(s)} = \frac{\partial \mathrm{B_y(s)}}{\partial \mathrm{x}} \frac{1}{\mathrm{B}\rho} = \frac{\mathrm{B_1}}{\mathrm{B}\rho} \tag{1.2.8}$$

is the strength of the quadrupole field. As these are given as a function of s, as a particle transits a quadrupole, $\rho(s) = 0$. The absence of $1/\rho^2$ in K_y is due to the absence of main dipoles in the vertical plane and the $\mp$ in K_x and the $\pm$ in $\mathrm{K_y}$ is because quadrupoles focus in one plane and defocus in the other, see Fig. 1.6. $\mathrm{K_1(s)}$ is also periodic in that $\mathrm{K_1(s)} = \mathrm{K_1(s + C)}$. The solution of Eq. 1.2.6, if $K_x = K_1$=constant and K_1 is focusing ($K_1 > 0$), is

$$x(s) = x_o \cos(\sqrt{K_x}s) + x'_o \frac{1}{\sqrt{K_x}} \sin(\sqrt{K_x}s) \tag{1.2.9}$$

and

$$x'(s) = -x_o \sqrt{K_x} \sin(\sqrt{K_x}s) + x'_o \cos(\sqrt{K_x}s) \tag{1.2.10}$$

where $\mathrm{x'(s)} = \mathrm{dx/ds}$. These equations can be written in matrix form,

$$\begin{bmatrix} x \\ x' \end{bmatrix} = M(s) \begin{bmatrix} x_o \\ x'_o \end{bmatrix} = \begin{bmatrix} \cos(\sqrt{K_x}s) & \frac{1}{\sqrt{K_x}} \sin(\sqrt{K_x}s) \\ -\sqrt{K_x} \sin(\sqrt{K_x}s) & \cos(\sqrt{K_x}s) \end{bmatrix} \begin{bmatrix} x_o \\ x'_o \end{bmatrix} \tag{1.2.11}$$

where M is the transport matrix from the origin to s, and can be calculated for the various magnet elements based off the magnets' field composition. Here x_o and $\mathrm{x'_o}$ are the values of x and x′ at the origin. The x in Eq. 1.2.9, 1.2.10 and 1.2.11 are interchangeable with y with accounting for sign changes in K_x. For a particle transiting a focusing quadrupole with length $\mathrm{L_{QF}}$ and gradient $\mathrm{K_1(s)}$ the matrix has the form

$$M_{QF} = \begin{bmatrix} \cos(\sqrt{K_x}s) & \frac{1}{\sqrt{K_x}} \sin(\sqrt{K_x}s) \\ -\sqrt{K_x} \sin(\sqrt{K_x}s) & \cos(\sqrt{K_x}s) \end{bmatrix}$$

$$= \begin{bmatrix} \cos(\sqrt{K_1}L_{QF}) & \frac{1}{\sqrt{K_1}}\sin(\sqrt{K_1}L_{QF}) \\ -\sqrt{K_1}\sin(\sqrt{K_1}L_{QF}) & \cos(\sqrt{K_1}L_{QF}) \end{bmatrix} \quad (1.2.12)$$

The focal length, f, of a horizontally focusing quadrupole, QF, with gradient $K_x(s) = K_1(s)$ and length L_{QF} is,

$$f = \frac{1}{K_1 L_{QF}} \quad (1.2.13)$$

shown in Fig. 1.6.

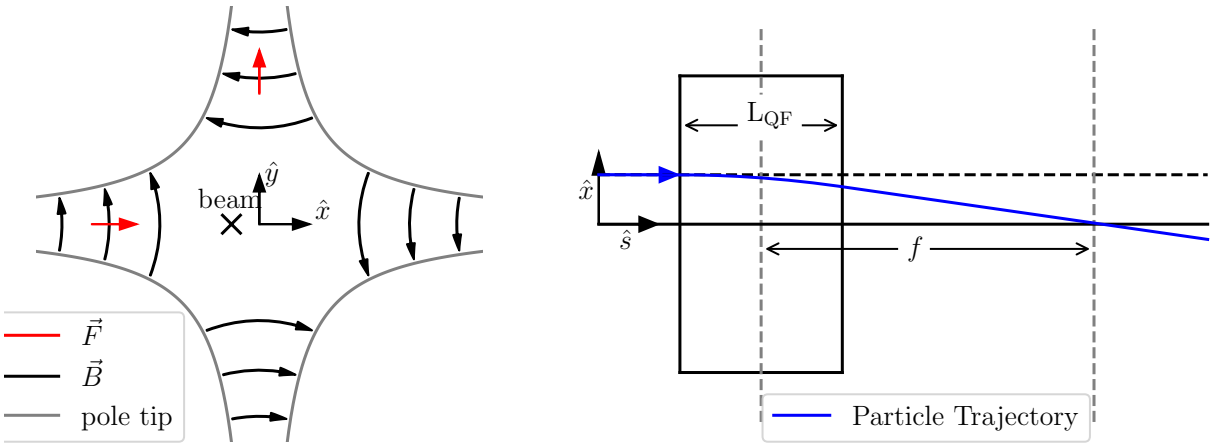

Figure 1.6: Left: Quadrupole magnetic field lines and resulting force on a positively charged particle moving into the page. Right: The horizontal bending of a single particle moving through a focusing quadrupole of L_{QF} and resulting focal length f.

This 2-dimensional transport matrix has the general form,

$$M = \begin{bmatrix} m_{11} & m_{12} \\ m_{21} & m_{22} \end{bmatrix}. \quad (1.2.14)$$

Eq. 1.2.1 is part of a larger 6x6 transport matrix that includes the vertical and longitudinal components. The updated transport matrix for a horizontally focusing quadrupole,

for example, is

$$R_{QF} = \begin{bmatrix} \cos(\sqrt{K_1}L_{QF}) & \frac{\sin(\sqrt{K_1}L_{QF})}{\sqrt{K_1}} & 0 & 0 & 0 & 0 \\ -\sqrt{K_1}\sin(\sqrt{K_1}L_{QF}) & \cos(\sqrt{K_1}L_{QF}) & 0 & 0 & 0 & 0 \\ 0 & 0 & \cosh(\sqrt{K_1}L_{QF}) & \frac{\sinh(\sqrt{K_1}L_{QF})}{\sqrt{K_1}} & 0 & 0 \\ 0 & 0 & \sqrt{K_1}\sinh(\sqrt{K_1}L_{QF}) & \cosh(\sqrt{K_1}L_{QF}) & 0 & 0 \\ 0 & 0 & 0 & 0 & 1 & 0 \\ 0 & 0 & 0 & 0 & 0 & 1 \end{bmatrix} \tag{1.2.15}$$

where the hyperbolic functions for the vertical components result from the vertical defocusing. A horizontally defocusing quadrupole has the opposite sign for K_1, its 6x6 transport matrix has the hyperbolic trigonometric functions and normal trigonometric functions swapped.

This 6x6 matrix has a general form of

$$M = \begin{bmatrix} m_{11} & m_{12} & \dots & m_{16} \\ m_{21} & m_{22} & & m_{26} \\ \vdots & & \ddots & \vdots \\ m_{61} & m_{62} & \dots & m_{66} \end{bmatrix} \tag{1.2.16}$$

The m_{11} to m_{22} 2x2 matrix represents the horizontal motion, the m_{33} to m_{44} 2x2 matrix represents the vertical motion, and the m_{55} to m_{66} represents the longitudinal transport components. Off diagonal elements represent coupling between planes. For example the m_{16} is the dispersion which is defined as a broadening in the horizontal plane after going through a horizontal bending dipole. The broadening is the result of momentum spread which results in particles being bent at different radii of curvature through the dipole and is addressed later in this section. There is also vertical dispersion from vertical dipoles but is much smaller than that from the main dipoles of an accelerator.

Considering again the 2x2 matrix from Eq. 1.2.14, these matrices can be multiplied together to get the evolution of coordinates through the accelerator such as transporting

initial coordinates through two elements, M_1 and M_2,

$$\begin{bmatrix} x_2 \\ x_2' \end{bmatrix} = M_2 M_1 \begin{bmatrix} x_0 \\ x_0' \end{bmatrix}. \tag{1.2.17}$$

and multiplying the matrices of all the elements in one turn of the ring yields the one turn matrix, M_T, defined as

$$M_T = \prod_{k=N}^{1} M_k \tag{1.2.18}$$

Considering only one plane that has a periodic structure in s, the Courant-Snyder parameterization can be applied to the transfer matrix which is given by [19]

$$M(s) = \begin{bmatrix} \cos(\phi(s)) + \alpha(s)\sin(\phi(s)) & \beta(s)\sin(\phi(s)) \\ -\gamma(s)\sin(\phi(s)) & \cos(\phi(s)) - \alpha(s)\sin(\phi(s)) \end{bmatrix} \tag{1.2.19}$$

where β(s) is the beta function, $\alpha(\mathrm{s}) = -\frac{1}{2}\mathrm{d}\beta(\mathrm{s})/\mathrm{ds}$, and ϕ(s) is the phase advance. These parameters are also known as Twiss parameters. Turn-by-turn a particle evolves on an ellipse shown in Fig. 1.7.

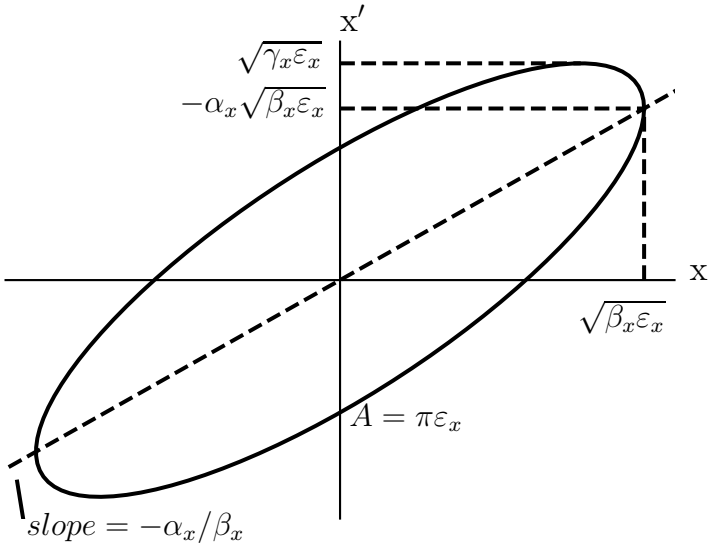

Figure 1.7: Plot showing the Courant-Snyder invariant and its geometric maxima in x and x′.

As a particle evolves from element 0 to element 1, the Twiss functions evolve with

the components of the 2x2 transport matrix between the two elements as

$$\begin{bmatrix} \beta_1 \\ \alpha_1 \\ \gamma_1 \end{bmatrix} = \begin{bmatrix} m_{11}^2 & -2m_{11}m_{12} & m_{12}^2 \\ -m_{21}m_{11} & 1+2m_{12}m_{21} & -m_{12}m_{22} \\ m_{22}^2 & -2m_{22}m_{21} & m_{22}^2 \end{bmatrix} \begin{bmatrix} \beta_0 \\ \alpha_0 \\ \gamma_0 \end{bmatrix} \tag{1.2.20}$$

and the phase advance between elements 0 and 1 is

$$\tan(\phi_1 - \phi_0) = \frac{m_{11}}{m_{11}\beta_0 - m_{21}\alpha_0}. \tag{1.2.21}$$

Given Eq. 1.2.22 and confirmed by Eq. 1.2.26, ε_{x} is the emittance of a single particle

$$\gamma x^2 + 2\alpha x x' + \beta x'^2 = \varepsilon_x. \tag{1.2.22}$$

The betatron tune, ν_x and ν_y, is the total number of oscillations a particle undergoes in one turn, defined as

$$\nu_x = \frac{1}{2\pi} \oint \frac{1}{\beta_x} ds. \tag{1.2.23}$$

The fractional component of the tunes is Q_x and Q_y. The solution for Eq. 1.2.6 is

$$x_\beta(s) = a\sqrt{\beta_x(s)}\cos(\nu_x \phi(s) + b) \tag{1.2.24}$$

where a and b are initial conditions derived from the initial coordinates, $\mathrm{x_o}$ and $\mathrm{x'_o}$. As particles are accelerated, the non-normalized emittance is damped. The normalized emittance, ε_{N}, is defined as

$$\varepsilon_N = \beta_1\gamma_1\varepsilon_1 = \beta_2\gamma_2\varepsilon_2 \tag{1.2.25}$$

where $\beta_1\gamma_1$ and $\beta_2\gamma_2$ are the Lorentz boost factors at times 1 and 2.

Considering a zero centered Gaussian beam distribution with RMS width σ_{x},

$$\sigma_x = x_{RMS} = (\sqrt{\beta_x \varepsilon})_{RMS}. \tag{1.2.26}$$

with ε_{RMS} being the RMS emittance of the bunched beam. These particle coordinates can be represented in a conjugate phase-space, where particle trajectories trace out a circle and not an ellipse. For this, new conjugate coordinates are defined by

$$X = x/\sqrt{\beta} \tag{1.2.27}$$

and

$$X' = \frac{\alpha x + \beta x'}{\sqrt{\beta_x}} \tag{1.2.28}$$

The normalized Gaussian beam distribution in this phase space is given by

$$g(X, X') = \frac{1}{2\pi\sigma_x^2} e^{-\frac{X^2+X'^2}{2\sigma_x^2}}. \tag{1.2.29}$$

Discussed in detail in Sec. 1.2.2, particles in a bunch exist in a stable range of momentum spread from $\mathrm{p_o}$. From Eq. 1.2.5, particles with momentum $\mathrm{p} = \mathrm{p_o} \pm \delta\mathrm{p}$ will have a different radius of curvature from the main dipoles resulting in a different orbit throughout the ring. The equation of motion in the horizontal plane is [35]

$$\frac{d^2x}{ds^2} + \frac{\rho + x}{\rho^2} = \frac{B_y}{B\rho}\left(1 + \frac{x}{\rho}\right)^2 \frac{p_o}{p} \tag{1.2.30}$$

where the radius of curvature for the off-momentum particle is $\rho + \mathrm{x}$. Expanding $\mathrm{B_y}$, as in Eq. 1.2.3, to first order yields

$$\frac{d^2x}{ds^2} + \left(\frac{1}{\rho^2} + \frac{B_1}{B\rho}\frac{p_o}{p}\right) = \frac{1}{\rho}\frac{\delta p}{p}. \tag{1.2.31}$$

Defining dispersion as

$$D(s) = \frac{\delta x}{\delta p/p} \tag{1.2.32}$$

and plugging into Eq. 1.2.31 yields

$$\frac{d^2D(s)}{ds^2} + K_x(s)D(s) = \frac{1}{\rho}\frac{\delta p}{p} \tag{1.2.33}$$

where D(s)δp/p is the chromatic closed orbit (CCO) for an off momentum particle.

Similarly, particles with $\delta \mathrm{p} \neq 0$ experience different focusing from quadrupoles. This change in focusing, ignoring higher order terms, is

$$\Delta K_x \approx -K_x \frac{\delta p}{p} \tag{1.2.34}$$

. The chromaticity, ξ_{x}, is written as

$$\xi_x = \frac{\delta \nu_x}{\delta p / p} \tag{1.2.35}$$

where $\delta \nu_{\mathrm{x}}$ is the change in tune for a given change in momentum error defined as,

$$\delta \nu_x \approx \left(\frac{1}{4\pi} \oint \beta_x K_x ds \right) \frac{\delta p}{p}. \tag{1.2.36}$$

The term

$$\frac{1}{4\pi} \oint \beta_x K_x ds = \xi_{x,nat} \tag{1.2.37}$$

is the natural chromaticity. The natural chromaticity is the chromaticity value from the presence of solely quadrupoles and no higher order magnets. The chromaticity can be corrected, or controlled, using sextupole magnets with strength

$$S(s) = -\frac{1}{B\rho} \frac{\partial^2 B_y}{\partial x^2}. \tag{1.2.38}$$

The corrected chromaticity is

$$\xi_x = -\frac{1}{4\pi} \oint \beta_x [\Delta K_x(s) - S(s) D(s)] ds. \tag{1.2.39}$$

The horizontal normalized chromaticity is defined as,

$$C_x = \frac{\xi_x}{\nu_x}. \tag{1.2.40}$$

1.2.1.1 Closed Orbit Bump

A closed orbit bump is a local change in orbit to achieve a certain position and/or angle at a desired location. Outside of the local bump region the orbit is zero, and is referred to as closed. The angular deflection or kick, θ_k, from a dipole of strength B_k and length L_c is

$$\theta_k = \frac{B_k L_c}{B\rho}. \tag{1.2.41}$$

In the Booster, orbit bumps using three dipole correctors (three-bump) are common. The correctors 1, 2, and 3 provide an angle kick of θ_1, θ_2, and θ_3. For the bump to be closed, the following conditions must be met [9]:

$$\frac{\theta_2}{\theta_1} = -\sqrt{\frac{\beta_1}{\beta_2}}\frac{\sin(\phi_3 - \phi_1)}{\sin(\phi_3 - \phi_2)}, \text{ and } \frac{\theta_3}{\theta_1} = -\sqrt{\frac{\beta_1}{\beta_3}}\frac{\sin(\phi_2 - \phi_1)}{\sin(\phi_2 - \phi_3)} \tag{1.2.42}$$

where $\beta_{1,2,3}$ are the beta functions and $\phi_{1,2,3}$ are the betatron phase advances at the location of the three correctors. Considering a vertical bump, $\theta_{1,2,3}$ are vertical kicks and $\beta_{1,2,3}$ are the vertical beta functions. For a vertical bump, y(s) and y$'$(s) between correctors 1 and 2 are:

$$y(s) = \theta_1\sqrt{\beta_1\beta(s)}\sin(\phi(s) - \phi_1) \tag{1.2.43}$$

and

$$y'(s) = \theta_1\sqrt{\frac{\beta_1}{\beta(s)}}[\cos(\phi(s) - \phi_1) - \alpha(s)\sin(\phi(s) - \phi_1))]; \tag{1.2.44}$$

and between correctors 2 and 3,

$$y(s) = \theta_3\sqrt{\beta_3\beta(s)}\sin(\phi_3 - \phi(s)) \tag{1.2.45}$$

and

$$y'(s) = -\theta_3\sqrt{\frac{\beta_3}{\beta(s)}}[\cos(\phi_3 - \phi(s)) + \alpha(s)\sin(\phi_3 - \phi(s))]. \tag{1.2.46}$$

1.2.1.2 Dipole Field Errors

Unlike the closed orbit bump where dipole kicks were implemented in a way to control the position at a specific location, closed orbit errors result from random dipole errors. Neither the alignment of magnets through the ring nor the uniformity of the field in a magnet are perfect. Because of feed-down, where a higher order multipole magnet can produce fields of lower order when a particle's trajectory is not centered in the magnetic element, the most common field error are dipole field errors since it can be produced by all higher order magnets. To this point, only betatron amplitudes have been considered, x_β, and if a small displacement error at a quadrupole is considered, δx, a dipole field is sampled at $\Delta B_x = B_1 \delta x$. The vertical closed orbit, y_{co}, resulting from a single dipole error with integrated field ΔBdl at location s_o is

$$y_{co}(s) = G(s, s_o)\frac{\Delta B(s_o)dl}{B\rho} \tag{1.2.47}$$

with G(s,s_o) is the Green function of Hill's equation defined as,

$$G(s, s_o) = \frac{\sqrt{\beta_y(s)\beta_y(s_o)}}{2\sin(\pi\nu_y)}\cos(\pi\nu_y - |\psi(s) - \psi(s_o)|) \tag{1.2.48}$$

which yields,

$$y_{co}(s) = \frac{\sqrt{\beta_y(s)\beta_y(s_o)}}{2\sin(\pi\nu_y)}\cos(\pi\nu_y - |\psi(s) - \psi(s_o)|)\theta(s_o) \tag{1.2.49}$$

where s_o is the location of the error, s is the location around the ring, $\theta(s_o)$ is the kick angle, and

$$\psi_s = \int_{s_o}^{s} \frac{1}{\beta_y(s)} ds. \tag{1.2.50}$$

If two dipole errors are considered, an interference modification to Eq. 1.2.49 is used of the form,

$$y_{co}(s) = \frac{\sqrt{\beta_y(s)\beta_y(s_o)}}{2\sin(\pi\nu_y)}\cos(\pi\nu_y - |\psi(s) - \psi(s_o)| + \phi)\theta(s_o) \tag{1.2.51}$$

that introduces a phase offset, ϕ, for the closed orbit.

In reality these errors are distributed throughout the ring. Distributed dipole field errors of ΔB(s$'$) result in a closed orbit error of [34]

$$y_{co}(s) = \int_{s}^{s+C} G(s,t)\frac{\Delta B(s')}{B\rho}ds' \tag{1.2.52}$$

where s' is the s coordinate of the field errors. Eq. 1.2.48 has the solution

$$y_{co}(s) = \sqrt{\beta_y(s)}\sum_{k=-\infty}^{\infty}\frac{\nu_y^2 f_k}{\nu_y^2 - k^2}e^{ik\phi} \tag{1.2.53}$$

where k is an integer orbit harmonic and f_k is known as the integer stopband integral defined as

$$f_k = \frac{1}{2\pi\nu_y}\oint\sqrt{\beta_y(s)}\frac{\Delta B(s)}{B\rho}e^{-ik\phi}ds \tag{1.2.54}$$

From Eq. 1.2.53 it is clear the strongest harmonic excited is that nearest ν_y.

To correct these excited orbit harmonics, a correction scheme is implemented using dipole correctors distributed throughout the ring. The kick required at dipole i to correct harmonic k is,

$$\theta_i = \frac{1}{\sqrt{\beta_i}}(a_k\sin(k\phi_{ik}) + b_k\cos(k\phi_{ik})) \tag{1.2.55}$$

where a_k and b_k are the strengths of the sine and cosine corrections, and ϕ_{ik} is the harmonic phase of corrector i with harmonic k. The excitation of the Booster corrector dipoles is 0.975 G $\cdot$ m/A and the harmonic correction scheme is implemented as such

$$I_i = \sum_{k=1}^{\infty} I(a_k)\sin(k\phi_i) + I(b_k)\cos(k\phi_i) \tag{1.2.56}$$

where the current of corrector i depends on the current of the sine and cosine corrector families and its harmonic phase.

Feed-down from having a non-zero closed orbit in sextupoles causes the particles to sample a quadrupole field and will thus cause a change in tune.

1.2.1.3 Dynamic Aperture

The dynamic aperture (DA) is the area defined by the maximum amplitude at which a particle will not be lost from single particle dynamics. This differs from the admittance, which concerns the physical aperture of the machine. The DA is determined numerically at a given optics configuration ($\nu_{\mathrm{x}},\ \nu_{\mathrm{y}}$ location) through particle tracking for many turns to determine if the particle is lost. Fig. 1.8 shows the stable range of x and y coordinates for $\nu_{\mathrm{x}} = 8.77$ and $\nu_{\mathrm{y}} = 8.88$. The stable area is used to determine the DA and is discussed further in Sec. 2.5.

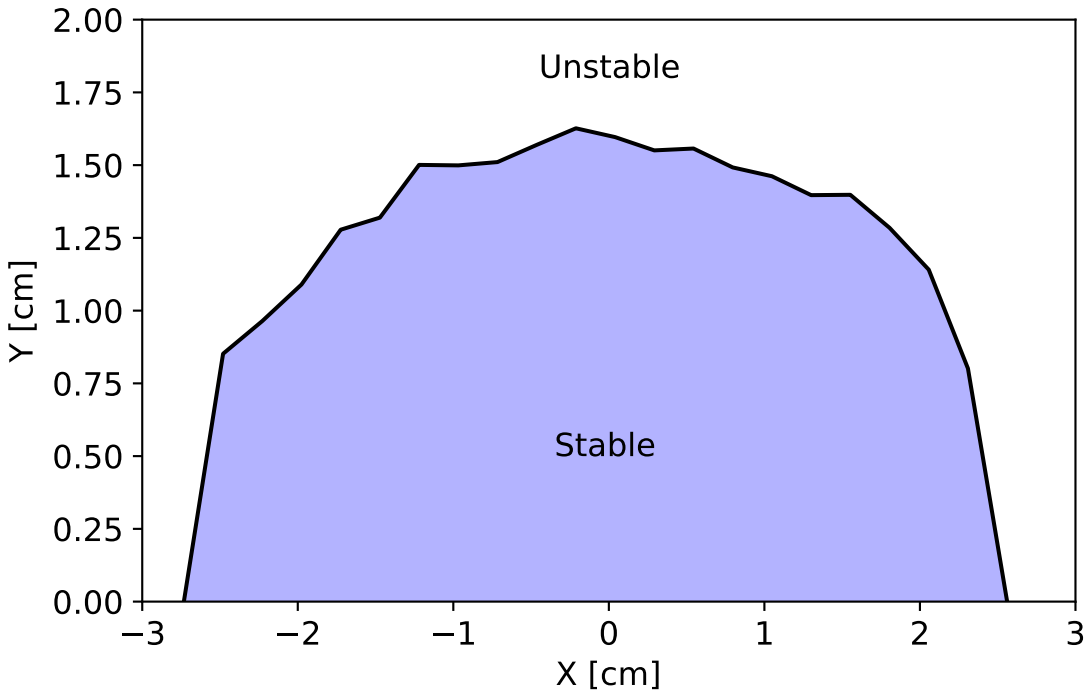

Figure 1.8: Example dynamic aperture in the AGS with $\nu_x = 8.77$ and $\nu_y = 8.88$.

1.2.1.4 Beam Dynamics with an AC dipole

An AC dipole with horizontal field $\mathrm{B_m}$ modulates vertical oscillations of the particles with tune,

$$\nu_m = \frac{f_m}{f_{rev}} \tag{1.2.57}$$

where f_m is the AC dipole frequency. An AC dipole is part of an LC circuit where L is the inductance of the magnet, and C is the capacitance added to the circuit to reach the

desired modulation frequency. That is,

$$f_m = \frac{1}{2\pi\sqrt{LC}} \tag{1.2.58}$$

. The separation between ν_{y} and ν_{m} is known as the resonance proximity parameter, δ_m, defined as

$$\delta_m = \nu_y - (\nu_m + n) \tag{1.2.59}$$

where n is an integer. The vertical betatron motion with the angular deflection from the AC dipole is Eq. 1.2.60 [36]

$$\frac{d^2y}{ds^2} + K_y(s)y = -\frac{B_m \cos(\nu_m\theta)}{B\rho} \tag{1.2.60}$$

where $\mathrm{B_m}$ is the maximum field produced by the AC dipole and θ is the azimuthal angle around the ring. This drives coherent betatron oscillations with amplitude

$$Y_{coh} = \frac{B_m L}{4\pi B\rho\delta_m}\beta_y \tag{1.2.61}$$

An AC dipole that is an iron core window frame magnet with a single winding of copper has a magnetic excitation of

$$B_m = \mu_o \frac{I_m}{g} \tag{1.2.62}$$

where I_m is the current through the copper windings, μ_o is the permeability of free space, g is the gap and B_m is the resulting field.

The AC dipole pulse goes from zero to its maximum setpoint over a number of turns $\mathrm{N_{up}}$, remains at its maximum amplitude for a duration sufficient to achieve a full spin-flip, $\mathrm{N_{flat}}$, and then is ramped back down to zero over $\mathrm{N_{down}}$ turns.

1.2.2 Longitudinal Dynamics

To accelerate particles, radio frequency (RF) cavities are used that produce a longitudinal electric field. The longitudinal electric field is a sine wave with a wavelength being a sub-harmonic of the accelerators' circumference. A particle that circulates around the ring and arrives at the cavity with the same phase of the RF wave is synchronous. This synchronous particle has phase ϕ_{s} (synchronous phase) and momentum $\mathrm{p_o}$. A particle that is traveling on the closed orbit, which arrives before or after the synchronous particle (either due to longitudinal offset or momentum deviation), will have a different phase and will receive a different longitudinal kick from the electric field. The kicks received by the non-synchronous particles will cause them to oscillate around a fixed point in a motion known as synchrotron oscillations. The number of turns it takes for a particle to complete an oscillation is the synchrotron period, $\mathrm{T_s}$, and the synchrotron tune being $\mathrm{Q_s} = \mathrm{T_{rev}}/\mathrm{T_s}$ where $T_{rev} = 1/f_{rev}$ is the revolution period.

The change in energy per turn for a typical RF system is given by,

$$\Delta E = qV_{RF}(\sin(\phi) - \sin(\phi_s)) \tag{1.2.63}$$

where V_{RF} is the peak RF cavity voltage, ϕ_{s} is the synchronous phase, and ϕ is the phase of the particle. The RF frequency and the revolution frequency are related by,

$$f_{RF} = h_{RF} f_{rev} \tag{1.2.64}$$

where $\mathrm{h_{RF}}$ is the harmonic at which the RF cavity is operating, and the revolution frequency is,

$$f_{rev} = \frac{v}{C} \tag{1.2.65}$$

where v is the velocity and C is the circumference. The phase-space mapping of these oscillations between turn n and turn n+1 is defined as [35],

$$\frac{\delta p_{n+1}}{p_{n+1}} = \frac{\delta p_n}{p_n} + \frac{qV}{\beta^2 E}(\sin\phi_n - \sin\phi_s) \tag{1.2.66}$$

where $\phi_{\rm n}$ is the phase of the particle and $\delta_{\rm n}$ is δp on turn n, and the phase $\phi_{\rm n+1}$ is

$$\phi_{n+1} = \phi_n + 2\pi h_{RF}\ \frac{\delta p_{n+1}}{p_{n+1}}\ \eta(\frac{\delta p_{n+1}}{p_{n+1}}) \tag{1.2.67}$$

and $\eta(\delta {\rm p_{n+1}}/{\rm p_{n+1}})$ is known as the phase slip factor. The slip factor is defined as,

$$\eta = \frac{1}{\gamma_T^2} - \frac{1}{\gamma^2} \tag{1.2.68}$$

and $\gamma_{\rm T}$ is the transition gamma. When $\gamma < \gamma_{\rm T}$ a particle with $\delta {\rm p} > 0$ will have a higher revolution frequency. Above the transition gamma, a higher energy particle will have a lower $\rm f_{rev}$. At $\gamma = \gamma_{\rm T}$ all particles have the same revolution frequency regardless of δp. In the Booster $\gamma_T = 4.62$ and $\gamma_T = 4.69$ for protons and helions, respectively.

When there is no acceleration, $\phi_{\rm s} = 0$, which produces a phase-space map (Eq. 1.2.66 and Eq. 1.2.67) shown in Fig. 1.9 (left). Typical RF parameters for acceleration of hadrons in the Booster are $\phi_{\rm s} = \pi/6$, $\rm V_{RF} = 32$ kV, and h_{RF}=1; the resulting phase-space map is shown in Fig. 1.9 (right). Under acceleration the phase-space area is damped by a factor of $\beta_{\rm n-1}\gamma_{\rm n-1}/\beta_{\rm n}\gamma_{\rm n}$. There are four RF cavities in the Booster: two high frequency and two low frequency. These two pairs of RF cavities (high and low frequency) are frequently operated to carry out a number of longitudinal beam manipulations which include bunch merging and bunch lengthening.

With a dual harmonic RF cavity configuration, the equation of motion is given by [35]

$$\dot{\delta} = \frac{f_{rev} q V_1}{\beta^2 E}\left[\sin\phi - \sin\phi_{1s} + \frac{V_2}{V_1}\left[\sin\left(\phi_{2s} + \frac{h_2}{h_1}(\phi - \phi_{1s})\right) - \sin\phi_{2s}\right]\right] \tag{1.2.69}$$

where indices 1 and 2 refer to the first and the second cavity respectively with V being the voltage of the cavities, $\phi_{\rm s}$ are the synchronous phases, h are the RF harmonic numbers.

Bunch merging is when a large number of bunches from RF operating at a high harmonic are merged to produce fewer bunches but with higher intensity, using RF cavities at a lower harmonic. In the Booster, the frequency range of the RF cavities requires a harmonic of h=4 to capture beam from EBIS. The beam from EBIS enters Booster as a

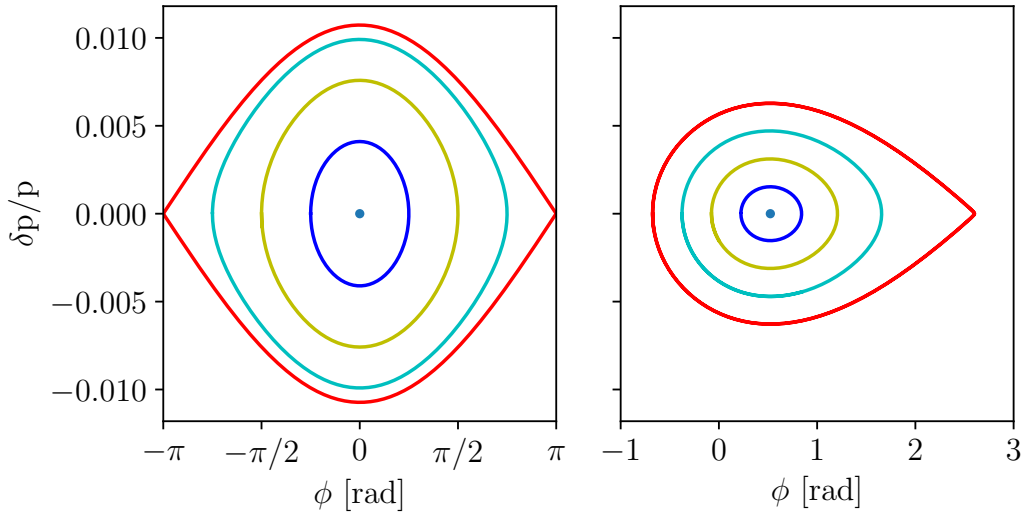

Figure 1.9: Left: Figure showing the longitudinal phase-space for $\phi_s = 0$. Right: Figure showing the longitudinal phase-space for $\phi_s = \pi/6$

continuous ribbon that fills the entire circumference of the machine. The h=4 cavities are ramped up in voltage to capture the beam into four equally spaced RF buckets. These cavities then accelerate to an energy sufficiently high for the cavities to operate at a lower harmonic. The RF voltage on the one set of cavities is adiabatically lowered as the other, at a lower harmonic, is raised. The merging is typically done from h=4 to h=2 and then from h=2 to h=1, an example "2-to-1" bunch merge is shown in Fig. 1.10.

Bunch lengthening is possible with two sets of RF cavities, at different harmonics, operating concurrently to stretch the bunch. This configuration is desired for multiple reasons: by increasing the length of the bunch in this manner, the longitudinal current distribution becomes more uniform which minimizes effects from space charge; the stable phase-space region is elongated, as seen in 1.11, which reduces the maximum momentum spread of the bunch. Values for these parameters in the Booster are: $V_1 = 32$ kV, $V_2 = 10$ kV, $h_1 = 1$, $h_2 = 2$, $\phi_{1s} = \pi/6$, $\phi_{2s} = \pi$, and for helions at E=5.24 MeV, $Q_s = 0.0057$, and $f_{rev} = 1.255$ MHz.

Fig. 1.11 shows the comparison of phase space area resulting from single and dual harmonic cavities, using the parameters described above.

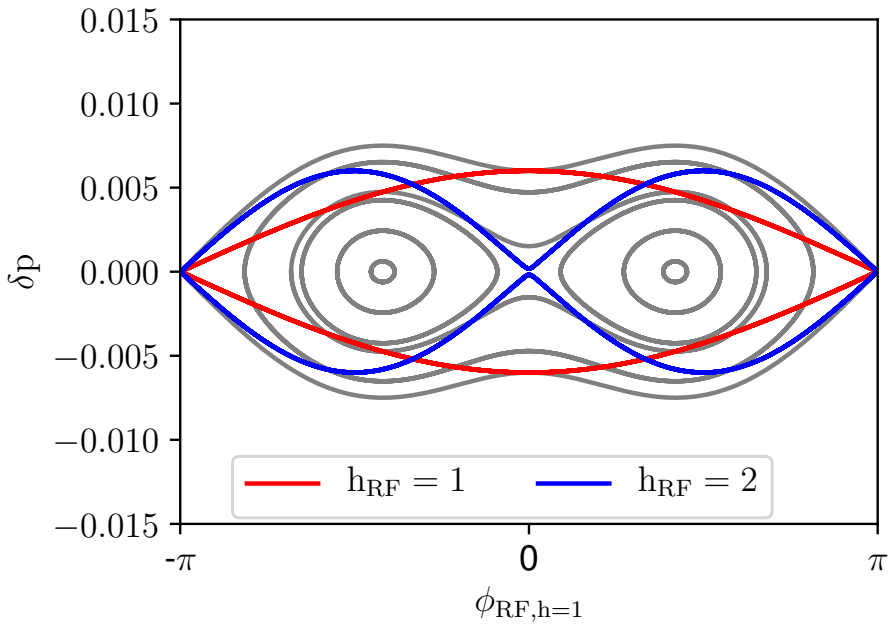

Figure 1.10: Longitudinal phase space diagram for a "2-to-1" bunch merge with RF parameters: h_1=1, V_1=10 kV, and h_2=2, $V_2 = 2V_1$. The gray lines are the resulting longitudinal phase space for different amplitudes. The red and blue lines are the stability limit for h_{RF} =1 and 2, respectively.

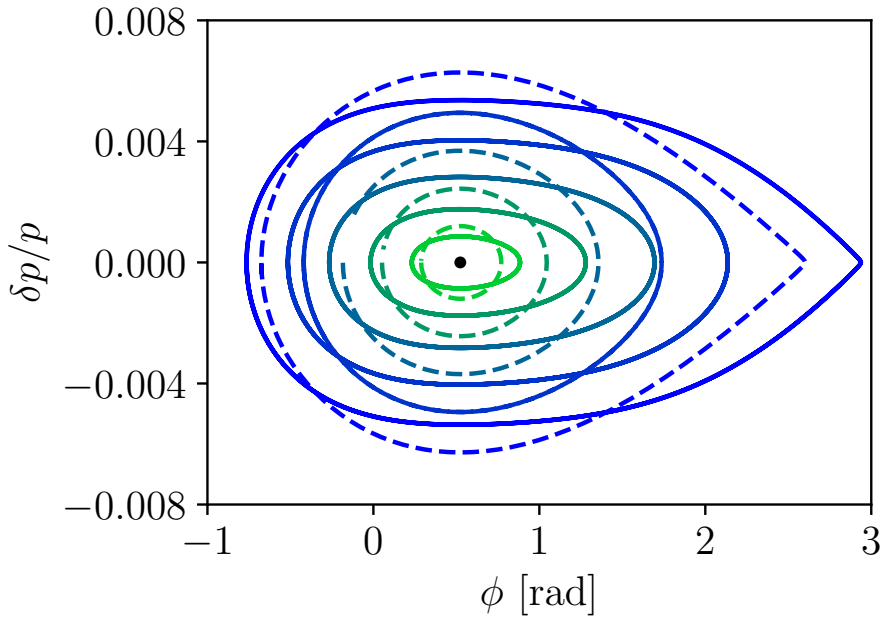

Figure 1.11: Phase-space comparison from single harmonic in dashed lines and dual harmonic, Eq. 1.2.69, in solid lines.

1.3 Spin Dynamics

This section establishes the mechanics of a particle spin motion in a synchrotron. The nuclear magnetic moment, $\vec{\mu}$, is defined as

$$\vec{\mu} = g\frac{q}{2m_o}\vec{S} \tag{1.3.1}$$

where g is the gyromagnetic ratio, m_o is the rest mass, and $\vec{S}$ is the spin vector. $\vec{S}$ is defined as

$$\vec{S} = S_1\hat{x} + S_2\hat{s} + S_3\hat{y} \tag{1.3.2}$$

with $\hat{}$ denoting unit vectors in the x, y, and s directions. The magnetic moment, $\vec{\mu}$, in its rest frame and in the presence of a magnetic field, $\vec{B}$, will experience a torque, $\vec{\Gamma}$,

$$\vec{\Gamma} = \vec{\mu} \times \vec{B} = \frac{d\vec{S}}{dt} \tag{1.3.3}$$

which causes it to precess.

The Thomas-BMT (Bargman-Michel-Telegdi) equation describes the motion of the spin vector in the lab frame when exposed to magnetic and electric fields in a synchrotron and is defined as [37, 38],

$$\frac{d\vec{S}}{dt} = \frac{q}{\gamma m_o}\vec{S} \times \left[(1+G\gamma)\vec{B_\perp} + (1+G)\vec{B_\parallel} + (G\gamma + \frac{\gamma}{\gamma+1})\frac{\vec{E}\times\vec{\beta}}{c}\right] \tag{1.3.4}$$

where $\vec{S}$ is the spin vector, $\vec{B}_\perp$ and $\vec{B}_\parallel$ are the transverse and longitudinal components of the magnetic field with respect to particles velocity vector $\vec{v}$, $\vec{E}$ is the electric field, $\vec{\beta} = \vec{v}/c$ is the normalized velocity and G is the anomolous magnetic moment for spin 1/2,

$$G = \frac{g-2}{2}. \tag{1.3.5}$$

Gγ is the number of times the spin vector precesses in one turn of a perfect ring which

is the spin tune, ν_s. From Eq. 1.3.4 it is clear that transverse magnetic fields produce rotations that scale with energy. Due to the lack of transverse electric fields, the term dependent on $\vec{E}$ will be ignored.

The Thomas-BMT equation in the Frénet-Serret coordinate system is given by

$$\frac{d\vec{S}}{d\theta} = \vec{S} \times \vec{F} \tag{1.3.6}$$

where θ is the bending angle from a main dipole and with

$$\vec{F} = F_1\hat{x} + F_2\hat{s} + F_3\hat{y} \tag{1.3.7}$$

where $\vec{F}$ is expressed in the particle coordinates

$$\begin{aligned} F_1 =& -\rho\frac{d^2y}{ds^2}(1+G\gamma), \\ F_2 =& (1+G\gamma)\frac{dy}{ds} - \rho(1+G)\frac{d}{ds}\left(\frac{y}{\rho}\right), \\ & \text{and} \\ F_3 =& -(1+G\gamma) + (1+G\gamma)\rho\frac{d^2x}{ds^2} \end{aligned} \tag{1.3.8}$$

In the frame that rotates with the particle, the Thomas-BMT is

$$\frac{d\vec{S}}{d\theta} = \vec{n} \times \vec{S} \tag{1.3.9}$$

with

$$\vec{n} = -F_1\hat{x} - F_2\hat{s} + G\gamma\hat{y} \tag{1.3.10}$$

Defining a two component spinor for a spin-1/2 particle

$$\psi = \begin{pmatrix} \mathrm{u} \\ \mathrm{d} \end{pmatrix} \tag{1.3.11}$$

where u and d represent the up and down states. The spin vector is

$$S_i =< \psi|\sigma_i|\psi > \tag{1.3.12}$$

where i denotes the x, s and y components, and σ_{i} are the Pauli spin matrices for spin-1/2 defined as

$$\sigma_x = \begin{bmatrix} 0 & 1 \\ 1 & 0 \end{bmatrix},\ \sigma_s = \begin{bmatrix} 0 & -i \\ i & 0 \end{bmatrix},\ \sigma_y = \begin{bmatrix} 1 & 0 \\ 0 & -1 \end{bmatrix} \tag{1.3.13}$$

Eq.1.3.6 becomes

$$\frac{d\psi}{d\theta} = \frac{-i}{2}(\vec{\sigma}\cdot\vec{n})\psi = -\frac{i}{2}\begin{bmatrix} G\gamma & -\xi(\theta) \\ -\xi(\theta)^* & -G\gamma \end{bmatrix}\psi \tag{1.3.14}$$

where

$$\xi(\theta) = F_1 - iF_2 \tag{1.3.15}$$

which characterizes the depolarizing kicks that couple the up and down spin components. $\xi(\theta)$ can be expanded in Fourier series yielding

$$\xi(\theta) = \sum_K \epsilon_K e^{-iK\theta} \tag{1.3.16}$$

where ϵ_{K} is the Fourier amplitude, or the resonance strength. The resonance strength writes,

$$\epsilon_K = -\frac{1+G\gamma}{2\pi}\oint \frac{d^2y}{ds^2}e^{iK\theta}ds = \frac{1+G\gamma}{2\pi}\oint \frac{\frac{\partial B_y}{\partial x}}{B\rho}ye^{iK\theta}ds \tag{1.3.17}$$

and

$$y = y_{co} + y_\beta \tag{1.3.18}$$

where $\mathrm{y_{co}}$ is defined in Eq. 1.2.53 and y_β is defined in Eq. 1.2.24 with y in place of x. The two types of depolarizing spin resonances that satisfy these conditions are imperfection resonances and intrinsic resonances. Imperfection resonances occur as a result of vertical

closed orbit errors when [34],

$$K = G\gamma = k \tag{1.3.19}$$

where k is an integer. Vertical intrinsic resonances occur as the result of vertical betatron motion and the horizontal field experienced in quadrupoles. These resonances occur when this condition is satisfied [34],

$$K = G\gamma = nP \pm \nu_y \tag{1.3.20}$$

where n is an integer and P is the superperiodicity of the accelerator.

Table 1.2: Physical parameters (m_o, q, G) for protons and helions.

species	m_o [MeV]	q [e]	G
protons	938.272	1	1.7928
helions	2808.391	2	-4.1842

1.3.1 Imperfection Resonances

By substituting Eq. 1.2.53 for y in Eq. 1.3.17 the resonance strength for imperfection resonances becomes

$$\epsilon_K = \frac{1+G\gamma}{2\pi} \sum_{k=-\infty}^{\infty} \frac{\nu_y^2 f_k}{\nu_y^2 - k^2} \oint \frac{\frac{\partial B_y}{\partial x}}{B\rho} \beta_y^{1/2}(s) e^{ik\phi_y(s)} e^{iK\theta} ds. \tag{1.3.21}$$

As this occurs when $|G\gamma| = k$, the corresponding orbit harmonic can be corrected with Eq. 1.2.55, or strengthened to enhance the resonance strength.

The energy spacing between imperfection resonances is [39],

$$\Delta_{imp} = \frac{m_o/q}{G}. \tag{1.3.22}$$

For protons $\Delta_{\text{imp}} = 523.34$ MeV whereas the spacing between resonances for helions is $\Delta_{\text{imp}} = 335.60$ MeV. By comparing the two spacings, one can infer that helions will cross 1.56 more resonances per unit change in energy. Because of this closer spacing, as helions are accelerated to the same γ as protons they have the potential of crossing three intrinsic

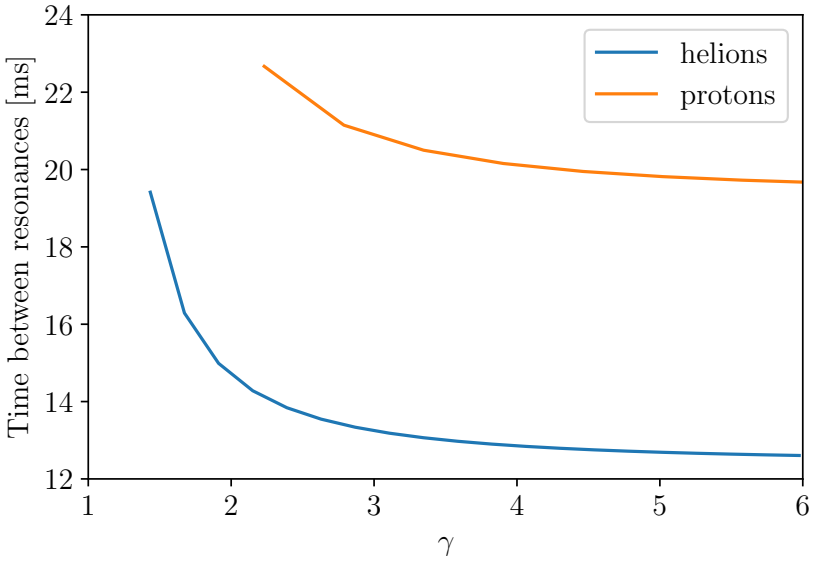

Figure 1.12: Time separation of resonances (ms) vs γ for protons and helions.

resonances and six imperfection resonances in the Booster. With a nominal ramp rate of 6.5 T/s the timing of these resonances will approach a separation of 12.6 ms for helions, and 19.7 ms for protons, as seen in Fig. 1.12

1.3.2 Intrinsic Resonances

By substituting Eq. 1.2.24 into Eq. 1.3.17 the intrinsic resonance strength is defined as

$$\epsilon_K = \frac{1+G\gamma}{2\pi}\sqrt{\frac{\varepsilon_N}{\pi\gamma}}\oint \frac{\frac{\partial B_y}{\partial x}}{B\rho}\beta_y^{1/2}(s)\cos(\nu_y\phi_y(s)+\xi)e^{iK\theta}ds. \tag{1.3.23}$$

1.3.3 Crossing of an Isolated Resonance

A particle is accelerated through a resonance with crossing speed α defined as [34, 40]

$$\alpha = \frac{dG\gamma}{d\theta} = G\frac{1}{2\pi}\frac{\Delta E}{m_o} \tag{1.3.24}$$

where ΔE is the change in energy per turn and $d\theta$ is the change in azimuthal angle. The Froissart-Stora Formula [40],

$$\frac{P_f}{P_i} = 2\exp\Big(-\frac{\pi}{2}\frac{|\epsilon_K|^2}{\alpha}\Big) - 1 \tag{1.3.25}$$

relates the asymptotic values of the polarization after the resonance, P_f, and the initial polarization before the resonance, P_i, for a beam accelerated through a resonance of strength ϵ_K at a crossing speed of α.

If the resonance is sufficiently weak, that is $P_f \sim P_i$, the motion of the spin as it crosses the resonance is well represented by a model of Fresnel integrals of the form [39],

- upstream of the resonance($\theta < 0$),

$$\frac{P(\theta)}{P_i} = 1 - \frac{\pi}{\alpha}|\epsilon_K|^2\left[\left(0.5 - C\left(-\theta\sqrt{\frac{\alpha}{\pi}}\right)\right)^2 + \left(0.5 - S\left(-\theta\sqrt{\frac{\alpha}{\pi}}\right)\right)^2\right] \tag{1.3.26}$$

- downstream of the resonance($\theta > 0$),

$$\frac{P(\theta)}{P_i} = 1 - \frac{\pi}{\alpha}|\epsilon_K|^2\left[\left(0.5 - C\left(\theta\sqrt{\frac{\alpha}{\pi}}\right)\right)^2 + \left(0.5 - S\left(\theta\sqrt{\frac{\alpha}{\pi}}\right)\right)^2\right] \tag{1.3.27}$$

where

$$C(x) = \int_0^x \cos\left(\frac{\pi}{2}t^2\right)dt, \qquad S(x) = \int_0^x \sin\left(\frac{\pi}{2}t^2\right)dt \tag{1.3.28}$$

Static depolarization [39] occurs when $\vec{S}$ is allowed to oscillate at fixed energy with a close proximity Δ to the resonance, defined by [39],

$$\Delta = G\gamma - K \tag{1.3.29}$$

The average of these oscillations at a given Δ writes,

$$\bar{S}_y^2 = \frac{1}{1 + |\epsilon_K|^2/\Delta^2} \tag{1.3.30}$$

The resonance strength $|\epsilon_K|$ and the resonance proximity Δ can be found numerically with appropriate simulation of the vertical polarization component, S_y.

Any of these methods (Eqs. 1.3.25, 1.3.30, 1.3.26, 1.3.27) can be used for determining resonance strength through simulation.

For a beam with Gaussian beam distribution of Eq. 1.2.29 that crosses a resonance,

Eq. 1.3.25 can be applied as

$$\left\langle \frac{P_f}{P_i} \right\rangle = \int_0^\infty [2e^{-\frac{\pi|\epsilon_K|^2}{2\alpha}} - 1]\rho(y)dy = \frac{1 - \frac{\pi|\epsilon_K|^2}{\alpha}}{1 + \frac{\pi|\epsilon_K|^2}{\alpha}} \tag{1.3.31}$$

1.3.4 Spin Dynamics with two Partial snakes

To preserve polarization of proton beams in the AGS, two partial Siberian snakes are used [28]. The AGS partial snakes rotate the spin an amount less than π. One of these snakes is super conducting, known as the cold snake, and rotates the spin by $\chi_c = 14\%\pi$. The other partial snake is normal conducting, known as the warm snake, and rotates the spin by $\chi_w = 5.9\%\pi$.

The spin tune in this dual partial snake configuration is [28]

$$\nu_s = \frac{1}{\pi}\cos^{-1}\left[\cos\frac{\chi_c}{2}\cos\frac{\chi_w}{2}\cos(G\gamma\pi) - \sin\frac{\chi_c}{2}\sin\frac{\chi_w}{2}\cos(G\gamma\frac{\pi}{3})\right] \tag{1.3.32}$$

where the $\pi/3$ term is from the relative separation of the two snakes being one third of the ring. It is also important to note that $\nu_s \neq G\gamma$ with snakes. The projection of the

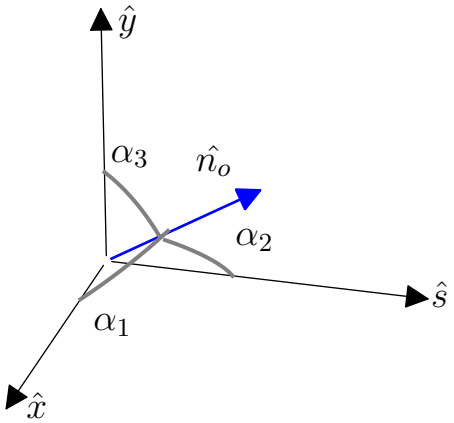

Figure 1.13: The angles between the spin vector and the corresponding axis.

stable spin direction on the vertical axis is given by

$$\cos\alpha_3 = \frac{1}{\sin\ \pi\nu_s}\left[\cos\frac{\chi_w}{2}\cos\frac{\chi_c}{2}\sin(G\gamma\pi) - \sin\frac{\chi_w}{2}\sin\frac{\chi_c}{2}\sin(G\gamma\frac{\pi}{3})\right] \tag{1.3.33}$$

and on the horizontal and longitudinal axes is,

$$\cos\alpha_1 = \frac{-1}{\sin\ \pi\nu_s}\left[\cos\frac{\chi_w}{2}\sin\frac{\chi_c}{2}\sin\big(G\gamma(\pi-\theta)\big)+\sin\frac{\chi_w}{2}\cos\frac{\chi_c}{2}\sin\big(G\gamma(\frac{\pi}{3}-\theta)\big)\right] \tag{1.3.34}$$

and

$$\cos\alpha_2 = \frac{1}{\sin\ \pi\nu_s}\left[\cos\frac{\chi_w}{2}\sin\frac{\chi_c}{2}\cos\big(G\gamma(\pi-\theta)\big) + \sin\frac{\chi_w}{2}\cos\frac{\chi_c}{2}\cos\big(G\gamma(\frac{\pi}{3}-\theta)\big)\right]. \tag{1.3.35}$$

The vertical component of the stable spin direction, $\cos\alpha_3$, will be nearest vertical every

$$G\gamma = 3n + 1.5. \tag{1.3.36}$$

The stable spin direction in the Booster is always vertical away from the resonances. To facilitate spin matching between the Booster and AGS, extraction from Booster must be constrained to Eq. 1.3.36 or otherwise cause polarization loss.

Snakes are primarily used for avoiding imperfection resonances since they ensure $\nu_s \neq k$. The region where this condition is satisfied is the spin tune gap. During normal operations, the vertical tune is set above 8.9 to be inside the spin tune gap and avoid most resonances [29]. Eq. 1.3.32 and Eq. 1.3.33 with χ_w=5.9% and χ_c=14% are shown in Fig. 1.14, also making the periodicity of Eq. 1.3.36 obvious.

The cold snake for protons has a nominal field of 2.1 T. This field produces strong optical defects that reduce the dynamic aperture at injection and constrain the tune space the beam can occupy. With protons injection into AGS at Gγ = 4.5 it would be beneficial for ν_y to be placed inside the spin tune gap at injection to avoid polarization loss at the $G\gamma = 5$ resonance.

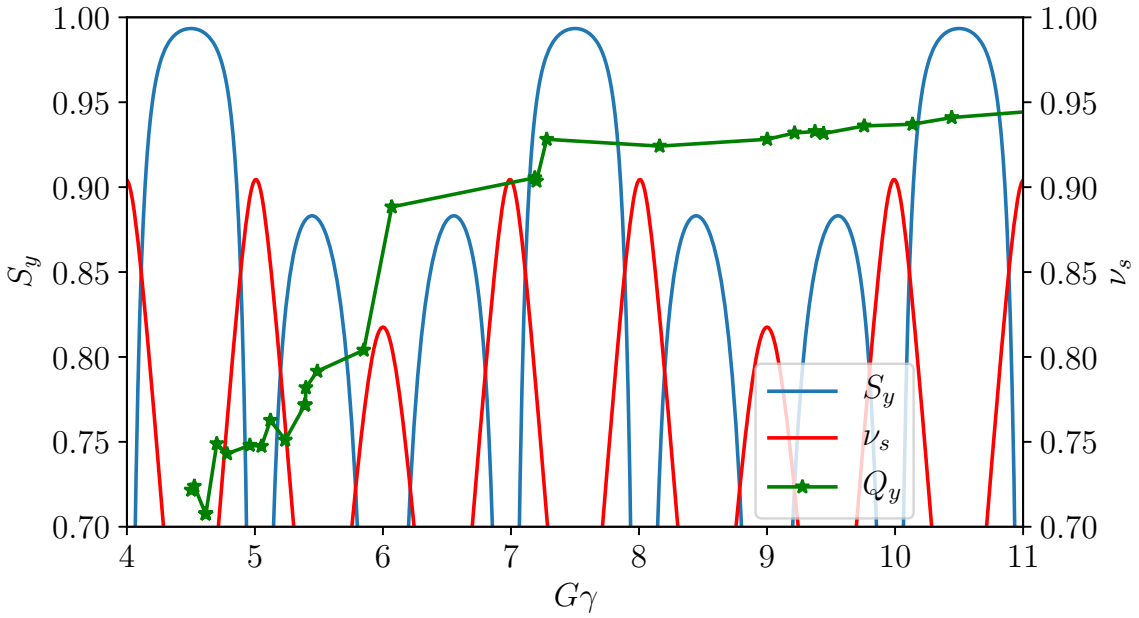

Figure 1.14: Spin tune ν_s (Eq. 1.3.32), vertical tune Q_y, and the vertical component of the stable spin direction in the AGS, S_y (Eq. 1.3.33). The periodicity of Eq. 1.3.36 is also clear

1.3.4.1 Fast Tune Jump Method

From Eq. 1.3.25, increasing the crossing speed will minimize polarization loss. The free parameter in Eq. 1.3.24 is ΔE, is limited by the the maximum voltage of the RF cavities. The tune jump changes the crossing speed by rapidly changing ν_{y} by an amount of $\Delta\nu_{\mathrm{y}}$/turn with modified crossing speed

$$\alpha = G\frac{d\gamma}{dt} \pm \frac{d\nu_y}{dt}. \tag{1.3.37}$$

See Fig. 1.15 for a sketch. Use of this method is avoided when possible since it may result in emittance dilution. This method was used for intrinsic resonances in the AGS prior to the installation of the two partial snakes. In the presence of partial snakes the stable spin direction has a horizontal component which causes horizontal intrinsic resonances to become present. These horizontal intrinsic resonances are crossed using the tune jump method [29].

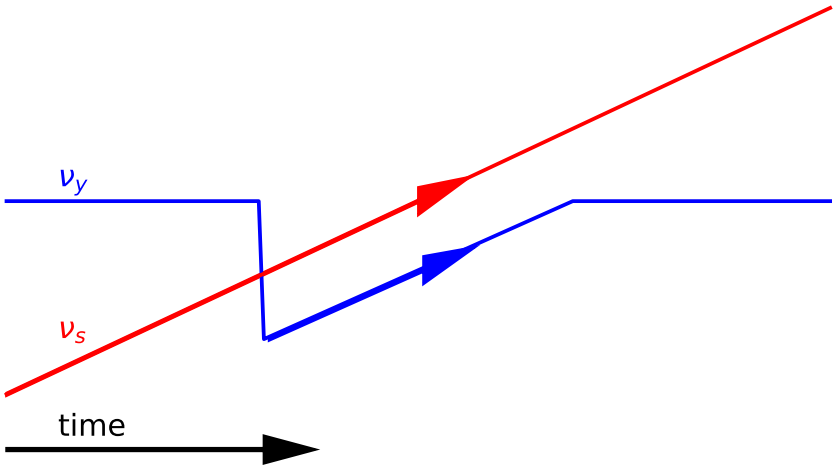

Figure 1.15: A sketch of a resonance crossing using the fast tune jump method.

1.3.5 Spin Dynamics with an AC dipole

In the case of protons in the Booster, only weak imperfection resonances are crossed and polarization is preserved by exciting or correcting orbit harmonics. This technique cannot be used to overcome intrinsic resonances and only applies to imperfection resonances. Intrinsic resonances can be overcome through use of an AC dipole. An AC dipole is a dipole magnet designed to drive large amplitude oscillations (Eq. 1.2.61) by oscillating at a frequency near the betatron frequency. The oscillation amplitude is ramped up as the intrinsic resonance is approached, and maintains its high amplitude through the resonance. The beam thus samples strong horizontal fields in the quadrupoles, so increasing the resonance strength and inducing a full spin-flip [36]. An AC dipole was first used for polarization transmission in the AGS.

The coherent betatron amplitude is given by Eq. 1.2.61. The AC dipole enhances the corresponding intrinsic resonances by,

$$\epsilon_{AC} = \frac{\epsilon_K Y_{coh}}{\sigma_y} \tag{1.3.38}$$

Using Eq. 1.3.31 to analyze P_f/P_i when a Gaussian beam distribution is undergoing vertical betatron oscillations, the distribution function writes [34, 41]

$$g(Y, Y') = \frac{1}{2\pi\sigma_y^2} \exp\left(- \frac{(Y + Y_{coh})^2 + Y'^2}{2\sigma_y^2} \right) \tag{1.3.39}$$

This leads to the following [41],

$$\left\langle \frac{P_f}{P_i} \right\rangle = \frac{2}{1 + \pi|\epsilon_K|^2/\alpha} \exp\left(- \frac{(Y_{coh}^2/(2\beta_y\sigma_y^2))(\pi|\epsilon_K|^2/\alpha)}{1 + \pi|\epsilon_K|^2/\alpha} \right) - 1 \tag{1.3.40}$$

Rearranging Eq. 1.3.40, the bunched beam requirement for a 99% spin flip can be approximated to,

$$Y_{coh} \geq \left[- 2\beta_y \left(1 + \frac{\alpha}{\pi|\epsilon_K|^2} \right) \ln\left(0.005 \left(1 + \frac{\pi|\epsilon_K|^2}{\alpha} \right) \right) \right]^{1/2} \sigma_y \tag{1.3.41}$$

which is sufficient for a single, well-isolated, resonance. Due to the artificial resonance created at δ away from the intrinsic resonance, simulations are required to get the magnet strength for a spin-flip.

Chapter 2

Booster Model and Simulations

2.1 Development of the Booster Model in Zgoubi

The Booster model was developed in Zgoubi [42] to match the model developed using MADx [43] which closely matches the machine parameters [44]. Having a model in Zgoubi allows for direct spin tracking of particles while having a second numerical model for supporting results from MADx. MADx calculates particle trajectories and parameters by matrix transport where Zgoubi tracks particles with a Taylor expansion of field components which, if enabled, allows direct spin tracking. Comparisons of the two models' tunes are shown in Fig. 2.1. Comparisons of $\beta_x(s)$, $\beta_y(s)$, and $D_x(s)$ are shown for protons in Fig. 2.2, and comparisons of key optical parameters (ν_x, ν_y, ξ_x, ξ_y, $\beta_{y,max}$, and $\beta_{y,min}$) for protons and helions at relevant resonances are shown in Tab. 2.1. Note in Fig. 2.1, there is a decrease in Q_x and Q_y with increased main magnet current which is caused by saturation of the main quadrupoles [45]. Simulations are performed with both models: spin tracking and beam dynamics are performed with Zgoubi, MADx is used to verify the optics from the Zgoubi model and for using DEPOL [46] to verify Zgoubi spin tracking results.

Note in the selection of Tab. 2.1, the differences in betatron tunes are on the order of 10^{-4} where the differences in the vertical chromaticities are on the order of 10^{-1}. This arises from differences in the magnet models used for a dipole in Zgoubi and MADx.

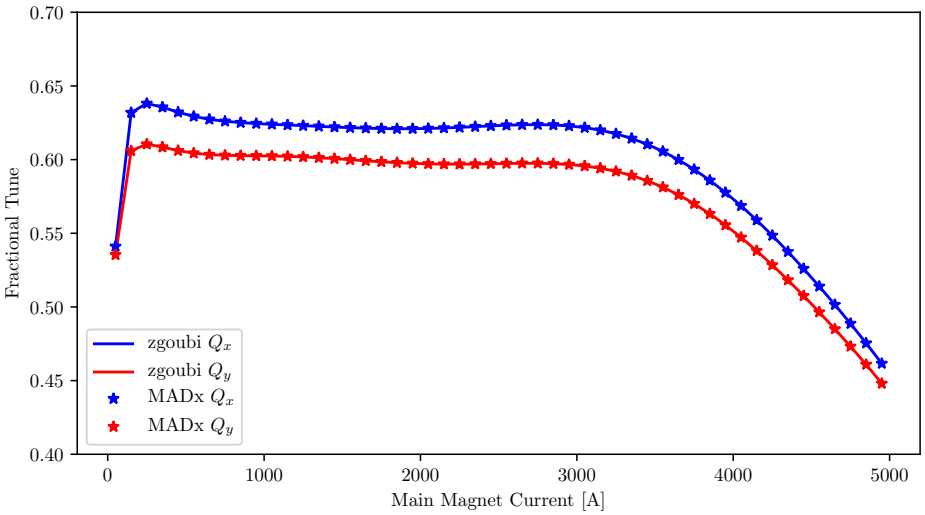

Figure 2.1: Bare tunes of the Booster lattice (no trim quadrupole current) from MADx and Zgoubi models.

Table 2.1: Table comparing key optical features of the Zgoubi and MADx models.

	Model	C [m]	$\nu_x,\ \nu_y$	$\xi_x,\ \xi_y$	$\beta_{y,max},\ \beta_{y,min}$ [m]
Protons	MADx	201.78000	4.6120, 4.8088	-7.947, -2.845	13.071, 3.906
$\lvert G\gamma\rvert = 0 + \nu_y$	Zgoubi	201.78002	4.6120, 4.8091	-7.378, -2.640	13.072, 3.905
Helions	MADx	201.78000	4.6150, 4.1891	-8.339, -2.195	13.916, 4.690
$\lvert G\gamma\rvert = 12 - \nu_y$	Zgoubi	201.78002	4.6154, 4.1888	-7.950, -1.946	13.917, 4.690
Helions	MADx	201.78000	4.6420, 4.1744	-7.699, -2.075	13.962, 4.705
$\lvert G\gamma\rvert = 6 + \nu_y$	Zgoubi	201.78002	4.6425, 4.1744	-6.917, -2.000	13.965, 4.705

The dipoles in Booster do not have a pure dipole field but exhibit higher order field components with [44, 47]

$$K_1 = -0.003571 - 2.520 \times 10^{-6} I_{MM} + 6.145 \times 10^{-8} I_{MM}^2 + ... \tag{2.1.1}$$

and

$$K2 = (-0.4438)/\rho \tag{2.1.2}$$

with I_{MM} being the main magnet current.

The sector dipole model in Zgoubi and MADx calculate these gradients differently, as seen in Fig. 2.3 where the particle trajectory is shown as the reference orbit relative to the constant field line $B_1 = 0$. The gradient in the Zgoubi dipole model causes a slight change in the path length and reference orbit. To compensate this change in the reference

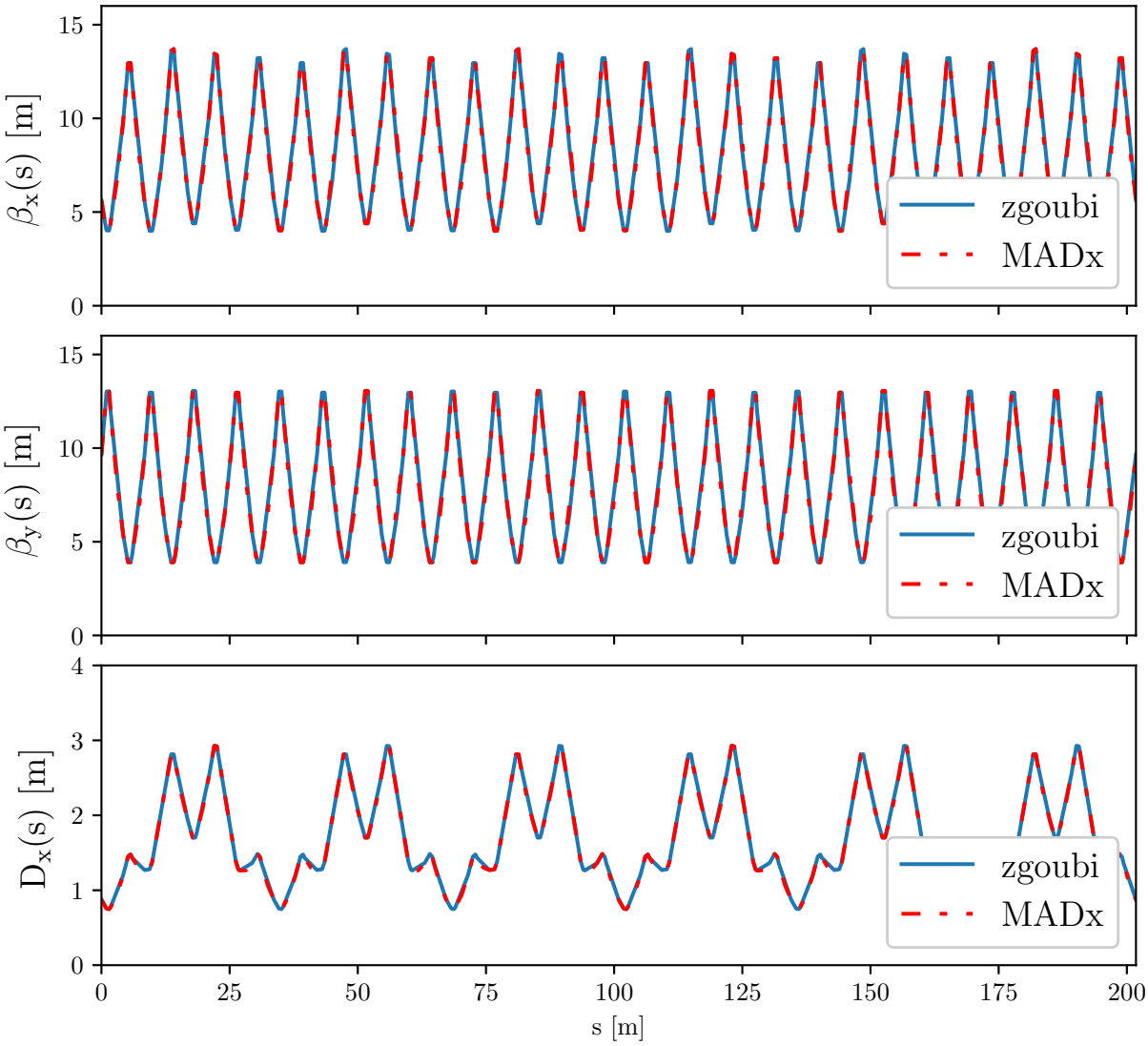

Figure 2.2: Comparison of β_x, β_y, and D_x between Zgoubi and MADx.

orbit, the position of the reference particle is adjusted so the entrance position and angle is the same as its exit, making the orbit through the dipole symmetric. To compensate the change in path length, the magnetic field in the dipole is scaled appropriately.

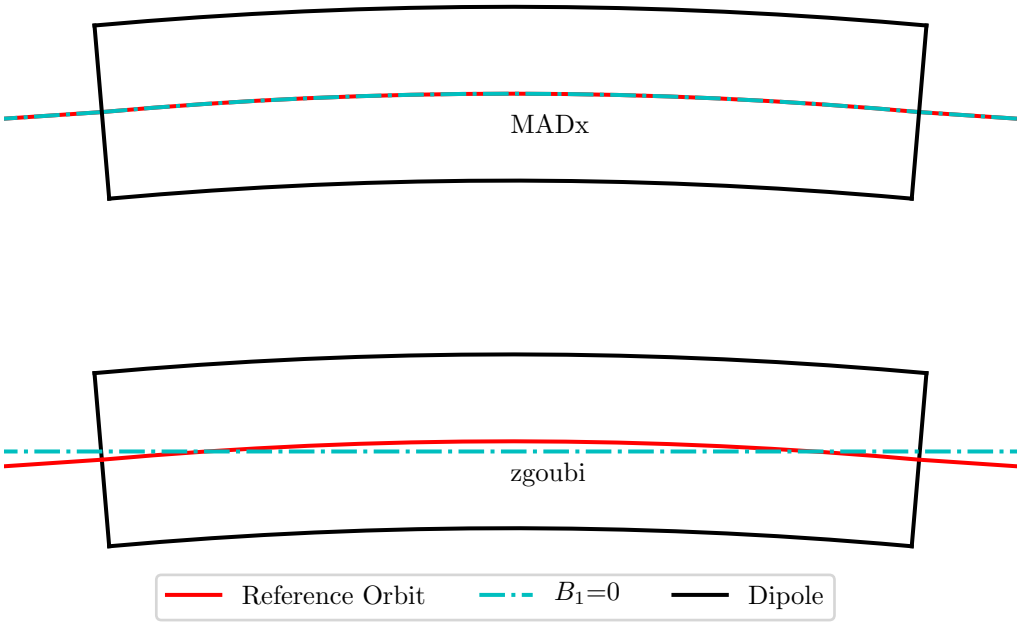

Figure 2.3: Image showing how the computation of gradient in the dipole varies from MADx and Zgoubi (using keyword BEND).

2.1.1 PyZgoubi

After initial developments in Zgoubi, the model was converted into PyZgoubi. PyZgoubi generates and executes the Zgoubi input files via python which provides access to the many modules python has to offer [48]. This particular model calculates all necessary parameters to start a simulation at a given value of $G\gamma$. The PyZgoubi input file has a multi-threading procedure implemented that allows the user to control: threads used, particles per thread, and number of batches. This implementation of multi-threading provides a versatile setup that can be optimized depending on the computer the simulations are being run on. The machine these simulations were primarily run on has 32 Threads available and a base clock speed of 2.9 GHz. Nominal simulations are run using 25 threads with 4 particles per thread and batches are used to scale the total number of particles for the simulation.

2.2 Resonance Strength Calculations

In order to ensure accuracy of the model and the calculations, resonance strengths are calculated using a number of methods and using Zgoubi and MADx. Resonance strengths are calculated by simulation using the Froissart-Stora formula (Eq. 1.3.25), the Fresnel integral (Eq. 1.3.26 and Eq. 1.3.27, intrinsic resonances only), using the static method (Eq. 1.3.30); and by optics output by Zgoubi using Eq. 1.3.21 and MADx using DEPOL [46]. An example of a single proton crossing the G$\gamma = 0 + \nu_{\mathrm{y}}$ resonances is shown in Fig. 2.4 and Fig. 2.5, while Fig. 2.6 shows a single proton with the static method. The results for helions are shown in App. B.1.3. Results of the calculations are shown in Tab. 2.2 for intrinsic resonances and Tab. 2.6 for imperfection resonances.

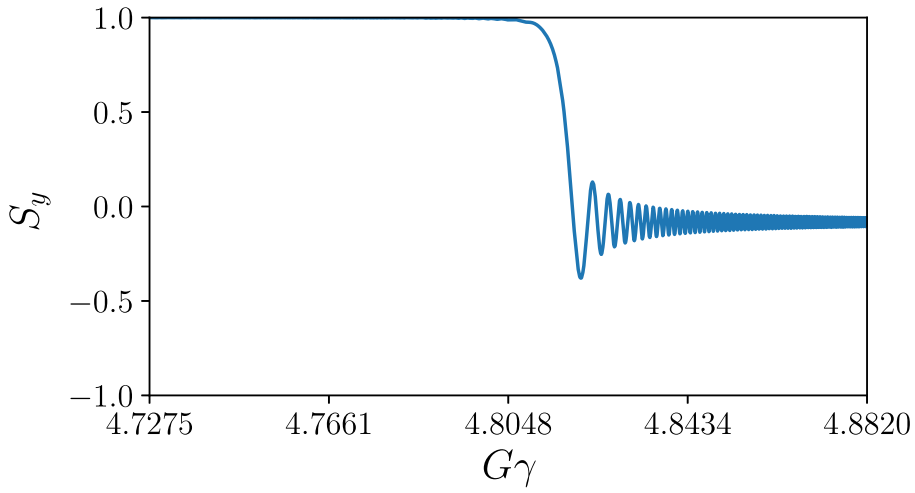

Figure 2.4: Single proton crossing the $G\gamma = 0 + \nu_y$ resonance. The asymptotic value of the polarization after crossing the resonance is used to determine the resonance strength by the Froissart-Stora formula, Eq. 1.3.25.

2.3 Intrinsic Resonance Crossing

With an AC dipole frequency of f_m =250 kHz, protons have a constrained vertical tune of ν_y=4.8089 to cross $|G\gamma| = 0 + \nu_y$ while maintaining $\delta_m \leq 0.01$. For helions crossing $|G\gamma| = 12 - \nu_y$ the vertical tune is constrained to ν_y=4.192, and to ν_y=4.174 for the $|G\gamma| = 6 + \nu_y$ resonance. For the simulations, the total number of particles, N_{total}, are

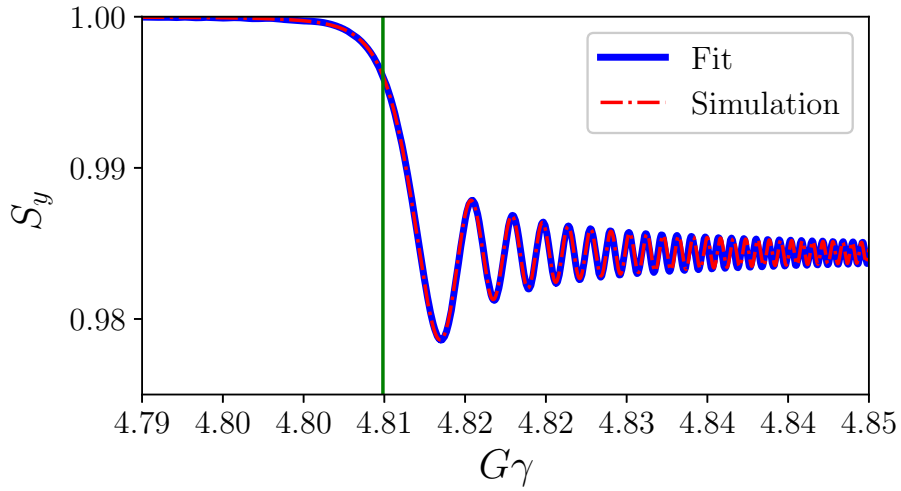

Figure 2.5: Single proton crossing the $G\gamma = 0 + \nu_y$ resonance. S_y is fitted with the Fresnel-integrals to determine ϵ_K (Eq. 1.3.26 and Eq. 1.3.27) which are separated by the green line.

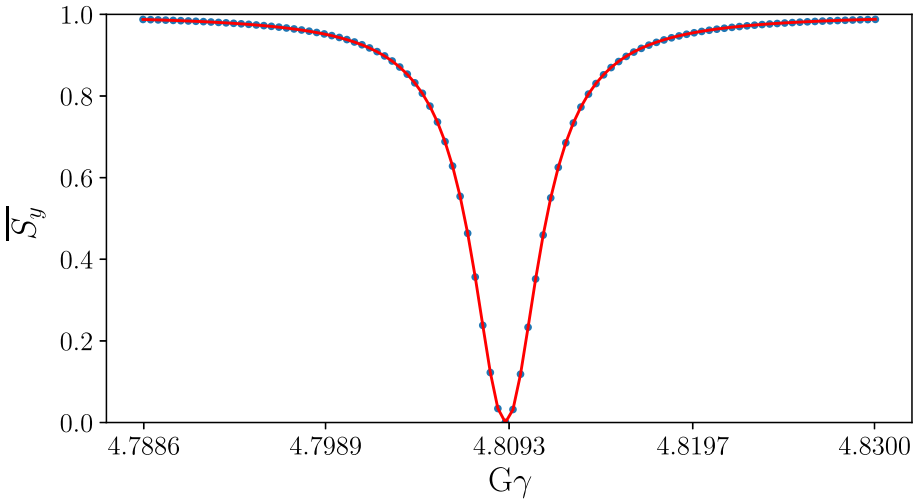

Figure 2.6: Single proton crossing the $G\gamma = 0 + \nu_y$ resonance. S_y is fitted with the static depolarization method 1.3.30.

1,000 with initial parameters shown in Tab. 2.4. 1,000 particles are sufficient to minimize errors and also provide suitable resolution of binned particles that are fit for determining emittance growth, as seen in Fig. 2.7. These parameters are also used in the imperfection resonance case where applicable.

To ensure there is minimal emittance growth, the distribution of particles is binned and fitted with a Gaussian. The width of the distribution at the end of the simulation is compared to the beginning, the ratio of which is ϵ_{ratio}. The vertical limiting aperture

Table 2.2: Summary of intrinsic resonance strengths calculated with various methods. $\alpha_{protons} = 5.105 \times 10^{-6}$; helion crossing $|G\gamma| = 12 - \nu_y$ resonance uses a fast ramp rate of $\alpha_{^3He,12-} = 7.961 \times 10^{-6}$ where the $|G\gamma| = 6 + \nu_y$ resonance crossing uses a slow ramp rate of $\alpha_{^3He,6+} = 2.6537 \times 10^{-6}$. These results are compared with results from DEPOL, which calculates the resonance strength from a MADx Twiss file using DEPOL.

	Resonance	Froissart-Stora		Fresnel Integral		Static		DEPOL
$\varepsilon_y(\mu m)$		ϵ_K	P_f	ϵ_K	ν_y	ϵ_K	ν_y	ϵ_0
Protons								
0.001	$0 + \nu_y$	0.000160	0.984	0.000160	4.8091	0.000161	4.8091	0.000161
0.1		0.001592	-0.083			0.001606	4.8091	0.001614
0.234						0.002463	4.8091	0.002469
10						0.016205	4.8094	0.016137
helion								
0.001	$12 - \nu_y$	0.000135	0.993	0.000135	7.8079	0.000132	7.8082	0.000130
0.1		0.001350	0.396			0.001319	7.8082	0.001303
0.535						0.003037	7.8082	0.003013
10						0.013319	7.8082	0.013027
0.001	$6 + \nu_y$	0.000229	0.933	0.000238	10.1739	0.000226	10.1742	0.000224
0.1		0.002291	-0.916			0.002265	10.1742	0.002235
0.369						0.004396	10.1742	0.004294
10						0.022826	10.1742	0.022353

0

Table 2.3: Summary of imperfection resonance strengths for protons and helions with quadrupole alignment based on Fig. 2.9a.

Species	k	$B\rho$ $[T \cdot m]$	ϵ_K		
			Froissart-Stora	Static	Eq. 1.3.21
Protons					
	3	4.198	0.000737	0.000714	0.000644
	4	6.240	0.002238	0.002367	0.002396
helions					
	5	3.064	-	0.004605	0.004492
	6	4.814	0.000684	0.000701	0.000716
	7	6.282	0.001283	0.001299	0.001158
	8	7.633	0.003444	0.003582	0.003834
	9	8.920	0.000223	0.000226	0.000239
	10	10.167	-	0.006252	0.006646

Table 2.4: Table of the horizontal, vertical, and longitudinal spatial dimensions used for simulations. σ_p being the width of the momentum distribution.

	protons	helions
$\varepsilon_{x,NRMS}$	1.1 mm mrad	1.6 mm mrad
$\varepsilon_{y,NRMS}$	1.1 mm mrad	1.6 mm mrad
σ_p	1.39×10^{-3}	1.19×10^{-3}

of the machine is placed in the Zgoubi model using the Zgoubi keyword, COLLIMA. If a particle is lost on the aperture, it is added to the total number of particles lost, $N_{scraped}$.

2.3.1 Protons

Cases of protons crossing the $|G\gamma| = 0 + \nu_y$ resonance using the AC dipole are shown in Fig. 2.7. The top image shows S_y motion across the resonance, and shows a full spin-flip. The middle plot shows the envelope of the beam during the AC dipole pulse. The bottom image shows a comparison of initial and final normalized vertical beam distributions. The AC dipole has $B_m l = 15.5$ G $\cdot$ m and has a pulse of [N_{up}, N_{flat}, N_{down}]=[2500, 3000, 2500] in turns, δ_m=0.01.

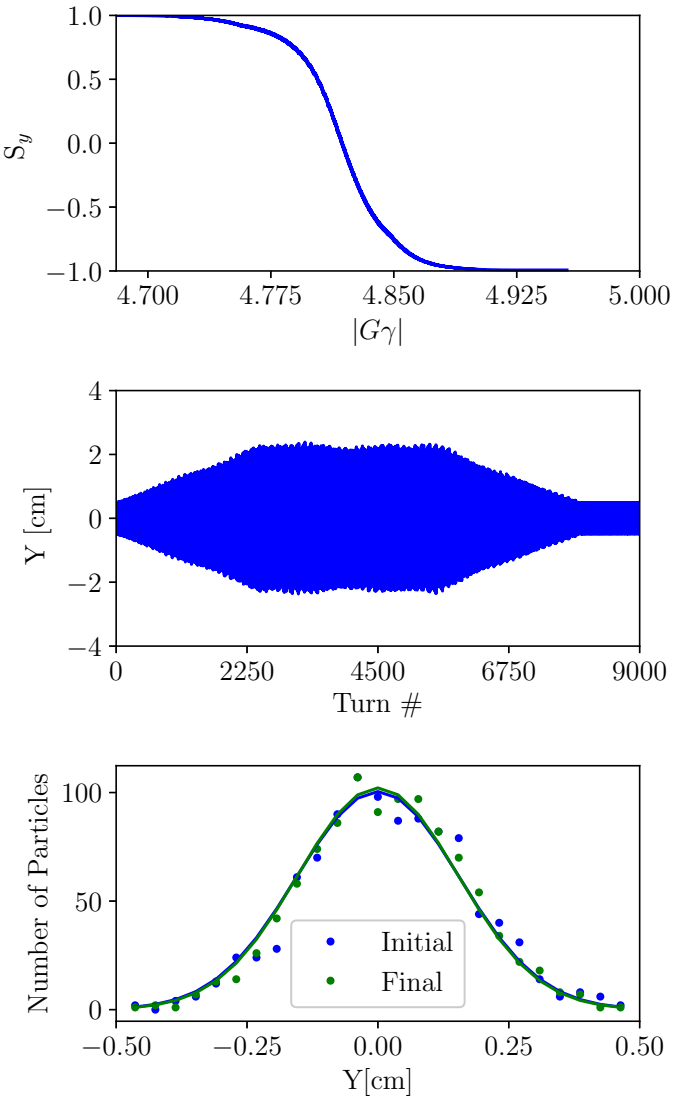

Figure 2.7: 1,000 protons tracked through the $G\gamma = 0 + \nu_y$ resonance using the AC dipole with: (top) the vertical component of the spin vector, the vertical position of the beam with turn, and a comparison of final and initial distributions.

2.3.2 helions

Cases of helions crossing the $|G\gamma| = 12 - \nu_y$ (left) and $|G\gamma| = 6 + \nu_y$ (right) resonances using the AC dipole are shown in Fig. 2.7. The top images show S_y motion across the resonance, and shows a full spin-flip. The middle plot shows the envelope of the beam during the AC dipole pulse. The bottom image shows a comparison of initial and final normalized vertical beam distributions. For $|G\gamma| = 12 - \nu_y$: the AC dipole has $B_m l = 16.5$ G $\cdot$ m and has a pulse of [N_{up}, N_{flat}, N_{down}]=[2500, 3000, 2500] in turns, δ_m=0.01. For $|G\gamma| = 6 + \nu_y$: the AC dipole has $B_m l = 20.5$ G$\cdot$m and has a pulse of [N_{up}, N_{flat}, N_{down}]=[4500, 7000, 4500] in turns, δ_m=0.01.

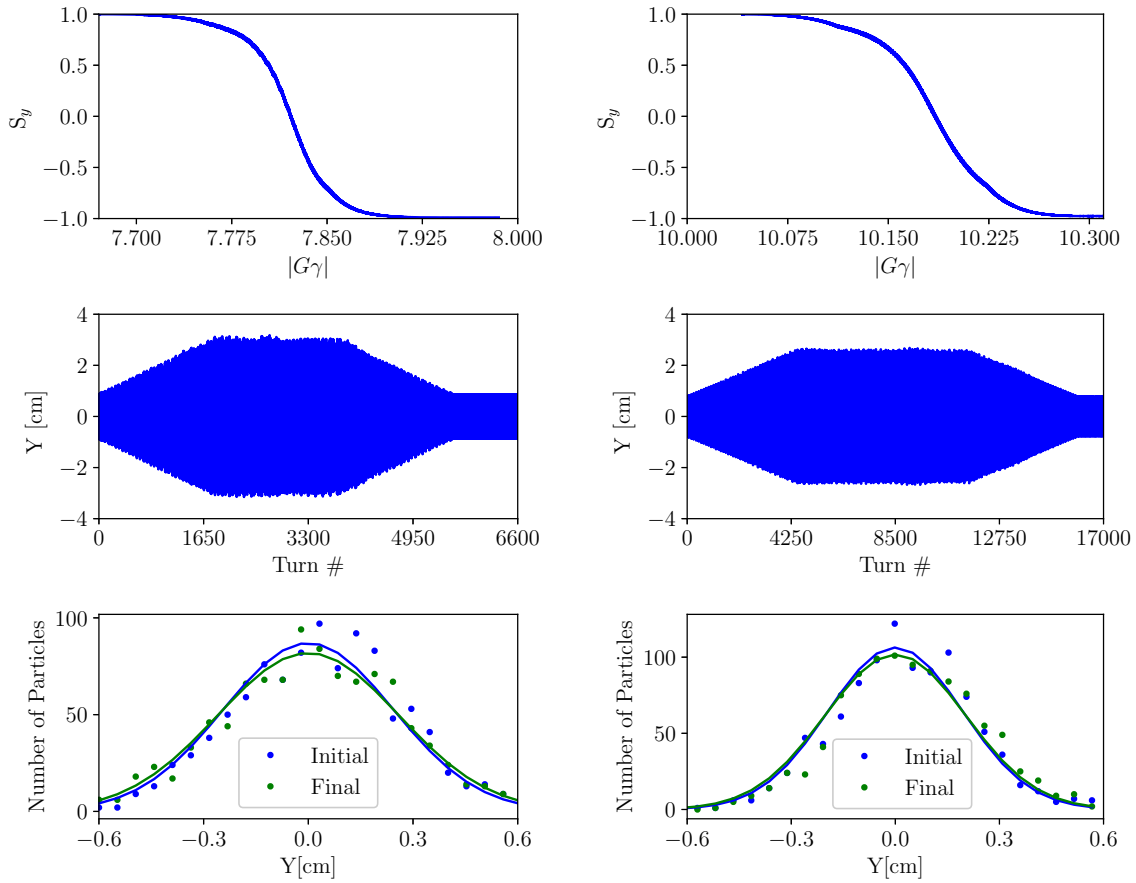

Figure 2.8: helion crossing $|G\gamma| = 12 - \nu_y$ (left) and $|G\gamma| = 6 + \nu_y$ (right). The top plot shows the ensemble average of the vertical component of the spin vector as it crosses the resonance. The middle plot shows the coherent motion of the bunch caused by the AC dipole. The bottom plot shows a comparison of the final and initial beam emittances.

2.3.3 Intrinsic Resonance Simulation Results

Results from these simulations are found in Tab. 2.5. The maximum $B_m l$ to achieve a full spin-flip is 20.5 G·m for helions crossing the $|G\gamma| = 6+\nu_y$ resonance. This maximum field strength was used to determine the design specification for the magnet and power amplifier design.

Table 2.5: Table summarizing beam parameters and corresponding AC dipole requirements and results from simulation.

	Protons	helions	
Resonance	$0+\nu_y$	$12-\nu_y$	$6+\nu_y$
ϵ_K	0.00246	0.00304	0.00440
σ_y [mm]	1.83	2.75	2.31
δ_m	0.01	0.01	0.01
$B_m \cdot l$ [G · m]	15.5	16.5	20.5
ν_y	4.809	4.192	4.174
ε_{ratio}	1.03	1.02	1.00
$N_{scraped}/N_{total}$[%]	0.0	1.2	0.0

2.4 Imperfection Resonance Crossing

2.4.1 Protons

To preserve polarization through imperfection resonances in the Booster, the orbit harmonic corresponding to the resonance being crossed (that is h=k) is either corrected to minimize polarization loss or enhanced to induce a spin-flip. At the start of a polarized proton run for RHIC, harmonic scans are performed in Booster to determine the optimal corrector current for each resonance to correct or enhance the orbit harmonic. This ensures the polarization transmission is lossless. These scans involve collection of polarization data, measured in AGS at injection, at various corrector current values of one family while the orthogonal family remains fixed. The particular dataset that was analyzed was taken by N. Kling and P. Adams in January of 2017.

2.4.1.1 Harmonic Orbit Corrections

Initial simulations use a single and dual misaligned quadrupoles, Eq. 1.2.49 and Eq. 1.2.51, which were able to match experimental results. However, for a single set of misalignments that satisfies both $G\gamma = 3,\ 4$ resonances, a minimum of 3 quadrupoles need to be used. The number of quadrupoles needed increases with each additional resonance. Because of this and a lack of experimental data for helions, the quadrupole misalignments from the most recent survey is used.

The quadrupole misalignments are sourced from survey, which are shown in Fig. 2.9a, and placed into the Zgoubi input files to allow comparison of simulation with experimental data. The overall amplitude of the quadrupole misalignments is scaled to 65% to match the experimental data. To emulate the misalignments, the Zgoubi keyword CHANGREF is used to change the position of the quadrupoles and leaving all other elements' positions fixed. Fig. 2.9b shows the orbit as output by Zgoubi where the spikes result from the use of CHANGREF. Fig. 2.9c shows the h=4, 5 corrected orbit, with differences resulting outside of CHANGREF filtered appropriately, and a baseline orbit that has no h=8 harmonic component. Fig. 2.9d shows the baseline subtracted orbit from Fig. 2.9c with [sin8v, cos8v]=[4.0 A, -13.0 A] and the resulting fit.

For helions, the h=4 orbit is corrected at $|\mathrm{G}\gamma| = 5$ and the correction found from the h=5 harmonic scan is scaled to all higher order resonances by the ratio of rigidity. That is the current to correct the h=4, 5 harmonic components for resonance k follows

$$I_{(h,|G\gamma|=k)} = I_{(h,|G\gamma|=5)} \frac{B\rho_{(|G\gamma|=k)}}{B\rho_{(|G\gamma|=5)}} \tag{2.4.1}$$

Which allows all imperfection resonances above $|G\gamma|$=5 to have simulations performed with the same orbit.

2.4.1.2 Harmonic Scans

The harmonic scans are performed using Zgoubi with comparison to polarization data. The proton polarization dataset compared to in Fig. 2.10 and Fig. 2.11 was taken on

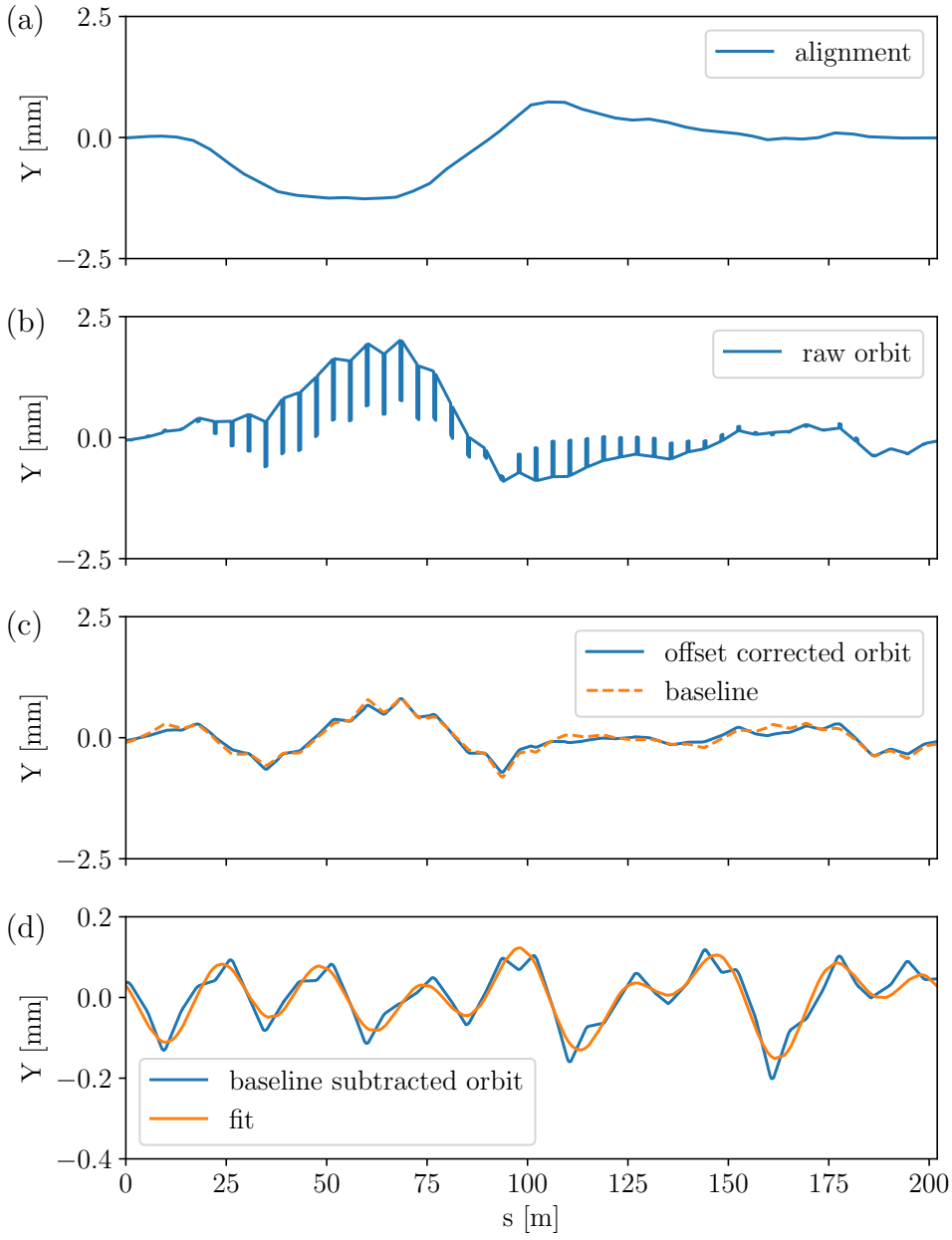

Figure 2.9: a) Vertical quadrupole misalignments in the Booster scaled to 65% to match h=4 data; b) orbit output from Zgoubi where discontinuities result from the quadrupole misalignments; c) Orbit after incorporating misalignments; d) Baseline subtracted orbit for helions crossing the $|G\gamma| = 8$ resonance after the h=4, 5 harmonics have been corrected with the addition of h=8. This example has corrector currents [sin4v, cos4v, sin5v, cos5v, sin8v, cos8v]=[2.797 $B\rho/B\rho(5)$, 0.669 $B\rho/B\rho(5)$, 0.520 $B\rho/B\rho(5)$, 4.296 $B\rho/B\rho(5)$, 4.0 ,-13.0]. The components of the fit results are: [sin4, cos4, sin5, cos5, sin8, cos8]=[0.000254, -0.000022, -0.000019, -0.000043, -0.000216, 0.000997].

January 12, 2017 with values:

[sin3v, cos3v]=[$\{-4.8 + 1\text{d}|\text{d} \in \{0, 1, 2, ..., 10\}\}$ A, -6.5 A],

[sin3v, cos3v]=[0.2 A, $\{-13 + 1\text{d}|\text{d} \in \{0, 1, 2, ..., 22\}\}$ A],

[sin4v, cos4v]=[$\{-10 + 2\text{d}|\text{d} \in \{0, 1, 2, ..., 10\}\}$ A, 2.0 A], and

[sin4v, cos4v]=[1.6 A, $\{-20 + 2\text{d}|\text{d} \in \{0, 1, 2, ..., 15\}\}$ A].

These scans are recreated in Zgoubi in an effort to improve the model so it gives accurate results and to determine the corrector current required for helion resonances. The $G\gamma = 3$ resonance harmonic scan is shown in Fig. 2.10 and the $G\gamma$=4 resonance harmonic scan is shown in Fig. 2.11.

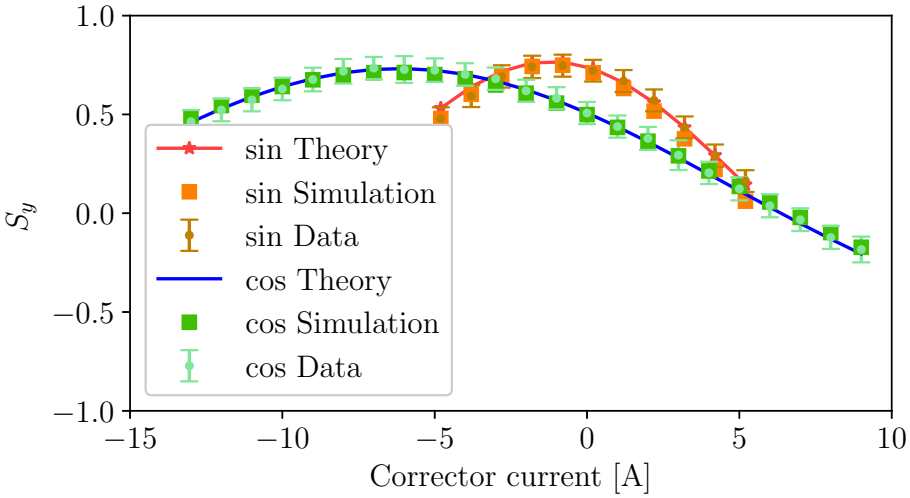

Figure 2.10: Harmonic scans of protons crossing the $G\gamma = 3$ resonance and comparisons between simulation, experimental data, and theory.

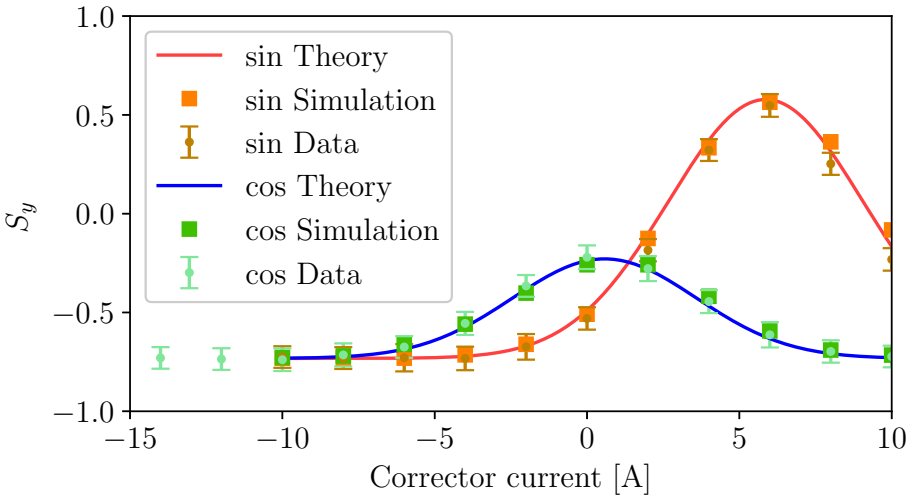

Figure 2.11: Harmonic scans of protons crossing the $G\gamma = 4$ resonance and comparisons between simulation, experimental data, and theory.

2.4.2 helions

The quadrupole alignment scaling used for protons is extended to helions crossing the $|G\gamma|$=5 through $|G\gamma|$ =10 resonances. Fig 2.12 shows an example of a harmonic scan of helions at $|G\gamma| = 5$. This scan have corrector currents that follow [sin5v, cos5v]=[0.0 A, $\{-10 + 2\text{d}|\text{d} \in \{0, 1, 2, ..., 10\}\}$ A] and [sin5v, cos5v]=[$\{-10 + 2\text{d}|\text{d} \in \{0, 1, 2, ..., 10\}\}$ A, 0.0 A]. This causes a low amplitude response for the sin5v scan as cos5v=0.0 A is near full spin-flip. Additional harmonic scans for helions are found in App. B.1.3.

2.4.2.1 Imperfection Resonance Crossing in Close Proximity of Intrinsic Resonances

As observed in these two sets of resonance crossing, Fig. 2.13 and Fig. 2.14, the stable spin direction does not fully flip after crossing one and before crossing the other. Due to the proximity and strength of these nearby resonances, the stable spin direction is not fully aligned vertically between the two resonances. It is after crossing the pair of resonances that the stable spin direction returns to vertical and the spin-flip through each resonance can be observed with $P_f \sim 99\%$.

Results of 1,000 particles crossing the $|G\gamma| = 10$ and $|G\gamma| = 6 + \nu_y$ resonances with several machine configurations is shown in Fig. 2.15, which includes:

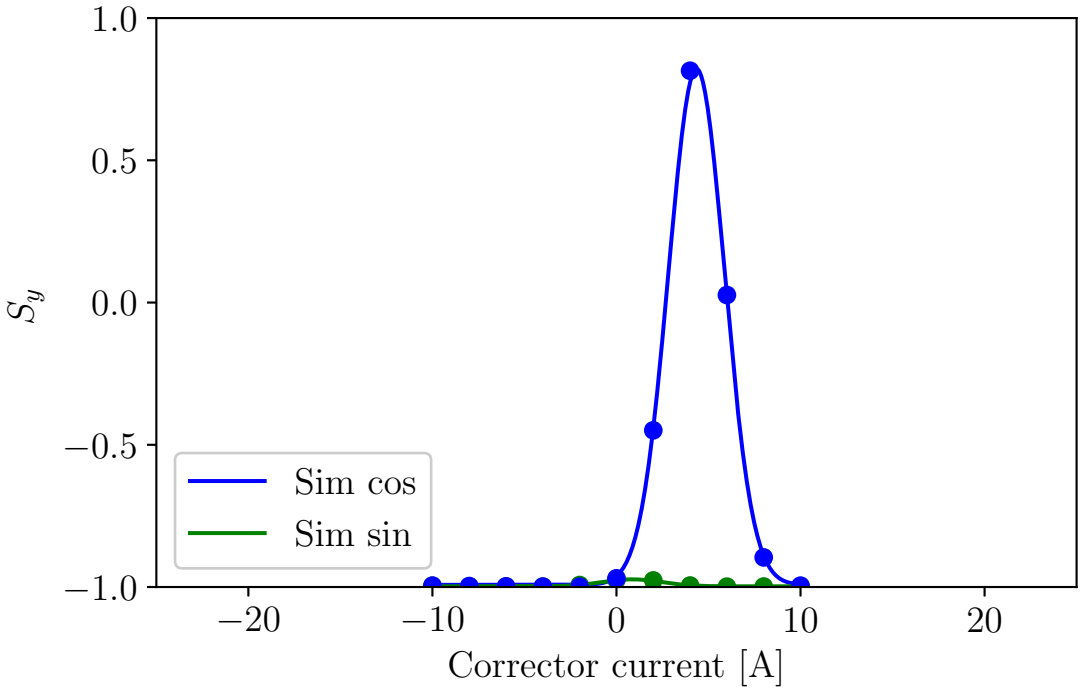

Figure 2.12: Imperfection resonance simulated scan of sine and cosine for helions at $|G\gamma| = 5$

- correction of h=10 orbit components so $|G\gamma| = 10$ does not spin-flip and $B_m l$ =35.0 G · m for the 100% spin-flip through the $|G\gamma| = 6 + \nu_y$ resonance
- sin10v, cos10v= 20 A, 11 A to spin-flip through the $|G\gamma| = 10$ resonance and $B_m l$ =35.0 G · m for the 100% spin-flip through the $|G\gamma| = 6 + \nu_y$ resonance
- sin10v, cos10v= 20 A, 11 A to spin-flip through $|G\gamma| = 10$ and $B_m l$ =0.0 G · m for to observe polarization loss through the $|G\gamma| = 6 + \nu_y$ resonance
- partial h=10 correction with sin10v, cos10v= 0 A, 5 A to observe polarization loss through $|G\gamma| = 10$ and $B_m l$ =35.0 G · m for to spin-flip through the $|G\gamma| = 6 + \nu_y$ resonance.

Note in the case that $B_m l$ =35.0 G · m that the vertical component of the polarization vector returns to vertical between the $|G\gamma| = 10$ and $|G\gamma| = 6 + \nu_y$ resonances. In the case where the $|G\gamma| = 10$ and $|G\gamma| = 6 + \nu_y$ resonances are enhanced to induce a spin-flip, the vertical component of the stable spin direction does not return to vertical between

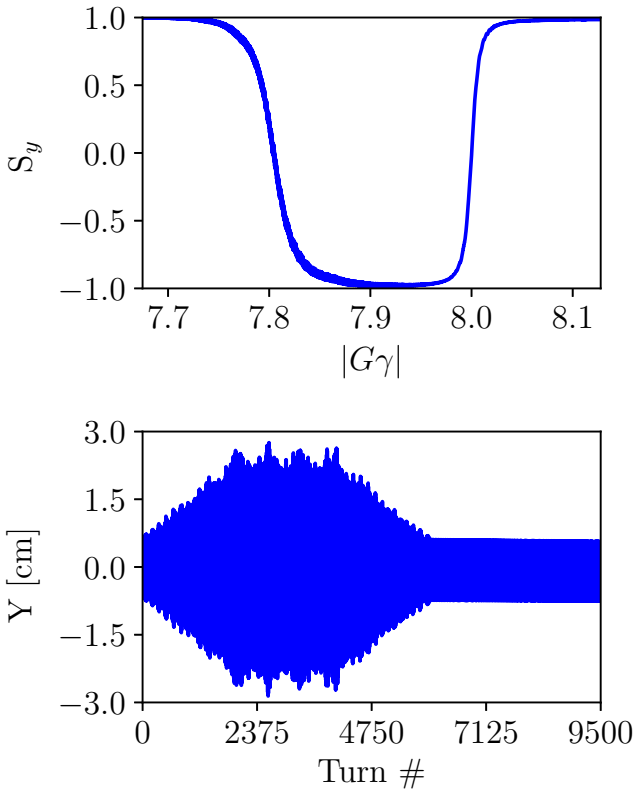

Figure 2.13: Helions crossing the $|G\gamma| = 12 - \nu_y$ resonance followed by the $|G\gamma| = 8$ resonance with harmonic corrector strengths [sin4v, cos4v, sin5v, cos5v, sin8v, cos8v]=[6.966, 1.666, 1.295, 10.700, 4.0, -13.0]. The AC dipole ramp is 2000 turns up, 2000 turns flat, and 2000 turns down. AC dipole parameters used are $B_m l = 23.8$ G·m and $\delta_m = 0.007$ with $P_f = 99.06$.

the two. The polarization after both resonances are crossed is where the efficiency of each spin-flip is accounted.

2.4.2.2 Imperfection Resonances Simulation Results

The data is fitted with a Gaussian of the form:

$$P_F(I_f) = A_{max,f} \exp\left(-\frac{I_f - \mu_f}{2\sigma^2} \right) + B_f \tag{2.4.2}$$

where f is the family being scanned (cos or sin), I_f is the corrector current of the family, μ_f and σ_f are the mean and variance of the distribution, $A_{max,f}$ and B_f are arbitrary scaling and offset, and P_F is used in place of P_f to avoid confusion with the family being scanned. These scans are done with two different orbits seen in Fig. 2.9 and Fig. B.6,

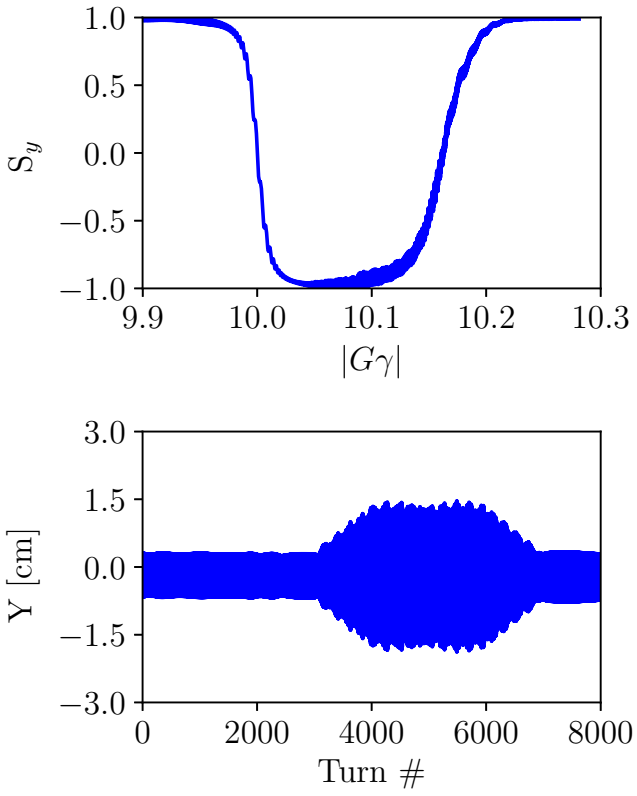

Figure 2.14: Simulation of 1,000 helion particles crossing the $|G\gamma| = 6 + \nu_y$ resonance preceded by the $|G\gamma| = 10$ resonance with harmonic corrector strengths [sin4v, cos4v, sin5v, cos5v, sin8v, cos8v]=[9.279, 2.220, 1.725, 14.253, 10.0, 10.0]. The AC dipole ramp is[N_{up}, N_{flat}, N_{down}]=[2000, 2000, 2000] turns. AC dipole parameters used are $B_m l = 14.1$ G·m and $\delta_m = 0.005$ with $P_f = 99.08$.

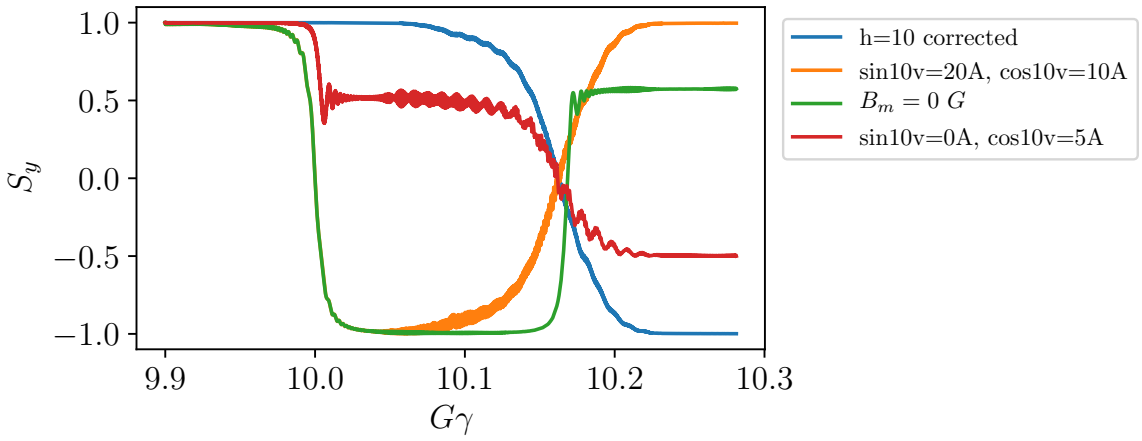

Figure 2.15: Results of 1,000 helion particles crossing the $|G\gamma| = 10$ and $|G\gamma| = 6 + \nu_y$ resonances for several machine configurations. Regions of interest being between the two resonances and the polarization downstream of both resonances.

where Fig. B.6 uses sin4v=2.097 $B\rho/B\rho(5)$ in place of sin4v=2.797 $B\rho/B\rho(5)$, to see how the μ_f and σ_f are affected. The Gaussian fit parameters are shown in Tab. 2.6. The μ and σ values are used to determine the corrector current shown in Tab. 2.7. One observes that the μ components are largely unchanged between the two orbits except the $|G\gamma| = 8$ and $|G\gamma| = 10$ which show a large dependence on the sin5v correction.

Table 2.6: Summary of Gaussian fit data for helion harmonic scans.

k	α	orbit	$\mu_{\sin}$ [A]	$\sigma_{\sin}$ [A]	$A_{max,\sin}$	$\mu_{\cos}$ [A]	$\sigma_{\cos}$ [A]	$A_{max,\cos}$
5	$\alpha_{helions,fast}$	Fig. 2.9	0.5200	1.5750	0.6843	4.2955	1.5288	0.8209
5	$\alpha_{helions,fast}$	Fig. B.6	0.4746	1.2075	-0.9671	4.2225	1.4749	0.8159
6	$\alpha_{helions,fast}$	Fig. 2.9	1.2226	3.6268	0.8773	-0.2896	2.7384	0.8127
6	$\alpha_{helions,fast}$	Fig. B.6	1.1615	3.6287	0.8823	-0.2372	2.7059	0.8205
7	$\alpha_{helions,fast}$	Fig. 2.9	3.1077	4.4358	0.8165	1.8801	4.5166	0.5680
7	$\alpha_{helions,fast}$	Fig. B.6	2.9817	4.5565	0.8073	1.6875	4.5153	0.5617
8	$\alpha_{helions,fast}$	Fig. 2.9	-4.8460	4.8366	-0.6658	10.6646	5.5313	0.3322
8	$\alpha_{helions,fast}$	Fig. B.6	1.9075	5.6127	0.8927	1.7186	5,3711	0.8653
9	$\alpha_{helions,fast}$	Fig. 2.9	-1.1232	5.2331	0.9987	-0.3165	3.9495	0.9779
9	$\alpha_{helions,fast}$	Fig. B.6	-1.0890	5.0791	0.9993	-0.3154	3.9433	0.9814
9	$\alpha_{helions,slow}$	Fig. B.6	-0.9737	4.7709	0.9550	-0.3320	2.989	0.6377
10	$\alpha_{helions,fast}$	Fig. 2.9	-23.6518	5.5783	0.9127	-0.4287	5.4708	0.5344
10	$\alpha_{helions,fast}$	Fig. B.6	-3.5187	5.4745	0.8869	1.2351	5.4345	0.5923
10	$\alpha_{helions,slow}$	Fig. B.6	-3.3476	3.0776	0.7155	0.7384	2.9718	-0.0992

The configuration of harmonic correctors in Tab. 2.7 can induce a full spin-flip (in the case of $G\gamma$=4 for protons and $|G\gamma|$=5, 6, 7, 8, 10 for helions) or fully correct the relevant harmonic to eliminate the resonance ($G\gamma$=3 for protons and $|G\gamma| = 9$ for helions.) The total corrector current for each of the resonances is shown in Tab. 2.7, none of which exceed $I_{max} = 25\ A$. There would also be more corrector current available if the h=4, 5 components were left uncorrected. Note that for crossing $|G\gamma|$=5, 6, 7, 8, and 10, the total corrector current is near the 25 A maximum and would not allow additional corrector current for other orbit corrections or manipulations.

2.5 AGS Dynamic Aperture at Injection

The goal for helions in the AGS at injection is to have both ν_x and ν_y inside the spin tune gap. For protons at $G\gamma$ =4.5 this has proven difficult due to excessive losses and constant

Table 2.7: Current to correct the two major orbit harmonics (h=4, 5), current to correct or amplify the orbit harmonic corresponding to the resonance (h=k), and the resulting maximum current on any single dipole corrector (current in units of A).

Species	k	sin4v[A]	cos4v[A]	sin5v[A]	cos5v[A]	sinkv[A]	coskv[A]	I_{max}[A]
Protons	3	-	-	-	-	0.897	-6.468	6.530
	4	-	-	-	-	0.0	18.0	24.306
Helions	5	2.797	0.669	-	-	10.0	-18.0	23.086
	6	4.393	1.051	0.817	6.748	-10.0	15.0	24.672
	7	5.733	1.371	1.067	8.806	-10.0	-10.0	24.246
	8	6.966	1.666	1.295	10.700	4.0	-13.0	24.491
	9	8.141	1.947	1.514	12.504	-1.074	0.0	17.924
	10	9.279	2.220	1.725	14.253	10.0	10.0	23.459

tuning. With helion injection at $|G\gamma| = 7.5$ being at a lower rigidity than protons at $|G\gamma| = 4.5$ ($B\rho = 7.203\ T \cdot m$) with $B\rho = 6.967\ T \cdot m$, concern over both the available aperture and dynamic aperture due to the strong optical distortions of the cold snake are raised. The physical aperture of the AGS is the beam pipe at the cold snake which is round with a 3.85 cm radius. As seen in Fig. 2.16, these optical distortions reduce quickly with $B\rho$.

To quantify this, particles are tracked through only the cold snake to calculate the transport matrix, Eq. 1.2.16. From the transport matrix, M, the total focusing and coupling is calculated from the focusing, FC, defined as [49],

$$FC = m_{12}^2 + m_{34}^2 \tag{2.5.1}$$

and the coupling, CP, is quantified using

$$CP = LL + UR \tag{2.5.2}$$

with

$$LL = m_{31}^2 + m_{32}^2 + m_{41}^2 + m_{42}^2 \tag{2.5.3}$$

$$UR = m_{13}^2 + m_{14}^2 + m_{23}^2 + m_{24}^2. \tag{2.5.4}$$

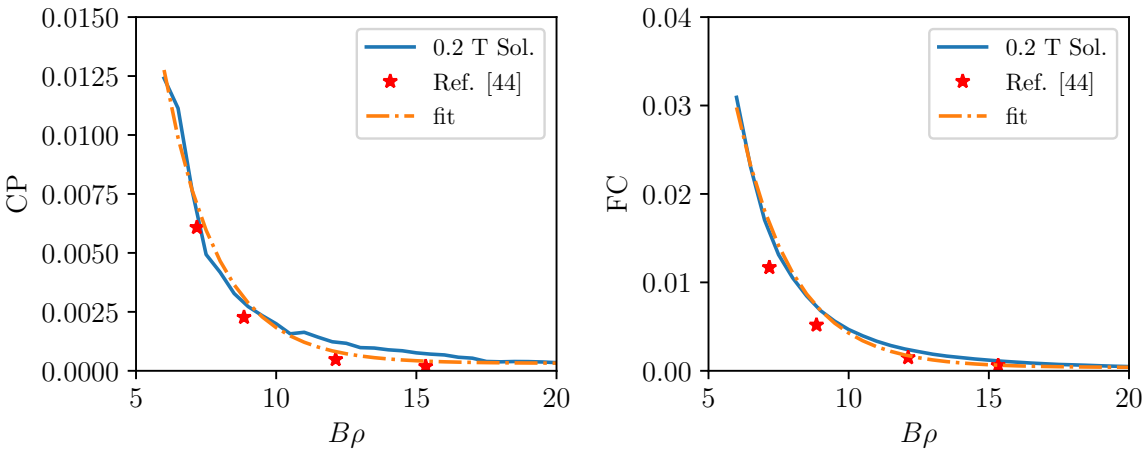

Figure 2.16: Coupling and focusing from the AGS cold snake as a function of $B\rho$ and comparison to an exponential function.

The cold partial snake magnet assembly also contains a solenoid magnet for coupling correction. The nominal current used is I_{sol}=220 A which corresponds to a field of B_{sol}=0.2 T. There is an engineering limit of $I_{sol,max}$=235 A, although this solenoid has been tested up to 300 A. From this, there are only marginal improvements that can be made on correcting the coupling so these simulations will use I_{sol} =220 A. An example of the coupling from a 0.5 T field is shown in Fig. 2.17, when one can see that the coupling at low energy is improved but is larger at higher energy.

The DA is calculated with various tune configurations to compare working points at injection. The methodology of the DA calculation follows:

1. Fit model to tunes

2. Find closed orbit

3. Find ±x limit where beam survives

    - Algorithm moves in steps of 0.5 mm from closed orbit until edge is found.
    - Binary search once edge is found.
    - Resolution of value ±0.008 mm.

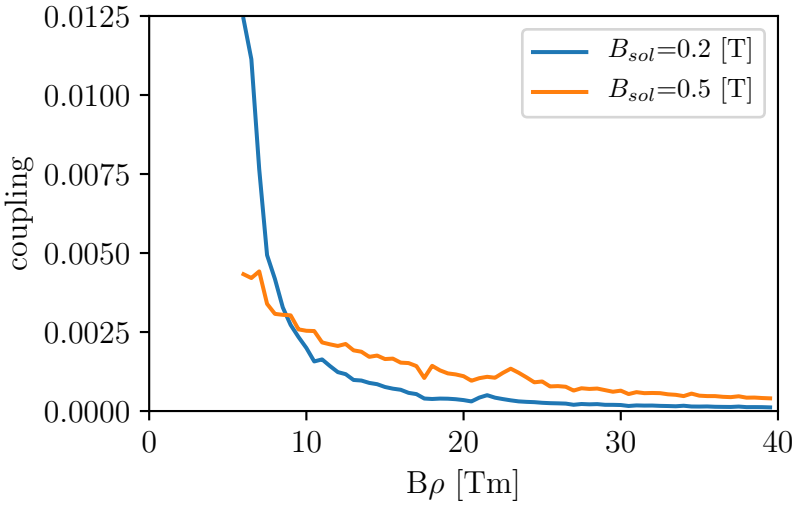

Figure 2.17: Figure showing the coupling error of the cold snake with a 0.2 T and a 0.5 T solenoid field with respect to $B\rho$.

4. Populate range $[X_L, X_U]$ with 20 particles separated by dx, and find Y_M (maximum stable Y) at each X coordinate.

    - Algorithm moves up in steps of 0.5 mm until edge is found.
    - Binomial search once edge is found.
    - Resolution of value ±0.008 mm.

5. Simulations with 169 points ($\nu_{\mathrm{x}} = \{0.69 + 0.02\mathrm{k} | \mathrm{k} \in \{1, 2, ..., 13\}\}$ and $\nu_{\mathrm{y}} = \{0.85 + 0.02\mathrm{k} | \mathrm{k} \in \{1, 2, ..., 13\}\}$)

This process is shown graphically in Fig. 2.18 and for one set of ν_x and ν_y in Fig. 1.8. This implementation uses a combination of Zgoubi and PyZgoubi where:

- Zgoubi handles all the tracking and optics computations,
- PyZgoubi handles particle coordinates and fitting algorithms described above,
- multi-threaded: PyZgoubi creates a thread for each ν_{y} and one ν_{x} configuration.

A comparison of the DA and the admittance is made for the AGS in the absence and presence of the snakes. This is shown for helions at $|G\gamma|$=7.5 in Fig. 2.19. Comparison of Fig. 2.19a with Fig. 2.19b shows that in the absence of the snakes, the DA is well

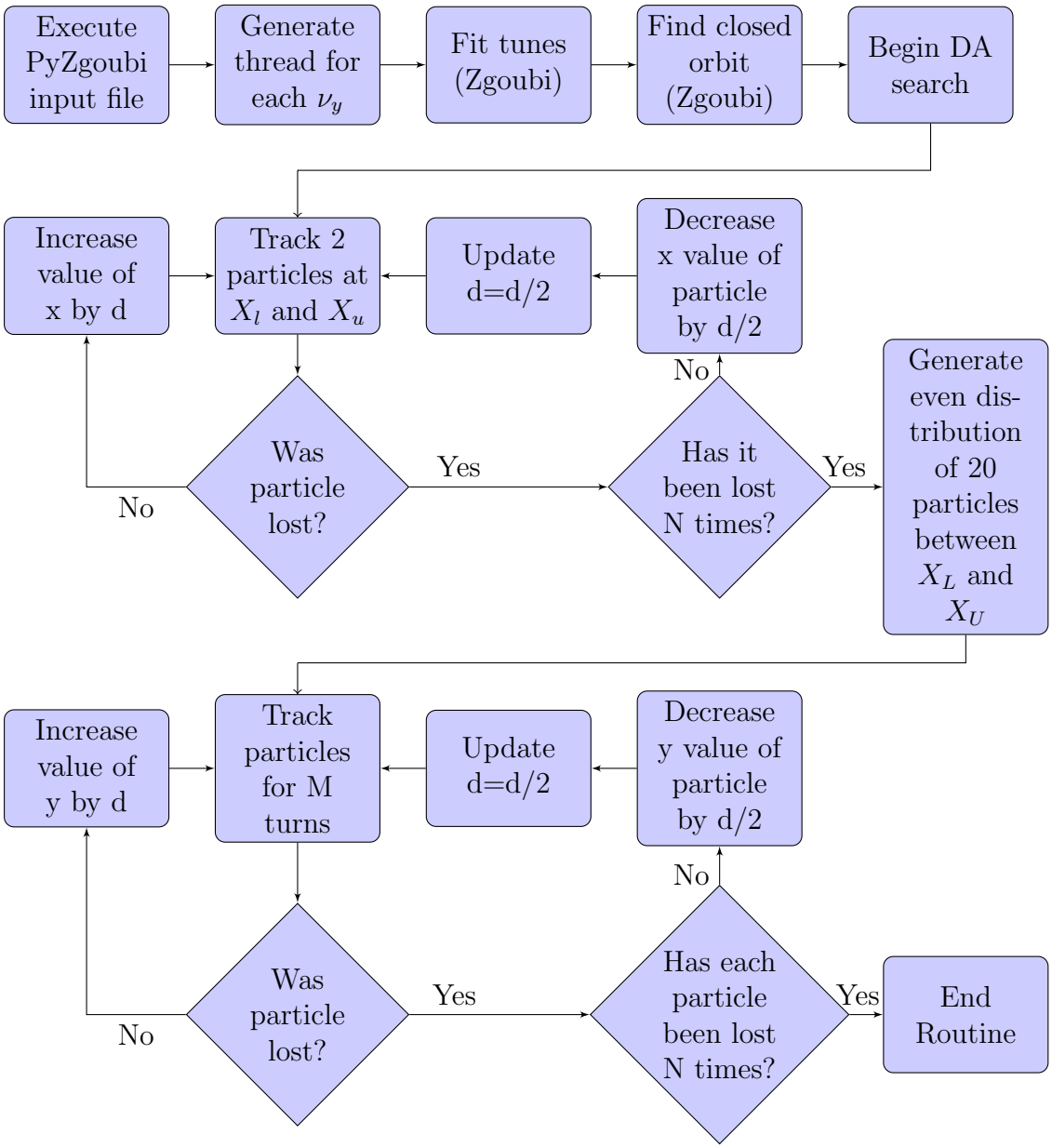

Figure 2.18: Flow chart showing the process for determining the DA.

larger than the admittance. Comparison of Fig. 2.19c with Fig. 2.19d shows that in the presence of snakes, the strong optical defects cause a further reduction in the DA and admittance.

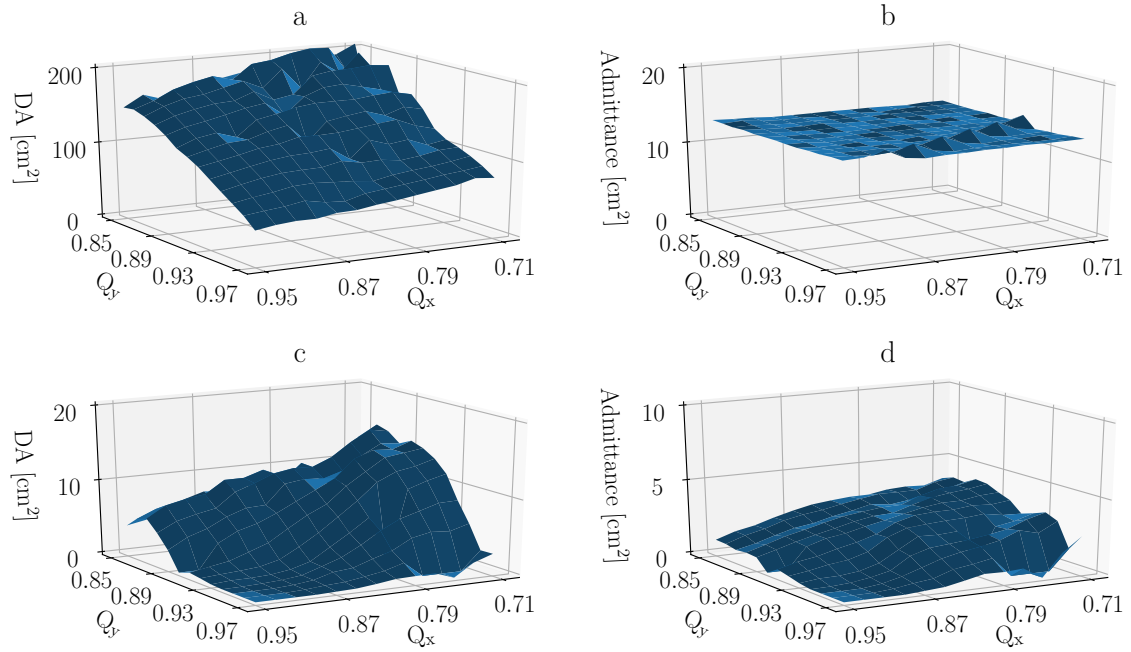

Figure 2.19: Comparison of DA and admittance for helions at $|G\gamma| = 7.5$ with: a) snakes off, no limiting aperture; b) snakes off with limiting aperture; c) snakes on, no limiting aperture; d) snakes on, with limiting aperture.

Simulations are performed for helions at $|G\gamma| = 7.5$ and $|G\gamma| = 10.5$, and $|G\gamma| = 4.5$ for protons and shown in Fig. 2.20. For each of these configurations, there are three cases simulated:

- From Fig. 2.20, one observes that there are subtle differences in the DA and admittance between helions at $|G\gamma| = 7.5$ and protons at $|G\gamma| = 4.5$ although a factor of 2 gain is observed when comparing to the $|G\gamma|$ =10.5 case (row (a) in Fig. 2.20).

- There is a factor of 4 reduction in the admittance compared to the DA. The DA in this case is larger than the available aperture. However, the configuration of tunes is greatly improved with the $|G\gamma|$ =10.5 case (row (b) in Fig. 2.20 for 200 turns).

- When tracking for 1,000 turns, there is a further reduction in the admittance with $|G\gamma|$=10.5 still displaying the largest value (row (c) in Fig. 2.20 for 1,000 turns).

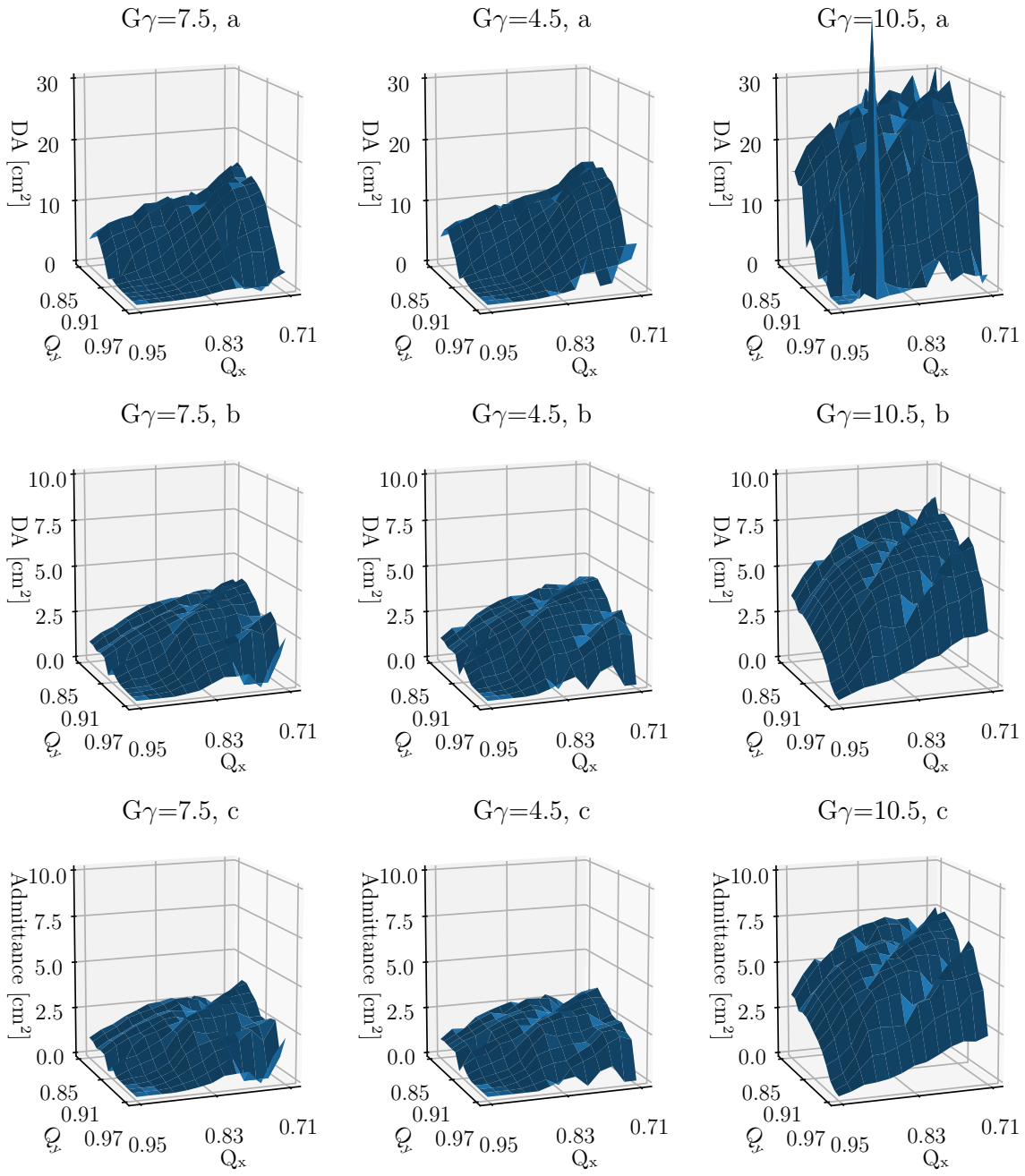

Figure 2.20: DA and admittance of AGS sorted by rigidity at $|G\gamma| = 7.5$, $B\rho = 6.968\ T{\cdot}m$, $|G\gamma| = 4.5$, $B\rho = 7.203\ T{\cdot}m$, and $|G\gamma| = 10.5$, $B\rho = 10.780\ T{\cdot}m$ where a) shows the DA without the limiting aperture of the snakes, b) shows the admittance and N_{turns}=200, c) shows the admittance and N_{turns}=1000.

Ideally this tracking would be for a number of turns equal to the time the particles are at injection energy. Computationally this proves problematic since the time for simulations is linearly proportional to the number of turns. The AGS f_{rev}=341 kHz at injection for protons, which are accelerated almost immediately after being injected. For protons

1,000 turns is more than sufficient. For polarized helions, there is the possibility that there are multiple injections to reach the desired intensity. With a Booster cycle length of 200 ms, the requirement for helions would be 70,000 turns. This is not necessary as the simulations show the admittance is many times larger at $|G\gamma| = 10.5$ than $|G\gamma| = 7.5$.

Note that there is virtually zero DA available in the region of interest with $[\nu_x,\nu_y] \geq [8.9, 8.9]$ for helions at $|G\gamma| = 7.5$ and protons at $|G\gamma| = 4.5$. This further supports extraction of helions at $|G\gamma|=10.5$ as the available DA is substantial. This is also observed in Fig. 2.21 where the three configurations are compared at a fixed tune of $[Q_x,\ Q_y]=[0.75, 0.91]$.

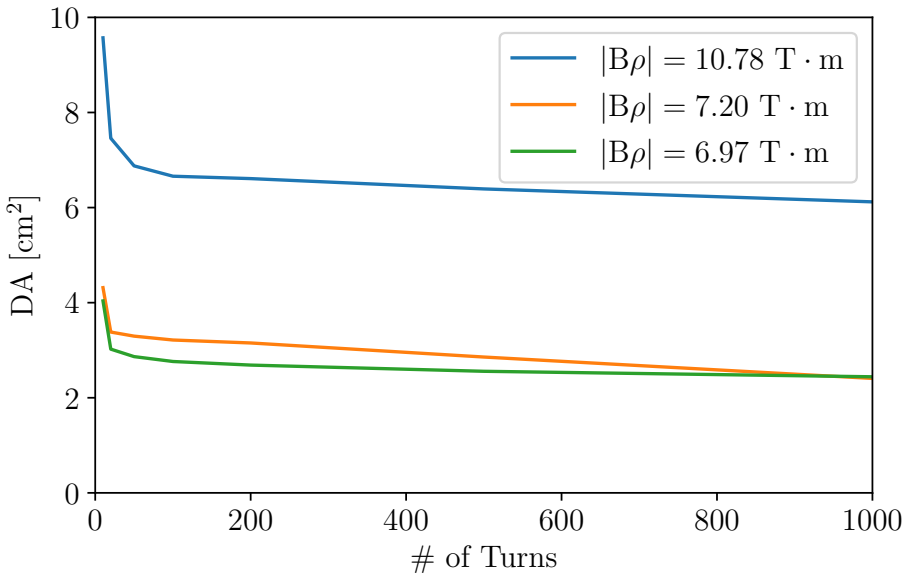

Figure 2.21: Comparison of admittances for the three configurations at $[Q_x,\ Q_y]=[0.75, 0.91]$ and an increasing number of turns.

Chapter 3

Experimental Setup

3.1 Booster Main Magnet

The Booster Main Magnet Power Supply (BMMPS) is comprised of six modules. Each module provides 1,000 V, however four have a maximum current of 3,000 A whereas the remaining two have a maximum current of 5,000 A. The power supply is controlled through the BoosterMainMagnet application, shown in Fig. 3.1. A typical main magnet function has extraction occurring at the peak current. The function used for the experiment has extraction occur at peak $\dot{B} = dB/dt$ so protons could continue to circulate in Booster with extraction turned off. This setup of allowing particles to circulate with extraction turned off facilitated studies prior to the ability to extract into AGS. The tunes and chromaticities are adjusted with the application OpticsControl. The maximum current on each trim tune supply is ±1100 A, and on each sextupole supply is ±250 A. For this setup at the timing of the $|G\gamma| = 0 + \nu_y$ resonance, the trim quadrupole supply currents are I_{Q_x} =309.7 A, I_{Q_y} =-504.2 A, and sextupole currents of I_{C_x} =6.7 A, I_{C_y} =69.4 A.

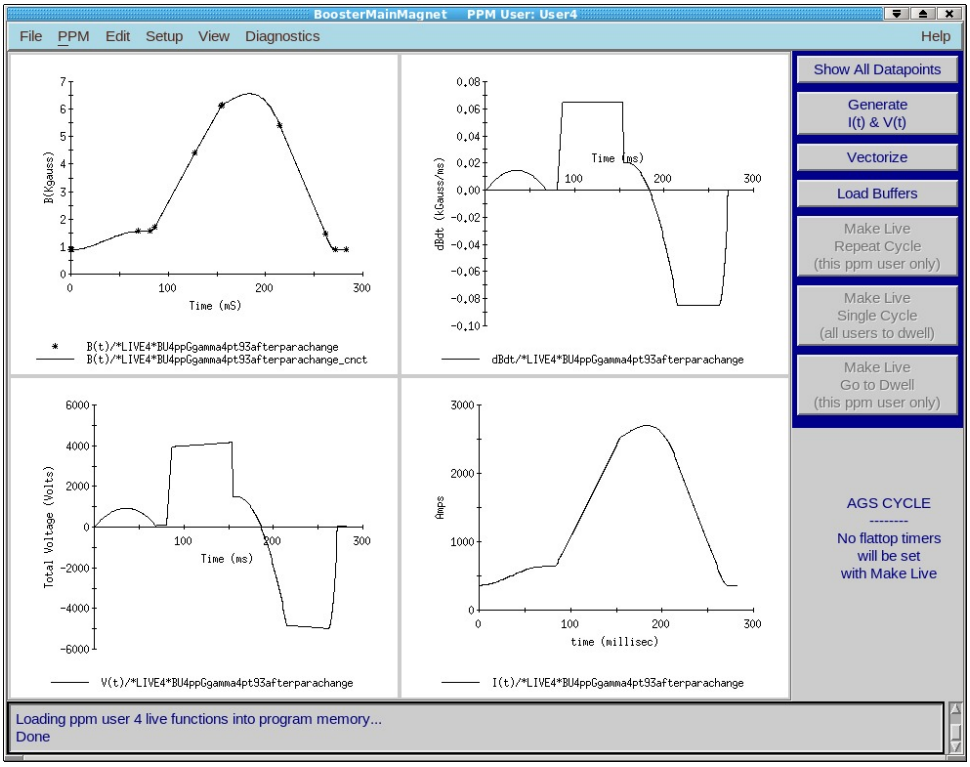

Figure 3.1: Booster main magnet application with the function used for the AC dipole experiment loaded.

3.2 AC Dipole Design

From the above sections describing polarized protons and helions crossing intrinsic resonances, Sec. 2.3, the maximum required field for achieving a full spin flip was 20.5 G · m for helions crossing the $G\gamma = 6 + \nu_y$ resonance. A design strength of 25 G · m provides an approximate margin of 25% in requirement of the AC dipole strength.

The Booster AC dipole upgrade installation, Fig. 3.2, replaced the tune kicker magnets in the E3 section (see Fig. 1.2). There are two newly installed magnets that will operate as tune meter kickers. A high voltage relay is connected to the vertical magnet assembly to allow the vertical magnet to also operate as an AC dipole.

The vertical magnet is a window frame magnet made of high permeability ferrite blocks 2.54 cm thick, 50 cm long with horizontal and vertical openings of 8.6 cm×8.2 cm. The vertical opening is reduced because of a 2 mm copper conductor on the top and bottom of the 8.6 cm iron opening. This aperture was determined in Sec. 3.2.1 For design frequency of f_m=250 kHz and a measured inductance of L=1.06 μH, the required

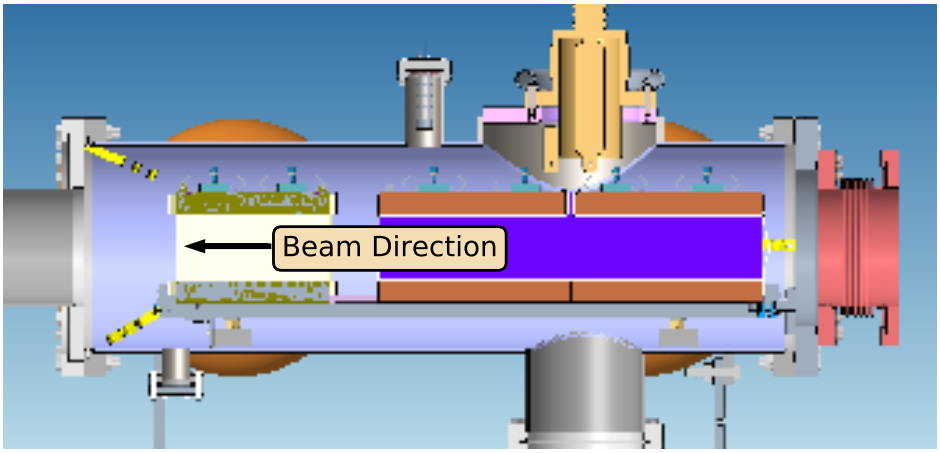

Figure 3.2: Cross section of the AC dipole upgrade vacuum assembly, where the longer magnet on the right operates as the AC dipole.

capacitance from Eq. 1.2.58 is C=0.382 μF.

When the magnet is operating as a tune kicker, the larger magnets (20 cm and 50 cm horizontal and vertical lengths compared to the old 12 cm magnets) for the horizontal and vertical tune kickers will allow measurements at the maximum Booster energy. The old tune kickers lacked sufficient magnetic strength to provide measurements above 9.3 T $\cdot$ m, whereas the maximum energy of the Booster corresponds to 17.24 T $\cdot$ m, see App. A.1.

3.2.1 Determining Magnet Aperture

As discussed in Sec. 1.3.5, the AC dipole forces the entire bunch to undergo large amplitude vertical betatron oscillations. When designing the magnet, not only must there be sufficient aperture to accommodate these oscillations but one also has to ensure this does not become the limiting aperture of the machine.

To confirm the limiting aperture of the machine, a beam study was performed using Au beam by Keith Zeno on June 16, 2017. From their study: A vertical bump was made

25 ms ($\beta\gamma = 0.0742$) into the cycle at the B7 location at +13.5 mm and -12.5 mm, just large enough to generate a small loss. The measurement had to be performed early in the cycle because the correctors used are not strong enough to generate a loss at higher $B\rho$. To determine the size of the beam, a measurement of the vertical profile of the beam was taken at MW006 (a multi-wire positioned six feet into the BtA (Booster to AGS) transfer line). This normalized RMS emittance was found to be $\varepsilon_{y,N,rms} = 3.7\ \pi$ mm mrad for the corresponding $\beta\gamma = 0.4948$. This value was compared to the point of the measurement with Eq. 1.2.25 to find the unnormalized emittance of $\varepsilon_{y,rms,25\ ms} = 49.3\ \pi$ mm mrad.

The values from their measurements were used in the MADx Booster Model with the bump and the known aperture of B7 confirmed the aperture to be 3.5 cm as seen in Fig. 3.3 [50].

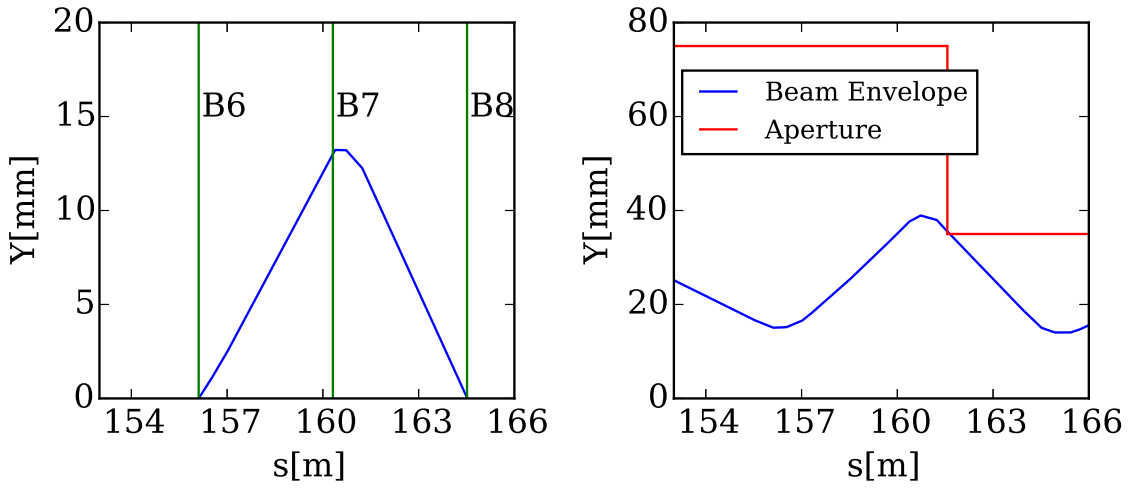

Figure 3.3: (Left) Vertical orbit bump that generated the loss at B7. (Right) The full width of the beam with the addition of the orbit bump and the known aperture.

Survey data shows a maximum difference in vertical alignments of 3 mm and horizontal alignments of 10 mm as seen in Fig. 2.9 [51]. In the space available at E3 for installation, the maximum beam envelopes are 64.25 mm vertically and 64.1 mm horizontally. These values were used to determine the minimum magnet aperture for the AC dipole, in order to avoid becoming the limiting aperture of the machine.

These parameters were specified for the mechanical design which was carried out by

Joseph Tuozollo and Danny Puleo. The excitation of this magnet with an AC driving current was modelled by Nicholaos Tsoupas [52] and Peter Oddo.

3.2.2 AC Dipole Installation

After successful design of the magnet, it was manufactured and assembled (as seen in Fig. 3.4 prior to installation into vacuum chamber). The installation occurred during the period of December 2018 through January 2019, and is seen in Fig. 3.5 as the vacuum chamber was being prepared for a vacuum bake out. This installation involved many personnel across several specialist groups. The high power feed-throughs were installed during the summer shutdown of 2019.

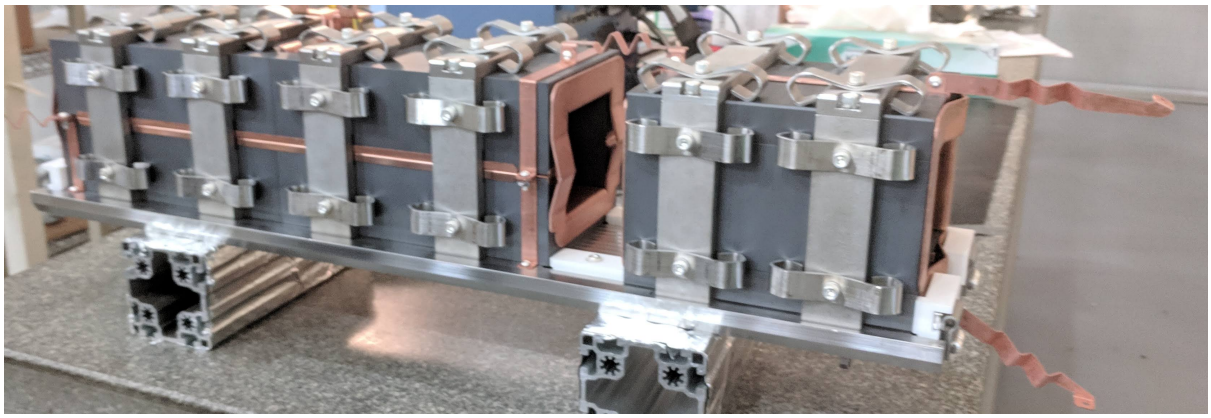

Figure 3.4: Magnet assembled prior to insertion into vacuum chamber and installation in ring.

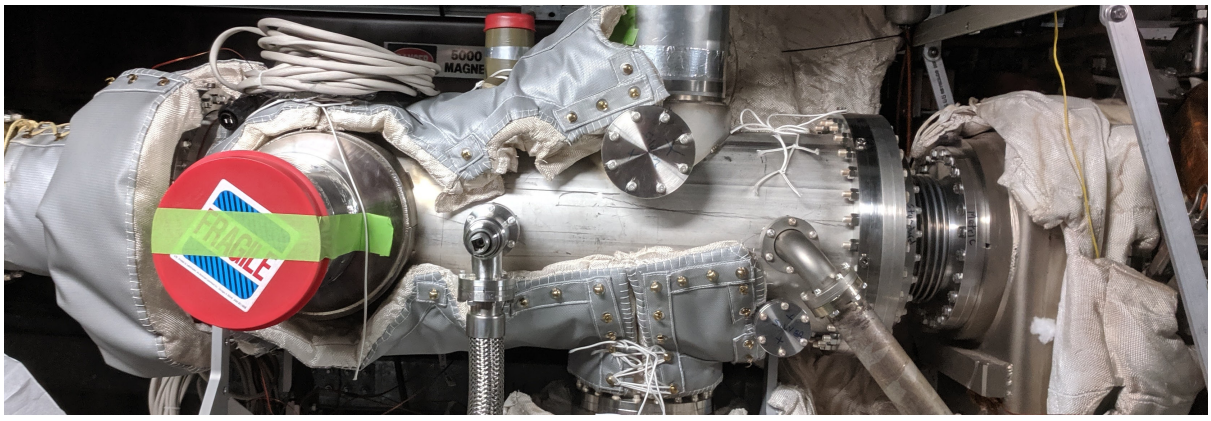

Figure 3.5: Magnet vacuum chamber after installation in ring as it is being prepared for a vacuum bakeout.

At that time, the new tune meter was commissioned along with the new BPM man-

ager, discussed in App. A.1. The BPM manager, and hardware upgrades to the BPM systems, was made by Matthew Panniccia and commissioned with the assistance of Kiel Hock. The power amplifier for the AC dipole was installed during the fall of 2020 to allow for the study in early January, 2021. The power amplifier and circuit were designed by Peter Oddo.

3.3 Controlling $\Delta\nu_y$

3.3.1 Chromaticity Control

Due to the vertical coherent amplitude's dependence on the vertical betatron tune, it is important to adjust the chromaticity to control the vertical betatron tune spread. Minimizing the vertical chromaticity in turn minimizes the spread of ν_y which reduces the variation of δ_m in Eq. 1.2.61 which serves two purposes:

- the AC dipole strength requirement for achieving a full spin-flip is less due to the smaller spread in Y_{coh},
- the maximum Y_{coh} of a particle is controlled to prevent particles being lost on the limiting aperture.

The full-width at half-maximum of the relative momentum spread for protons near extraction was measured to be 1.39×10^{-3} during RHIC run17. For a longitudinal Gaussian beam distribution this corresponds to $\sigma_p = 1.18 \times 10^{-3}$. The natural vertical chromaticity for the proton setup is $\xi_{y,nat} = -2.64$, the amplitude of which for protons crossing the $G\gamma = 0 + \nu_y$ resonance is shown in Fig. 3.6 with a comparison with $\xi_y = -0.5$. Since there is a minimum coherent amplitude to achieve a spin flip, the AC dipole operating at the natural chromaticity will need a stronger kick than with the chromaticity near zero. The observation that protons would be lost while operating at the natural chromaticity is clear with $Y_{coh,max} = 8$ cm and a limiting aperture of 3.5 cm. The AC dipole field strength required to 99% spin-flip and the corresponding maximum vertical amplitude

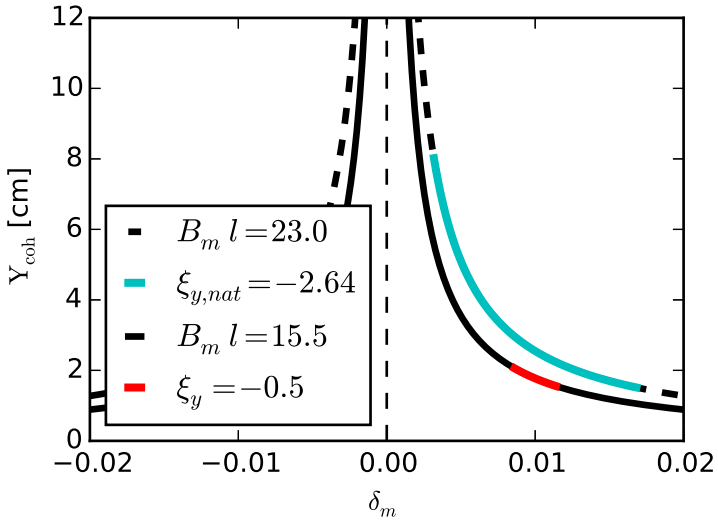

Figure 3.6: Y_{coh} at ξ_y=-0.5, -2.64 and corresponding $B_m l$ for a 99% spin-flip.

for protons crossing the $G\gamma = 0+\nu_y$ resonance at several values of ξ_y is shown in Tab. 3.1.

Table 3.1: Comparison of AC dipole strength for 99% spin-flip and corresponding maximum Y_{coh} at several vertical chromaticity settings.

ξ_y	-0.50	-1.00	-1.50	-2.64
$B_m \cdot l$ $[G \cdot m]$	15.5	18.0	19.6	23.0
$Y_{coh,max}$ $[cm]$	2.38	2.99	3.58	7.91

It was observed when running the AC dipole in the AGS that amplitude detuning reduced the ability to spin-flip and it was decided to run with the bare machine, i.e. no sextupole current. The AGS has $\xi_{y,nat}$ ~0 so the need to control the chromaticity was not as necessary as with the Booster. To check the amplitude detuning in the Booster when running the AC dipole with sextupoles on, simulations were performed.

3.3.2 Bunch Length Control

From Sec. 3.3.1, controlling the ξ_y is imperative to minimize $\Delta\nu_y$ while operating the AC dipole. From Sec. 1.2.2, introducing a second RF harmonic, with the correct phase and amplitude, will lengthen the bunch and reduce δp of the bunch. The parameters from the previous section are used and simulated with the AC dipole. This shows that the dual RF harmonics further reduces AC dipole requirements for a full spin-flip.

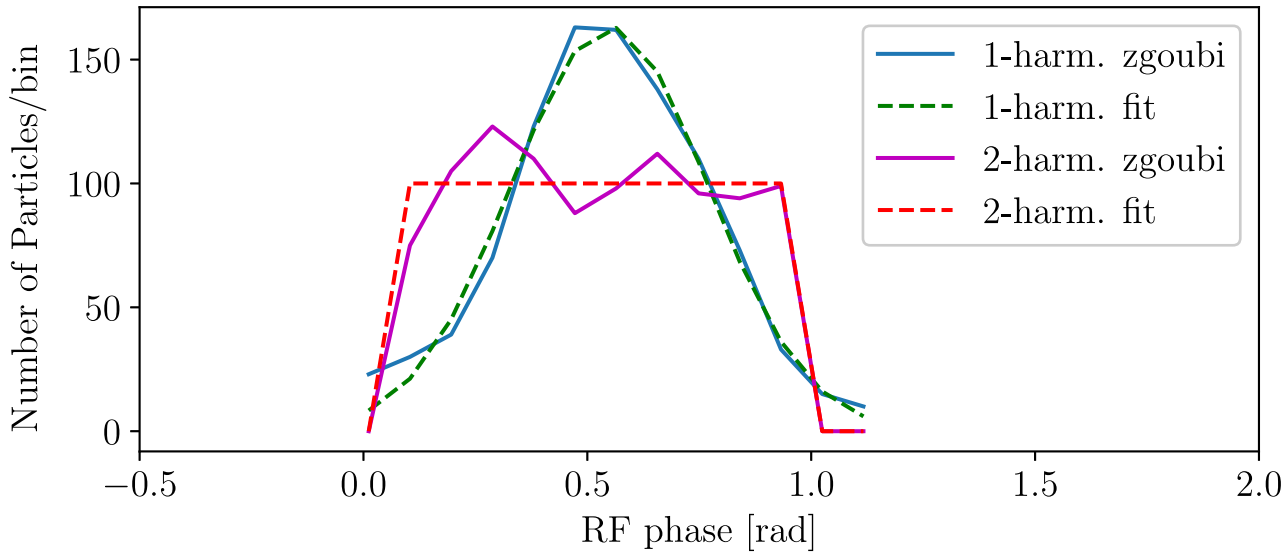

Figure 3.7: Longitudinal distribution from a single and dual harmonic RF system.

Table 3.2: AC dipole requirements for a full spin-flip for the single and dual RF harmonic cases.

	$h_{rf,1}$=1	$h_{rf,1}$=1, $h_{rf,2}$=2
$B_m l$ [G · m]	15.5	13.9
$Y_{coh,max}$ [cm]	2.4	2.1

3.4 Variable ν_m

By Eq. 1.2.57, ν_m is not fixed as particles are accelerated and f_{rev} increases. Protons crossing the $|G\gamma| = 0+\nu_y$ has a f_{rev} range from 1.373 MHz to 1.386 MHz during an 8,000 turn AC dipole pulse. This frequency change has a corresponding change of $\Delta\nu_m$=0.00155. An example of this is shown in Fig. 3.8 where the increasing frequency causes a sweep of ν_m. Due to the lower γ of helions crossing $|G\gamma| = 12 - \nu_y$, there will be an even larger sweep of $\Delta\nu_m$=0.00239. A slope can be put on the tunes to mitigate this effect.

3.5 Orbit Control

The orbit of the Booster is controlled via the boosterOrbitControl application, Fig. 3.9, which shows the pane for harmonic orbit corrections. This application controls the 24 horizontal and 24 vertical corrector magnets primarily through closed orbit bumps and

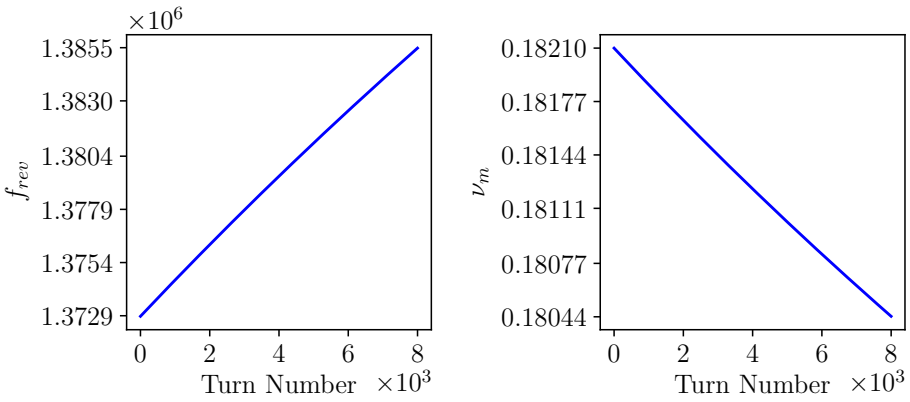

Figure 3.8: Booster f_{rev} for protons crossing the $|G\gamma| = 0 + \nu_y$ resonance and corresponding change in ν_m as a result.

harmonic bumps. For harmonic corrections, each supply has a gain calculated by their phase and the corresponding harmonic number.

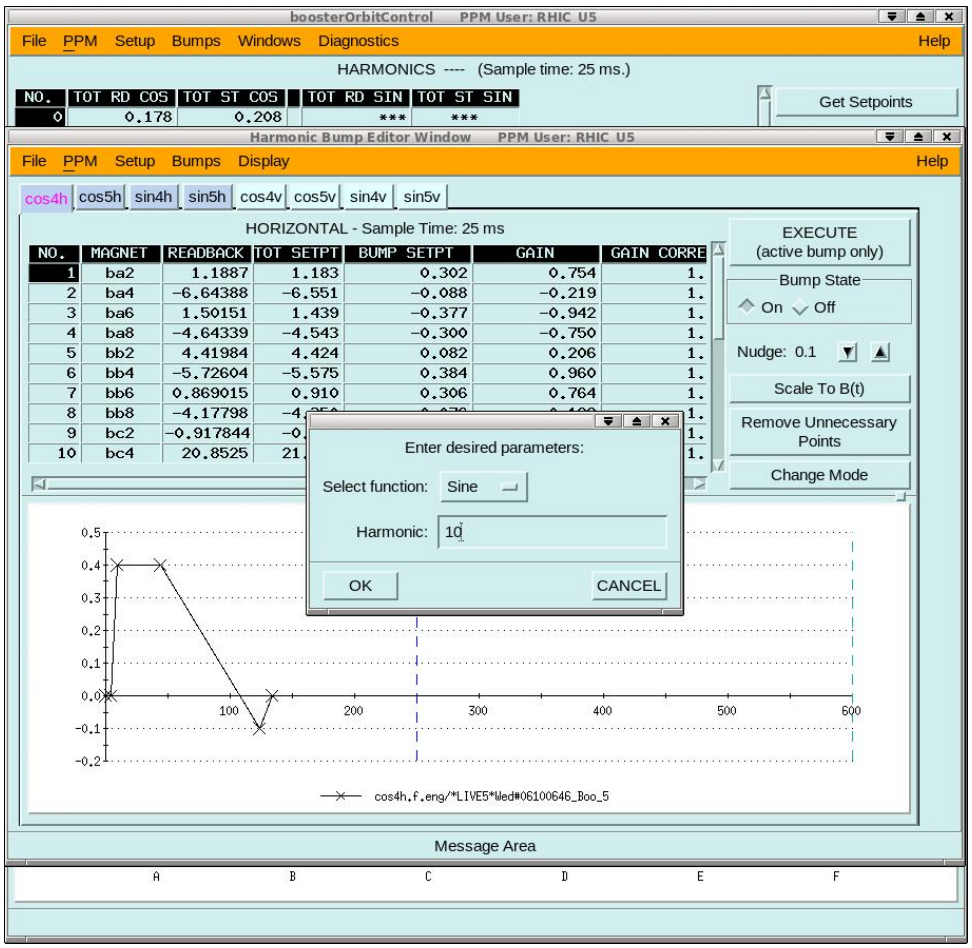

Figure 3.9: boosterOrbitControl application used to manipulate the orbit in Booster through their 48 horizontal and vertical orbit correctors.

3.6 AC Dipole Controls

To control the AC dipole, an ADO (Accelerator Device Object) manager was made for changing of the parameters. These ADO parameters are also integrated into the top pane of the Booster AC dipole application, Fig. 3.10. The AC dipole application also includes three panes: an FFT of the beam position monitor (BPM) data (top), the BPM position (middle), and the AC dipole current (bottom). This also shows an AC dipole pulse of

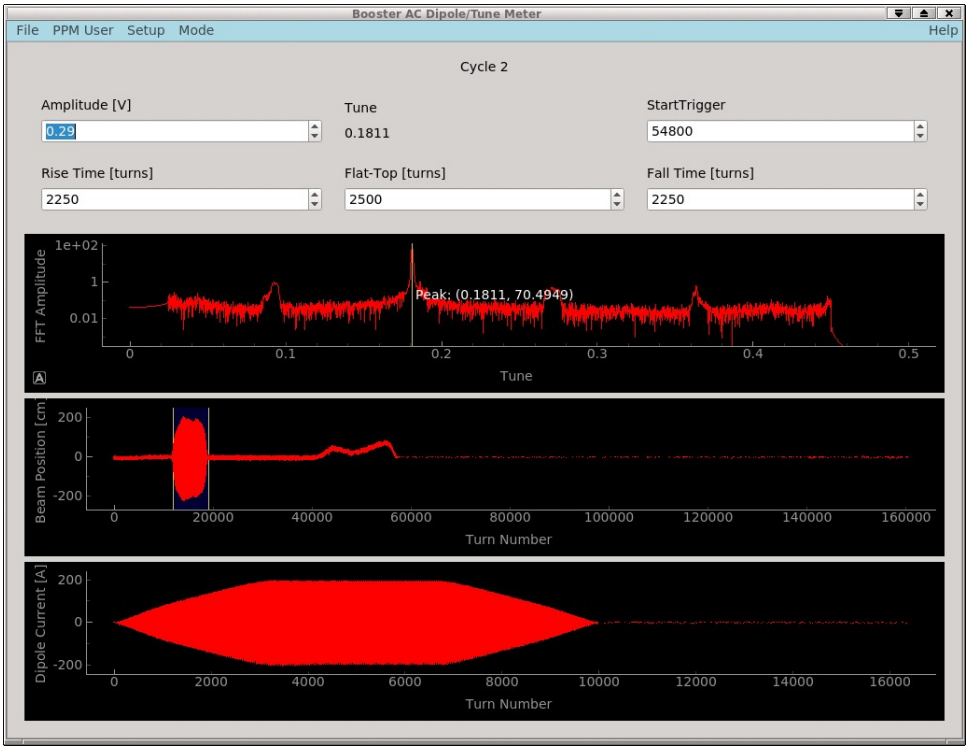

Figure 3.10: The Booster AC dipole application with ADO controls on top and 3 graphics panes of: FFT of vertical BPM data (top); vertical BPM data (middle); AC dipole current (bottom).

2250 turns up, 2500 turns at maximum amplitude, 2250 turns down. As the setpoint of the power amplifier is in units of voltage, the correlation between setpoint and output current is shown in Fig. 3.11.

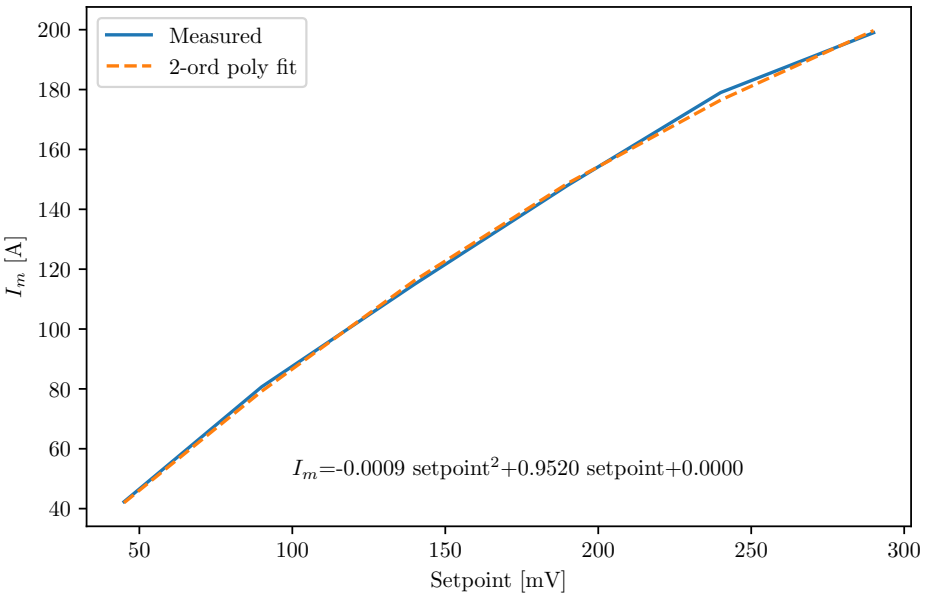

Figure 3.11: Magnet current as a function of setpoint.

Chapter 4

Experimental Results

4.1 Beam Dynamics with an AC dipole

Prior to having polarized protons cross the $G\gamma = 0 + \nu_y$ resonance, beam dynamics effects of the AC dipole are studied. Sec. 4.1.1, 4.1.2, and 4.1.3 are results from studies outside the block of time devoted to transmission of polarization through the $|G\gamma| = 0 + \nu_y$ resonance. The beam for the studies was prepared primarily by Keith Zeno with measurements taken by Kiel Hock. The experimental period for polarization transmission studies was scheduled for 3 days in January 2021. This experimental period was carried out with three shifts per day with Haixin Huang, François Méot, Vincent Schoefer, and Kiel Hock participating.

4.1.1 Chromaticity Control

For calculating the tunes, both an FFT and a damped sinusoid fit are used. The function for the damped sine fit is [53],

$$Y = e^{-\tau} \sin(2\pi\nu_y(T - T_o) + \phi) + C. \tag{4.1.1}$$

where τ is the damping time, T is the turn number and T_o is the initial turn, ϕ and C are a phase and constant offset. Fig. 4.1 shows a tune measurement by sine fit for two different chromaticity values. The damped sine fit procedure is also programmed to do

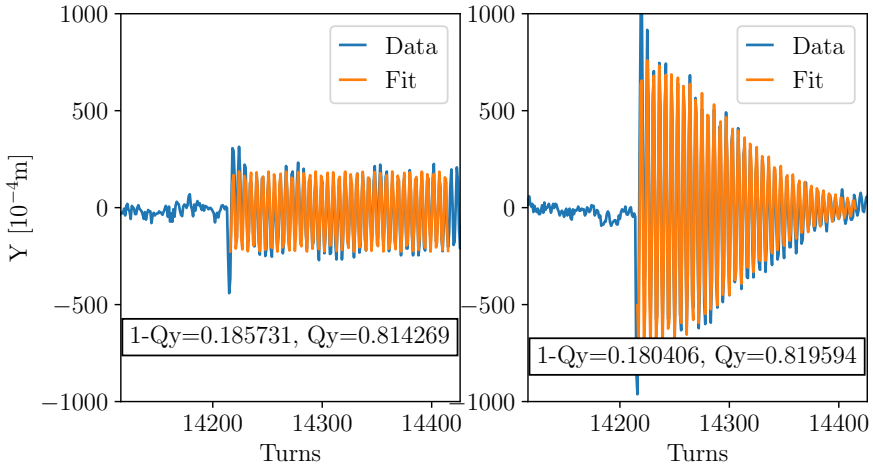

Figure 4.1: Damped sinusoid fit, Eq. 4.1.1, with BPM data for tune measurement. (left) ξ_y=-0.2 and (right) $\xi_y = \xi_{y,nat}$

a sine fit for N turns every M turns through the data set. The chromaticity is measured using the formula [54]

$$\xi_y = \frac{1}{\gamma_T^2} \frac{\Delta\nu_y}{\nu_y} \frac{r}{\Delta r} \tag{4.1.2}$$

where r is the Booster radius, $\Delta\nu_y$ is the change in ν_y for corresponding radius change Δr. Reducing ξ_y to zero diminishes the required $B_m l$ to full spin-flip while also reducing the number of particles that may be lost on the limiting aperture, as discussed in Sec. 3.3.1. This is also observed in Fig. 4.2 where a scan of δ_m is performed with $B_m l = 3.3$ G $\cdot$ m ($Y_{coh} = 0.39$ cm at δ_m=0.01), setting ξ_y=-0.2 provides 0% beam loss up to $\delta_m = \pm 0.0025$ compared to $\delta_m = \pm 0.009$ with $\xi_{y,nat}$.

The extended sine fit is run to fit for 200 turns every 200 turns through the duration of the oscillations. This provides Q_y throughout the AC dipole pulse for various δ_m values, in the absence of extraction bumps, as shown in Fig. 4.3.

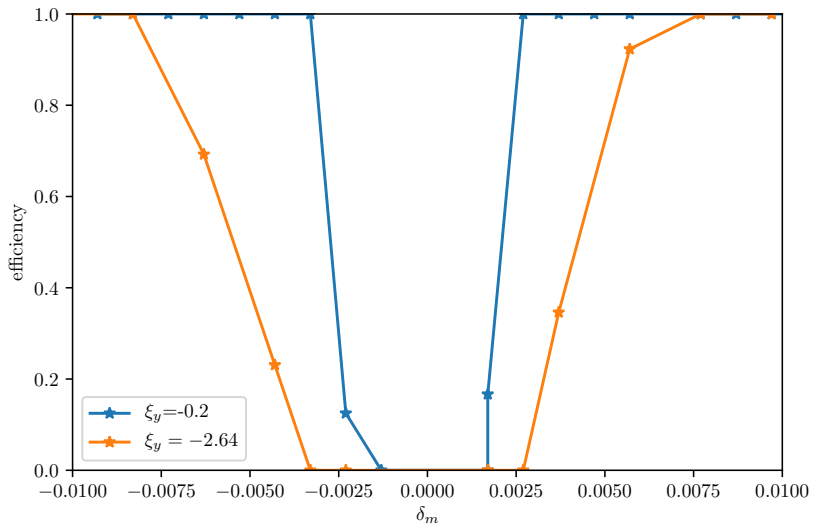

Figure 4.2: Losses generated from AC dipole pulse (efficiency) at corresponding δ_m values and $B_m l = 3.3$ G · m.

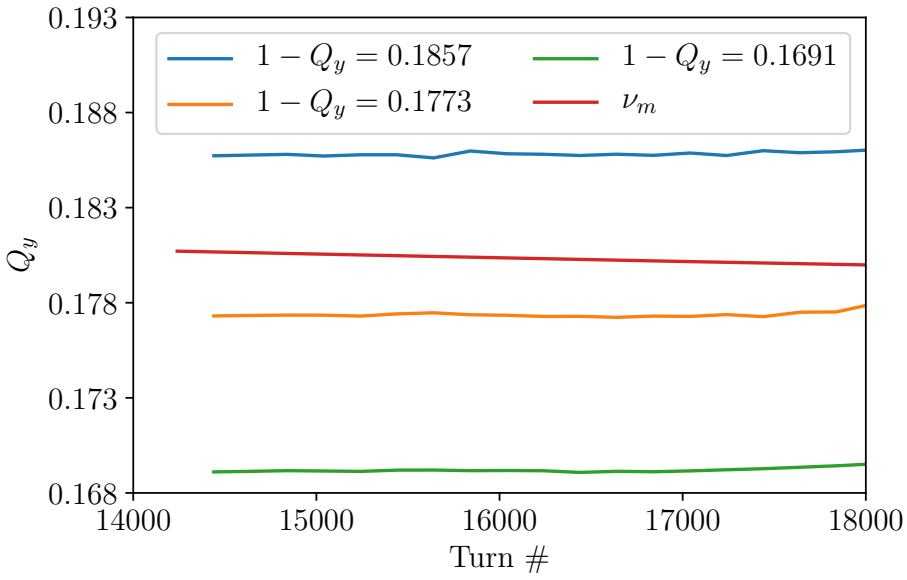

Figure 4.3: Q_y through the AC dipole pulse for δ_m=0.008 (blue), -0.003 (orange), and -0.012 (green) with a comparison of ν_m.

4.1.2 Scanning δ_m

With each polarization measurement taking many AGS cycles to accumulate 10 million events, the average Y_{coh} at the center of the pulse is used from each cycle to determine the amplitude. The measured Y_{coh} for each AC dipole pulse at $B_m l = 6.6$ G · m is shown in Fig. 4.4

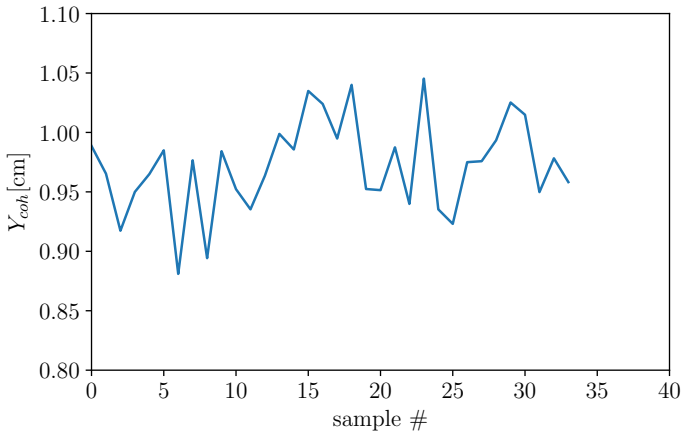

Figure 4.4: Example of measured Y_{coh} for each AC dipole pulse at $B_m l = 6.6$ G · m.

A scan of δ_m was done by adjusting ν_y and shows strong agreement between theory, measurements, and simulations. This study was performed with $B_m l = 2$ G · m so as to be constant over the range of δ_m and not generate loss with small δ_m.

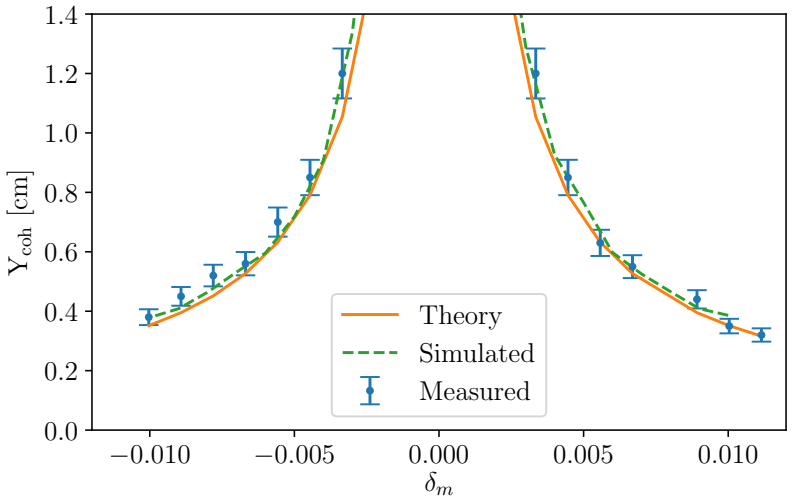

Figure 4.5: Y_{coh} at corresponding δ_m values with $B_m l = 2$ G · m.

4.1.3 Scanning $B_m l$

The strength of the AC dipole was increased in increments of 50 mV and the resulting Y_{coh} was measured and is shown in Fig. 4.6. This plot shows there is strong agreement between theory, measurements, and simulations at all strengths of the AC dipole that are presented.

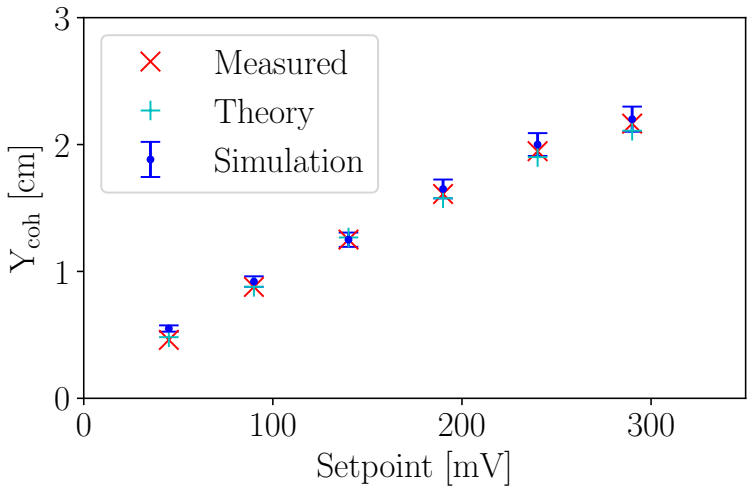

Figure 4.6: Y_{coh} at corresponding $B_m l$ values in units of setpoint (mV).

4.1.4 Emittance Growth

Scraping was setup after the AC dipole pulse so any emittance growth would show increased losses. In the Booster, scraping is done with a bump on the limiting aperture as there are no collimators. This is shown in Fig. 4.7 with three traces corresponding to: AC dipole off (blue), AC dipole on (red), AC dipole on with Q_x lowered 0.02 (yellow). Comparison of AC dipole on with AC dipole off after the tune adjustment shows no increase in losses and thus the absolute size of the beam is unchanged. During the experiment, profiles are taken on MW006 (Fig. 4.8) to monitor for emittance growth. During the experimental period emittance growth on MW006 did not exceed 3%.

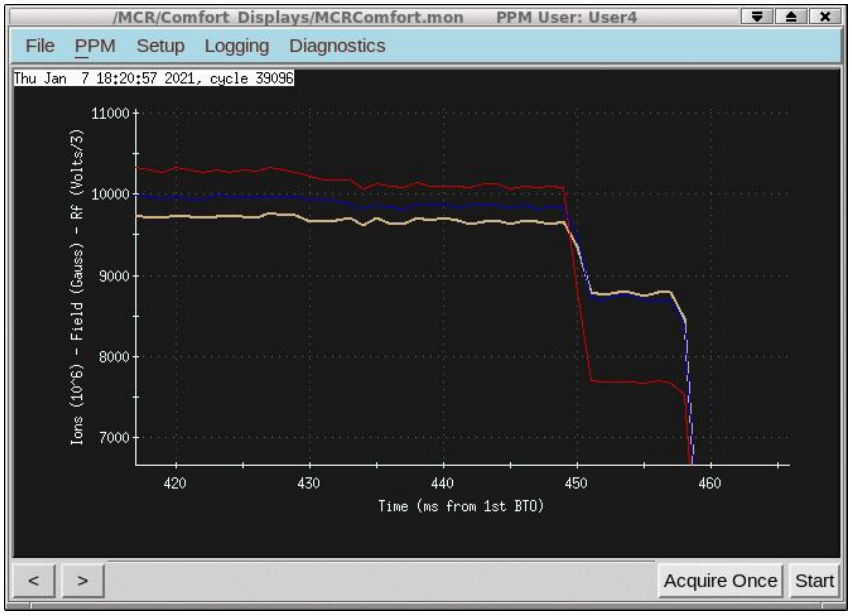

Figure 4.7: Snapshot of the Booster current transformer, in units of intensity, with three traces showing the beam loss with: AC dipole on (red), AC dipole off (blue), AC dipole on after lowering Q_x by -0.02 (yellow). As only the current transformer signal is shown in the plot, the relevant axis label is ion intensity $\times 10^6$.

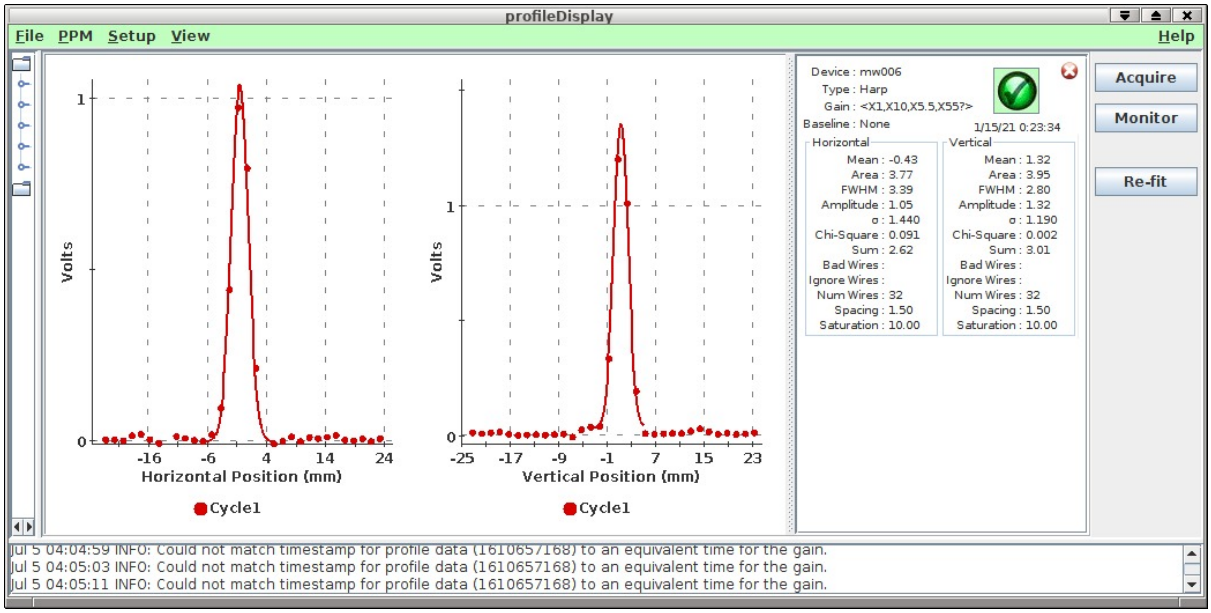

Figure 4.8: Image of MW006 using the application, ProfileDisplay.

4.2 Protons Crossing $|G\gamma| = 0 + \nu_y$

Results of protons crossing the $|G\gamma| = 0 + \nu_y$ resonance as a function of I_m are shown in Fig. 4.9 for several configurations. The polarization is measured in AGS at injection. This is done with the AGS partial snakes off so the stable spin direction in the AGS is vertical and does not follow the periodicity as in Eq. 1.3.36.

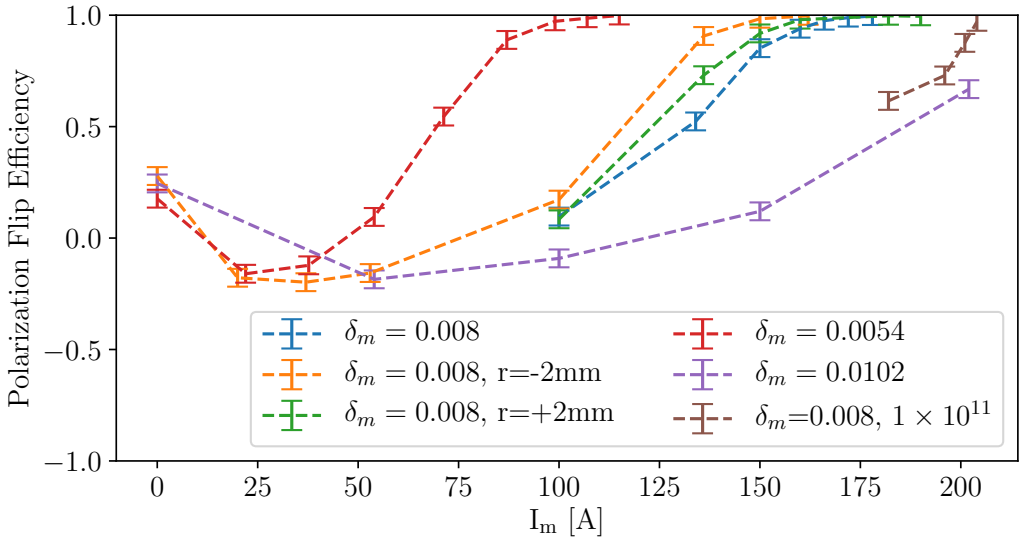

Figure 4.9: P_f of protons crossing the $|G\gamma| = 0 + \nu_y$ resonance for multiple machine configurations and δ_m values. The reported data have their δ_m value and the corresponding intensity listed.

The parts with a negative P correspond to cases where the AC dipole is not sufficiently strong to produce overlap of the two resonances and so the particle crosses two intrinsic resonances, one at $|G\gamma| = 0 + \nu_y$ and the other at $|G\gamma| = 0 + \nu_y + \delta_m$ as seen in Fig. 4.10. The resonance strength is calculated from Eq. 1.3.31, where P_i uses the polarization value

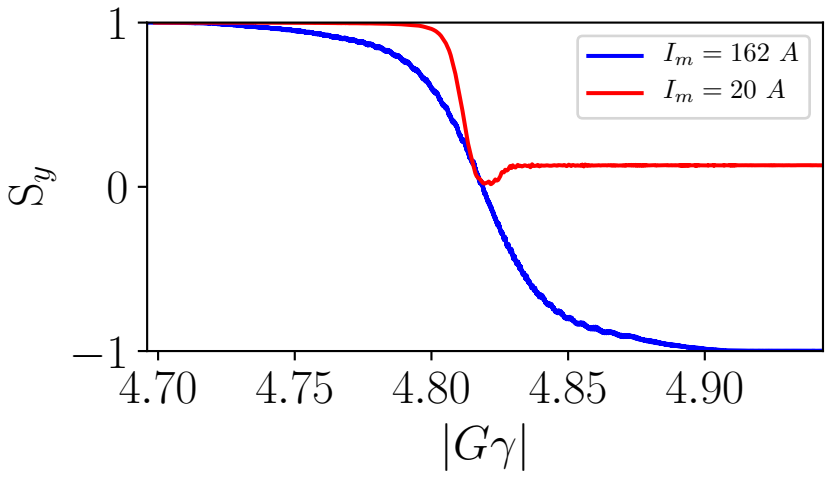

Figure 4.10: Comparison of protons crossing the $|G\gamma| = 0 + \nu_y$ resonance with $I_m = 20\ A$ and $I_m = 162\ A$

after crossing both the $|G\gamma| = 0 + \nu_y$ and $|G\gamma| = 0 + \nu_y + \delta_m$ resonances, and P_f is the

value of resonance crossing in the absence of the AC dipole pulse. Select curves from Fig. 4.10 are shown in Fig. 4.11 relative to Y_{coh} in place of I_m. From this plot, a gap

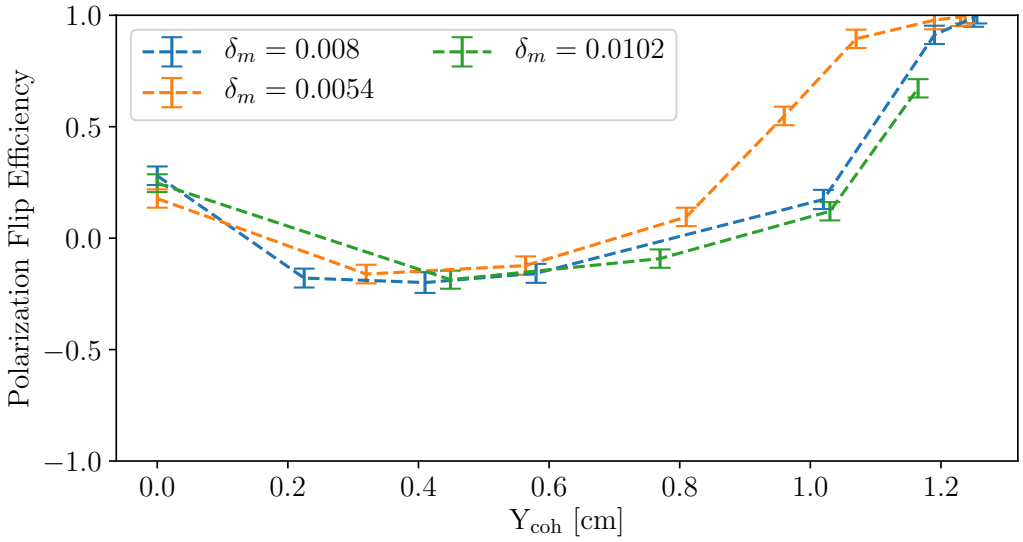

Figure 4.11: Comparison of polarization flip ratio relative to Y_{coh} with δ_m=0.01 (green), 0.008 (blue), and 0.0054 (yellow).

is observed between δ_m=0.0054 and δ_m $\geq$0.008 as the lower value of δ_m has improved overlap between the two spin resonances so is able to full spin-flip with less Y_{coh}.

As observed in Fig. 4.12, protons were unable to reach amplitudes that match theory as the preliminary beam dynamics experiments (Section 4.1). The cause of this is discussed in detail in Sec. 4.2.4. Because of the reduced Y_{coh}, the beam was scraped vertically to reduce the emittance which also reduces the required $B_m l$ to full spin-flip. With σ_y = 1.23 mm and $\epsilon_K(1.23\ mm)$ from Tab. 4.1, the minimum Y_{coh} for a full spin-flip is $Y_{coh,min}$ = 1.22 cm from Eq. 1.3.41. The measured RMS width on MW006 after reducing the intensity to N=0.5 $\times$ 10^{11} protons was σ_y=1.23 mm, instead of σ_y=1.8 mm. The resonance strength is calculated using Eq. 1.3.31 and shown in Tab. 4.1. This shows the resonance strength calculated using nominal emittance through the preceding simulations matched that from the experiment.

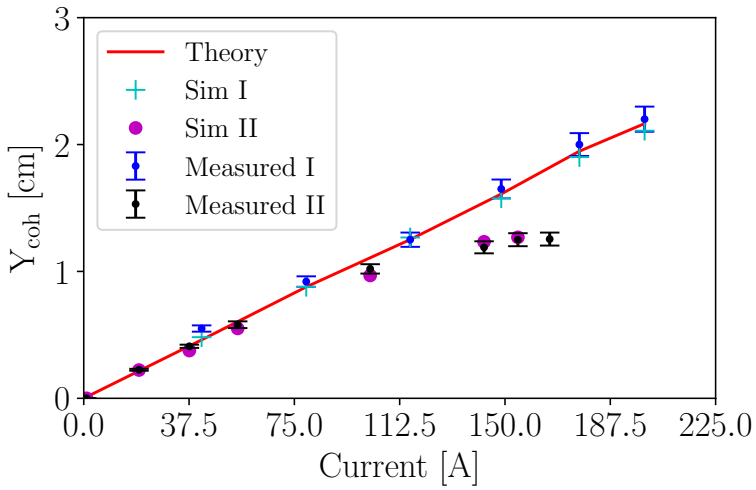

Figure 4.12: Measured Y_{coh} compared to theory and simulation for the experimental and pre-experimental period.

Table 4.1: Comparison of ϵ_K from simulation and experimental results. Simulation value from Tab. 2.2.

	Simulation	Experiment
σ_y [mm]	1.83	1.23
$\epsilon_K(\sigma_y)$	0.002460	0.001905
ϵ_K(1.83 mm)	0.002460	0.002324

4.2.1 Bunch Length Control

As discussed in Sec. 3.3.1, having a longer bunch improves conditions for a full spin-flip by further minimizing δp. Due to the extended setup time for a longer bunch, comparison is made with a shorter bunch where instead of the h=2 cavity being phased to increase the bunch length, it is in phase with the h=1 RF to squeeze the bunch shorter from a full-width of 120 ns to 80 ns. Fig. 4.13 shows that the shorter bunch has reduced spin flipping efficiency.

A larger bunch length can also cause the bunch to be elongated in the vertical phase space due to different particles receiving different kicks, Fig. 4.14. Each particle's kick is still in phase with itself and thus does not reduce spin-flip efficiency or cause emittance dilution.

This was implemented initially into a matrix transport code, see App. A.3, and later in Zgoubi with the SCALING keyword with option -88.3 that applies vertical kick based

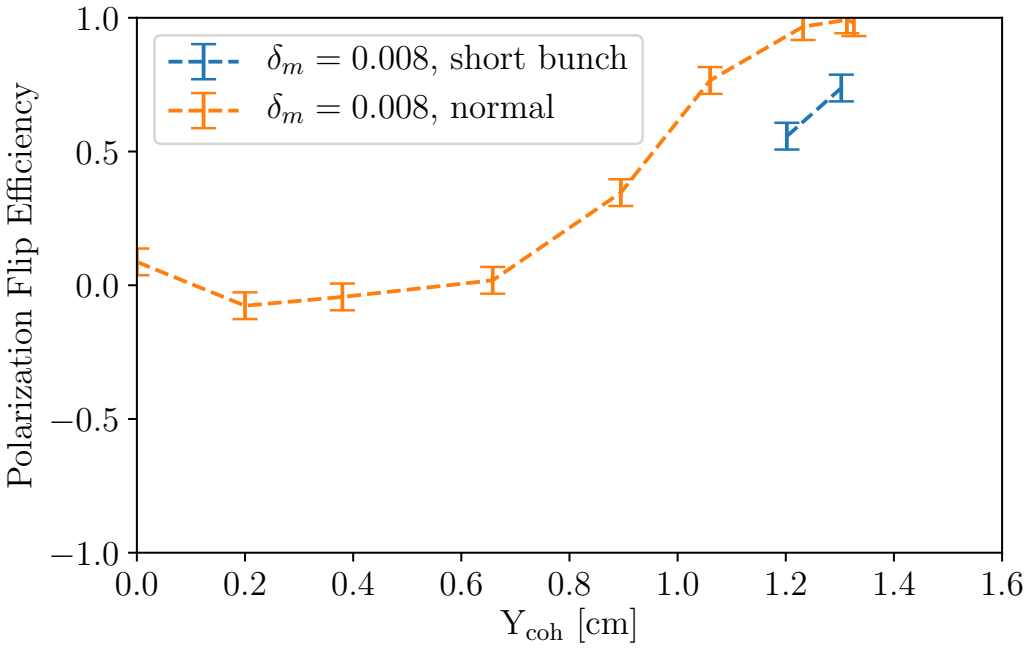

Figure 4.13: P_f comparison for a normal and short bunch.

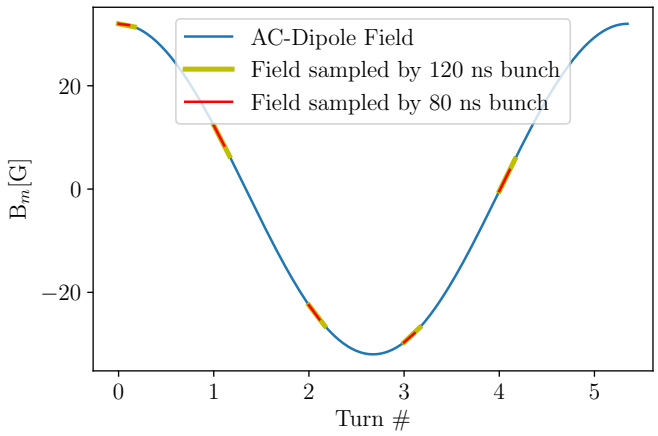

Figure 4.14: One AC dipole period with a normal 120 ns bunch and a smaller 80 ns bunch.

on longitudinal phase. These beam dynamics results are confirmed with a simple beam dynamics tracking code written in python. Results from Zgoubi on a single turn is shown in Fig. 4.15.

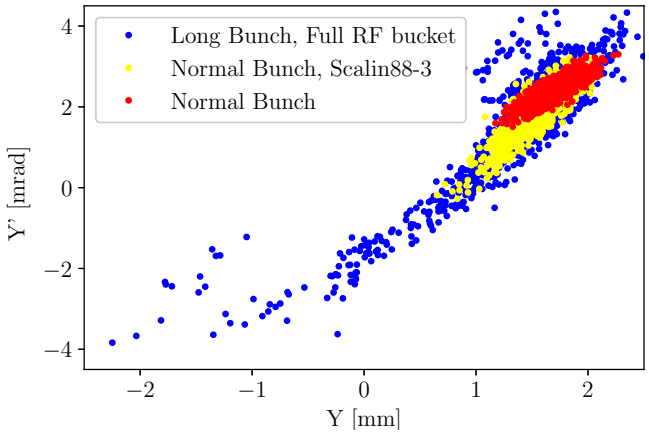

Figure 4.15: A bunch excited by the AC dipole at large amplitude (Normal Bunch), with AC dipole kick based on longitudinal coordinate (Normal Bunch, Scalin88-3), and a long bunch that fills the RF bucket that shows large amount of filamentation.

4.2.2 AC Dipole Operation with Extraction Bumps

As the extraction bumps are ramped up, the large residual that is left causes a decrease in $1-Q_y$ by feed down, as seen in Fig. 4.16. This results in a reduction of δ_m as $B_m l$ is being

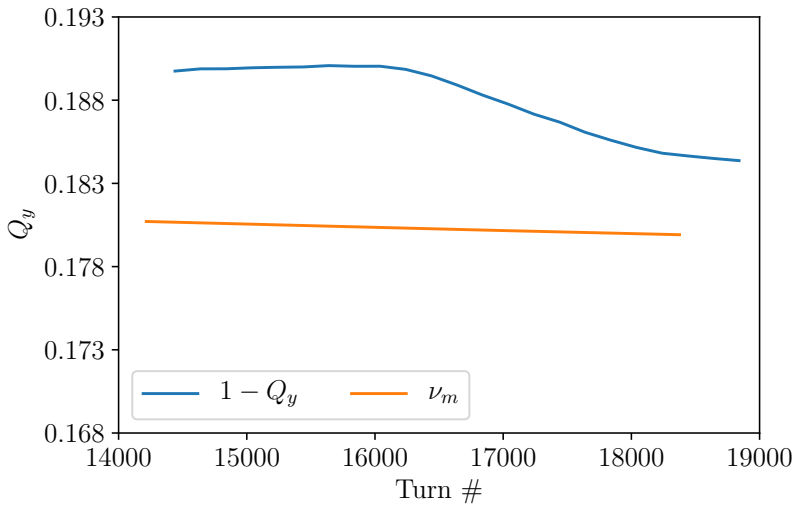

Figure 4.16: 1-Q_y and ν_m for the AC dipole pulse while the extraction bumps are ramping up.

ramped down, resulting in a non-adiabatic ramp down of Y_{coh}. This can be observed on Fig. 4.17 where:

- Ramp up of extraction bumps causes vertical tune to start decreasing at turn #16250.

- Ramp down of AC dipole begins at turn #16667.
- The AC dipole is ramped down at turn #18920 where there is still some Y_{coh} due to the non-adiabiticity of the ramp down.

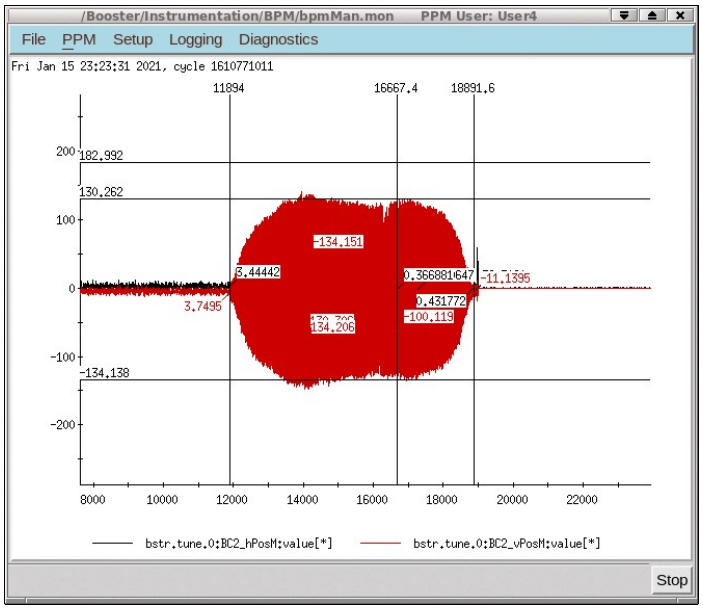

Figure 4.17: General Purpose Monitor (GPM) of the BPM showing the structure of Y_{coh}.

The extraction bumps are installed into Zgoubi with the settings used during the experimental period. The effect this has on Y_{coh} is shown in Fig. 4.18 with measurements and simulations. This figure uses $B_m l = 4.12$ G $\cdot$ m

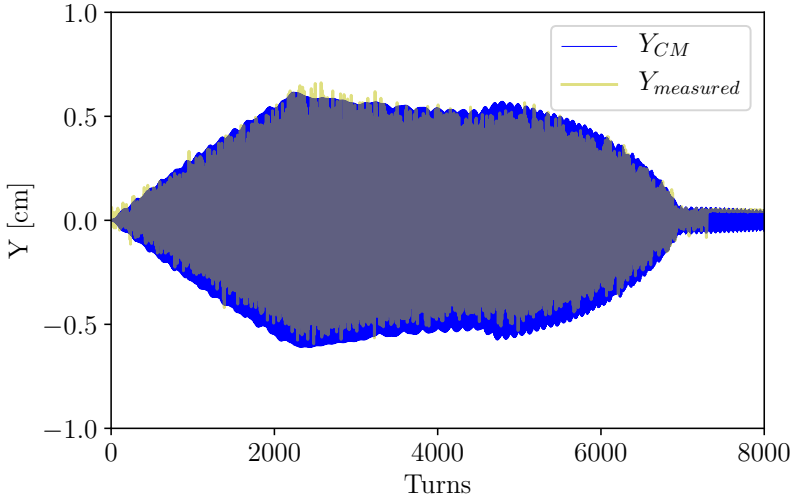

Figure 4.18: Simulations of 1,000 particles crossing the $|G\gamma| = 0 + \nu_y$ resonance with I_m=53 A and resulting beam position from simulation, Y_{CM}, compared to measurements, $Y_{measured}$.

4.2.3 AC Dipole Timing scan

To separate the AC dipole pulse from the extraction bumps, a scan of the pulse start time (beginning with 54000 Gauss Counts (GCs)) with corresponding polarization is shown in Fig. 4.19. This scan shows a broad porch of approximately 0.8 ms where the spin-flip

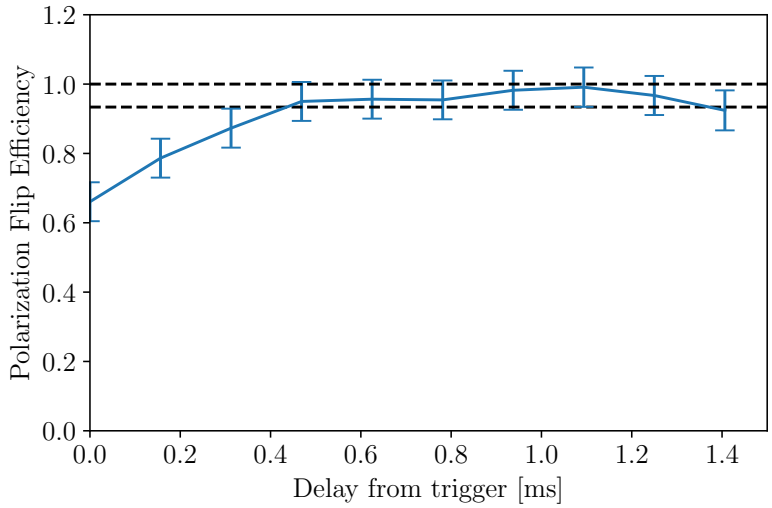

Figure 4.19: P_f versus AC dipole delay.

efficiency remains constant. Here, 10 Gauss counts corresponds to a change of 1 G. The mechanism for polarization loss is crossing the resonance on or near the AC dipole ramp

in place of on the flat portion. To separate the extraction bumps from the AC dipole pulse, the extraction bumps were changed so that extraction occurs as the bumps are ramping and the AC dipole pulse is moved 0.2 ms earlier. The resulting BPM response is shown in Fig. 4.20.

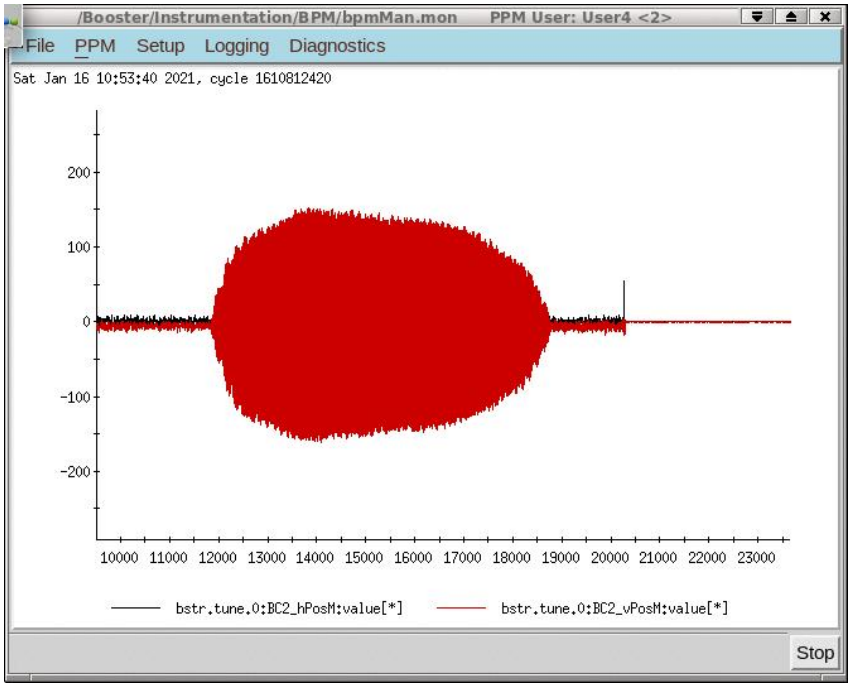

Figure 4.20: BPM response after separation of extraction bumps and AC dipole pulse.

4.2.4 AC Dipole Operation with Synchro

Synchro is the synchronization of the Booster to the AGS RF so that the bunch extracted out of Booster enters the AGS in the correct RF phase. This is done by taking a reference table of frequencies that the Booster RF will maintain at different times in the cycle. To maintain the specified frequency, the RF will modulate the beam radius as needed.

The large amplitude betatron motion driven by the AC dipole causes an increase in path length. This change in radius follows [35],

$$\Delta r = \frac{1}{2}\left\langle \frac{1+\alpha_y}{\beta_y} \right\rangle \frac{Y_{coh}^2}{2\beta_y} r \tag{4.2.1}$$

The resulting change in radius changes the OCO (optimal closed orbit) by a reduction in energy. This new OCO does not pass through the sextupoles' center, causing feed down

and a change in ν_y. This change in ν_y has a corresponding change to δ_m and Y_{coh}. From Eq. 4.2.1, the change in radius is quadratically proportional to the change in vertical amplitude. The BPM structure shown in Fig. 4.21 is observed via comparison between measured data ($Y_{measured}$) and simulation (Y_{CM}). To simulate the change in radius, the

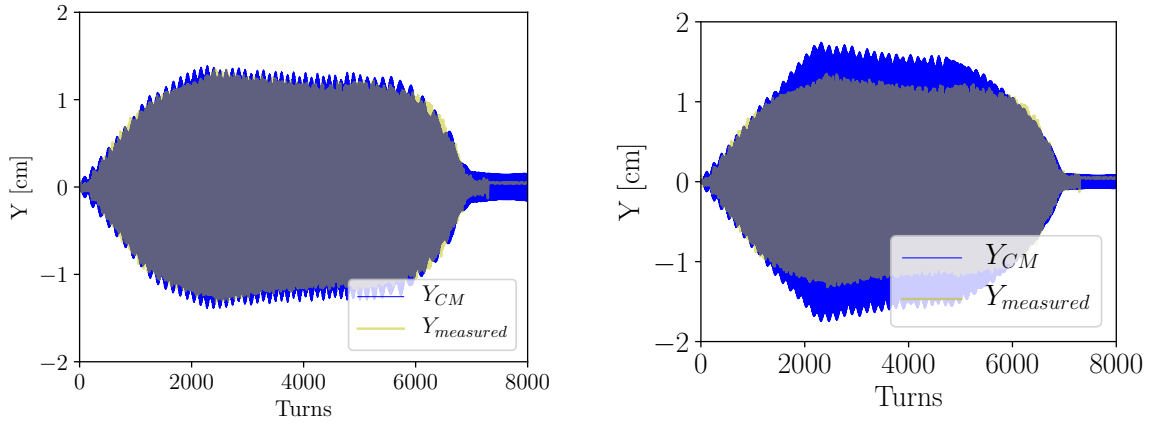

Figure 4.21: Simulations of 1,000 particles crossing the $|G\gamma| = 0 + \nu_y$ resonance with I_m=136 A and resulting beam position from simulation, Y_{CM}, compared to measurements, $Y_{measured}$. Radial change during AC dipole ramp (left), no radial change during simulation (right).

reference momentum is scaled in Zgoubi starting at turn 1200 to the end of the cycle. A comparison of simulation where radial shift on vs off is also shown in Fig. 4.21 between the left and right plots. The effect this has on Y_{coh} is also observed in Fig. 4.12 where previous measurements, Fig. 4.6, showed strong correlation between theory, simulation, and measurement. In line with these comparisons, Fig. 4.22 shows a FFT comparison between the measured BPM data and simulation. Although there is a baseline offset, the structure shows that the simulations exhibit the same frequency excitation as the experiment.

As the OCO changes horizontally, the vertical aperture of the beam pipe changes. At the horizontal edge of the beam pipe (8.3 cm from center), the aperture is reduced from 3.5 cm to 2.2 cm. This change in vertical aperture is shown in Fig. 4.23 with a $\sigma_x = \sigma_y$ =1.8 mm beam.

Further improvements of the zgoubi model were gained with the modification to the dipole fringe fields, Sec A.2. The results of these simulations show good agreement with

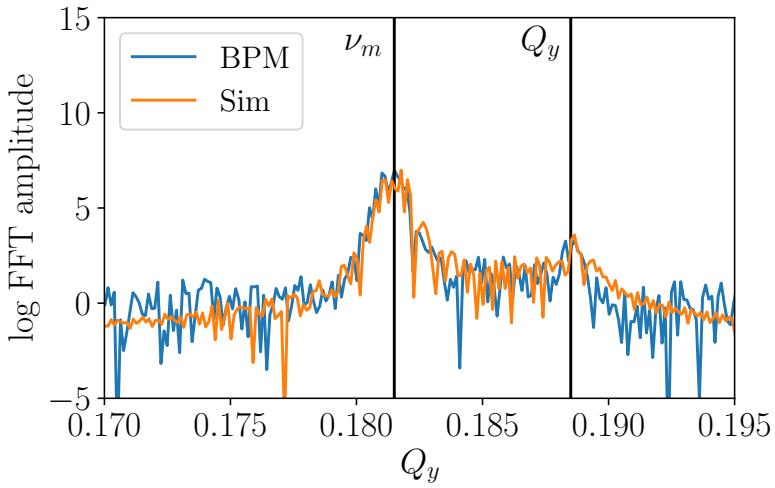

Figure 4.22: Comparison of FFTs of real data and simulation.

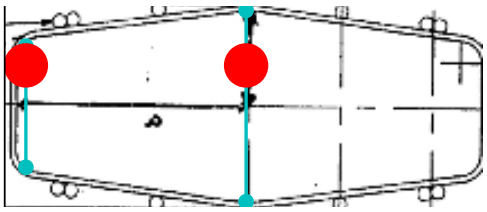

Figure 4.23: Booster vacuum chamber cross section showing reduced aperture with large x_{co} and σ_y=1.83 mm round beam.

measurements as seen in Fig. 4.24.

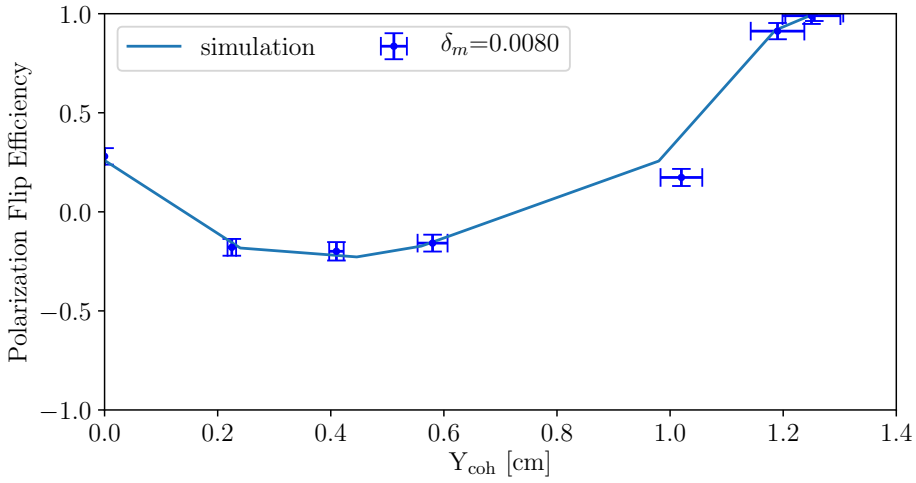

Figure 4.24: Plot showing experimental data of $\delta_m = 0.008$ compared with simulation, with $N_{protons} = 0.5 \times 10^{11}$.

4.2.5 Separating Synchro from AC dipole pulse

Extracting at $|G\gamma| = 5.5$ will allow the crossing of the $|G\gamma| = 0 + \nu_y$ resonance 15 ms before extraction. For this to be possible, the ramp rate will need to be changed from the nominal 6.5 T/s to 5.1 T/s after the resonance is crossed. This will allow the resonance crossing to occur in an unadulterated state.

The $|G\gamma| = 5$ resonance was crossed during the experimental period and found the response of sin5v and cos5v to have very poor response. Initial currents of [sin5v,cos5v]=[5 A, -9.6 A] are scanned via simulation and shown in Fig. 4.25. From the scan, the initial

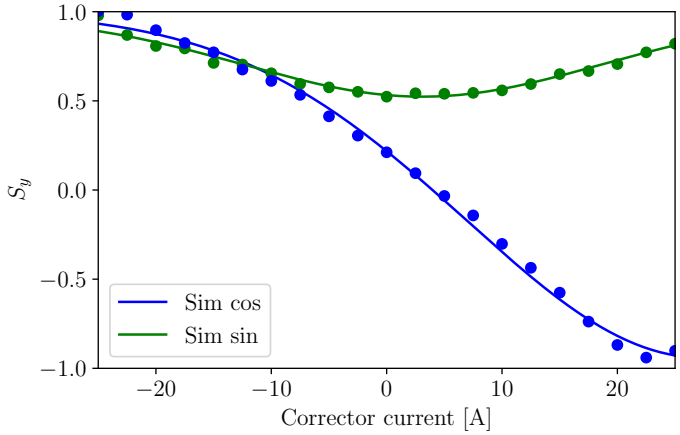

Figure 4.25: Scan of h=5 correct currents for protons crossing $|G\gamma| = 5$.

currents are far from optimal. These simulations show the optimal harmonic corrector currents are [sin5v, cos5v]=[0.2 A, 24.3 A] to spin-flip across $|G\gamma| = 5$. This complications crossing the $|G\gamma| = 5$ with protons as the corrector currents are at their limit.

Another alternative is setting $\nu_y = 4.1762$ with extraction at $|G\gamma| = 4.93$ which will have $|G\gamma| = 0 + \nu_y$ being crossed 15.8 ms prior to extraction with the nominal ramp rate of 6.5 T/s. This configuration will require additional setup time as the standard setup has Q_y <0.5 but has the benefit of avoiding the $|G\gamma|$=5 imperfection resonance.

For helions at $|G\gamma| = 6 + \nu_y = 10.174$, there is 14.4 ms between it and extraction at $|G\gamma| = 10.5$ with a ramp rate of 2 T/s. With the AC dipole ramp ending at $|G\gamma| = 10.277$, the ramp rate would need to be lowered after the pulse to 1.32 T/s to allow the AC dipole pulse to be completed before the synchro processes begin.

Chapter 5

Summary

Helions in the Booster have a number of depolarizing resonances that need to be compensated for to ensure high polarization transmission to the EIC, as they are accelerated to extraction corresponding to $|G\gamma| = 10.5$. This higher extraction energy also allows the AGS $|G\gamma| = 0 + \nu_y = 8.9$ to be avoided. Dynamic aperture simulations at $|G\gamma| = 10.5$ and $|G\gamma| = 7.5$ show the higher AGS injection energy has a much larger admittance due to reduced optical defects from the AGS Siberian snakes [55]. This improved admittance will allow both the vertical and horizontal tunes to be placed within the spin tune gap at injection.

Simulations of harmonic scans at the $|G\gamma|$ =3 and 4 imperfection resonances for protons match closely to experimental data. The method used was extended to helions for their six imperfection resonances. These simulations show that there is sufficient corrector current to either correct or exacerbate each orbit harmonic [18, 56] at each of the resonances.

The aperture of the Booster was measured and confirmed to be the documented value. For helions crossing the two intrinsic resonances, simulations show that a full spin-flip will occur with coherent oscillations that are within the limits of the beampipe [16, 17, 57]. An AC dipole were designed and installed in the Booster for these two resonances [58, 59]. AC dipole simulations showed that controlling the chromaticity was imperative in maintaining these coherent oscillations without losing particles.

These simulations show that the AC dipole can spin-flip protons through the $|G\gamma| = 0 + \nu_y$ resonance in Booster. The criteria for a full spin-flip of protons crossing the $|G\gamma| = 0 + \nu_y$ is similar to that of helions at $|G\gamma| = 12 - \nu_y$, providing a convenient proof of principle experiment. These simulations were done with a fixed modulation frequency of the AC dipole which mimics the operating mode that is more realistic. It was determined that the resulting modulation tune sweep does not dilute the effectiveness of spin-flipping.

Measurements from a period before extracting beam into the AGS showed strong agreement with theory and simulation. These measurements include a scan of δ_m and $B_m l$. Scans of beam loss as a function the resonance proximity parameter showed that reduced chromaticity minimized particles lost by minimizing spread of δ_m. This period also showed emittance growth to be minimal when operating the AC dipole.

The experiment of protons crossing the $|G\gamma| = 0 + \nu_y$ showed the AC dipole was able to achieve a full spin-flip. Due to the operation of the AC dipole near extraction, there were two processes that interfered its operation: extraction bumps, and Booster to AGS synchro. The extraction bumps ramping up caused the AC dipole pulse to ramp down non-adiabatically which caused the coherent oscillations to continue. After a timing scan of the start of the AC dipole pulse, the AC dipole pulse was separated from the extraction bumps, eliminating the interference. The large amplitude oscillations from the AC dipole caused a change in path length which caused the RF system to change the radius in order to maintain the correct frequency between Booster and AGS. This radial change caused horizontal excursions into the sextupoles where feed-down caused a shift in ν_y, a corresponding increase in δ_m and a reduction of Y_{coh}. Because of the reduced Y_{coh}, the beam had to be scraped to reduce ε_y so a spin-flip could occur. The calculated value of ϵ_K from this period matched the expectations from theory and simulation. The model was modified to reflect these effects and the agreement between simulation and experimental data was recovered.

Based off the AC dipole results from protons crossing the $|G\gamma| = 0 + \nu_y$, polarized helions will be able to spin-flip through both the $|G\gamma| = 12 - \nu_y$ and $|G\gamma| = 6 + \nu_y$.

Despite the $|G\gamma| = 6 + \nu_y = 10.174$, a small reduction in the ramp rate would allow the AC dipole pulse to be completely separated from synchro. Studies using polarized protons can continue to take place to separate the AC dipole pulse from synchro and crossing higher order imperfection resonance, which will lend to the future development of polarized helions. With the polarized helion upgrade to EBIS now scheduled for the 2022 shutdown, polarized helion studies can soon take place in the injectors in preparation for the EIC.

Appendix A

Appendix I

A.1 Tune Kicker Design

The original tune kickers were unable to provide sufficient coherent amplitude above $B\rho = 9.3$ T $\cdot$ m where the maximum rigidity of the Booster is 17.24 T $\cdot$ m. To support taking tune measurements at this maximum rigidity, a new magnet is installed for the horizontal tune kicker supply. The horizontal magnet is increased from 12 cm to 20 cm, and a change in gap from 9 cm to 8.6 cm, providing $\times$1.74 more integrated field strength, as per Eq. 1.2.62. The vertical magnets new length of 50 cm provides a kick $\times$4.2 stronger.

Table A.1: Measurements of pulse parameters with the new magnets. Rise time defined as 0-90% of peak amplitude and flat time is 90% to 90%.

	pulse type	rise time (90%) [ns]	flat time [μs]
Horizontal	long	281	3.0
Vertical	long	500	2.8
Horizontal	short	221	1.0
Vertical	short	300	0.9

The fall time is twice the length of the rise time which puts the total length of the short pulse 1.2 μs which puts the pulse length more than one period long above f_{rev}=667 kHz. Similarly the long pulse is 4.3 μs and extends beyond one turn above f_{rev}=232 kHz. As part of this, the BPM electronics were also upgraded to improve data collection and analysis. This is an ongoing project to have it sufficiently robust to accommodate the full array of ions and intensities that run in the Booster. During the experimental period,

the intensity of protons were kept within the operating range of the BPMs.

A.2 Booster Main Dipole Fringe Fields

The original fringe fields used were from the Saturne magnets. To improve the accuracy of the Booster model in zgoubi, the pole tips for the main dipoles were modelled using Opera by Nicholaos Tsoupas. Their analysis found these fringe fields in the Booster add a small sextupole component as seen in Tab. A.2.The fringe field is seen in Fig. A.1 for B_{MM}=1.21 T where s=0 is set so fringe field contribution for $s > 0$ matches the missing field from $s < 0$.

Table A.2: Fringe field components normalized to B_0 and analyzed at r=1 inch.

	Low Energy	Medium Energy
B_0/B_0	1.0	1.0
B_1/B_0	0.00	0.00
B_2/B_0	-0.00044	-0.00094
B(0,0) [T]	0.55	0.91

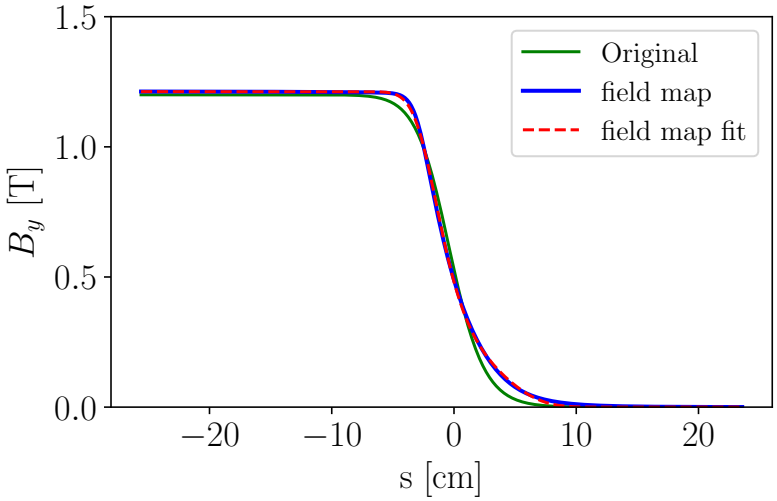

Figure A.1: Fringe field of the Booster main dipole with B=1.21 T

The fringe fields are fitted according to [42]

$$F = \frac{1}{1 + \exp P(s)} \tag{A.2.1}$$

with

$$P(s) = C_0 + C_1\left(\frac{s}{\lambda}\right) + C_2\left(\frac{s}{\lambda}\right)^2 + C_3\left(\frac{s}{\lambda}\right)^3 + C_4\left(\frac{s}{\lambda}\right)^4 \tag{A.2.2}$$

where C_0 through C_4 are the coefficients and λ is the extend of the fringe field.

A.3 Particle Tracking Code

The particle tracking code takes the one turn 6x6 Courant-Snyder matrix, Eq. 1.2.19 for 2x2 as a function of s. Each particle has its new coordinates calculated as normal safe for y' that receives an additional kick from the AC dipole as,

$$y'(n+1) = \frac{(1+\alpha_y^2)}{\beta}\sin(2\pi\nu_y)y_n + (\cos(2\pi\nu_y) - \alpha_y\sin(2\pi\nu_y))y'_n + \frac{B_m l}{B\rho}\cos(2\pi dL\nu_m + \phi) \tag{A.3.1}$$

where dL is the position of the particle relative to C. An example 6x6 matrix is

$$M_{66} = \begin{bmatrix} 5.547536 & 0.923280 & 0.000000 & 0.000000 & 0.000000 & 0.770102 \\ 0.923280 & 0.333922 & 0.000000 & 0.000000 & 0.000000 & -0.100014 \\ 0.000000 & 0.000000 & 10.646834 & -1.516733 & 0.000000 & 0.000000 \\ 0.000000 & 0.000000 & -1.516733 & 0.309996 & 0.000000 & 0.000000 \\ 0.000000 & 0.000000 & 0.000000 & 0.000000 & 0.000000 & 0.000000 \\ 0.000000 & 0.000000 & 0.000000 & 0.000000 & 0.000000 & 0.000000 \end{bmatrix} \tag{A.3.2}$$

A Gaussian distribution is generated in all planes and then the particles position with each turn is calculated. The results of these simulations are shown in Fig. A.2 which were then placed into zgoubi as SCALING option -88.3 with results shown in Fig. 4.15.

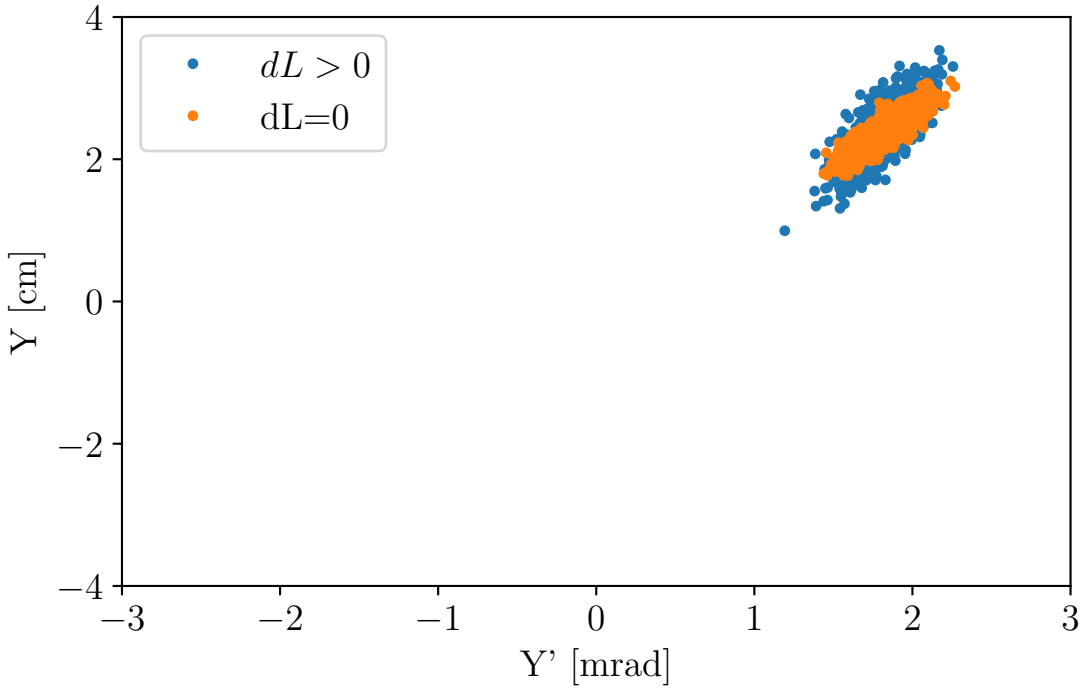

Figure A.2: Comparison of bunched particles undergoing large amplitude coherent oscillations with kick based off of particles longitudinal phase with respect to the AC dipole.

Appendix B

Appendix II

B.1 Resonance Strengths

This section is a compilation of simulations, the results of which are found in Sec. 2.2

B.1.1 Intrinsic Resonances

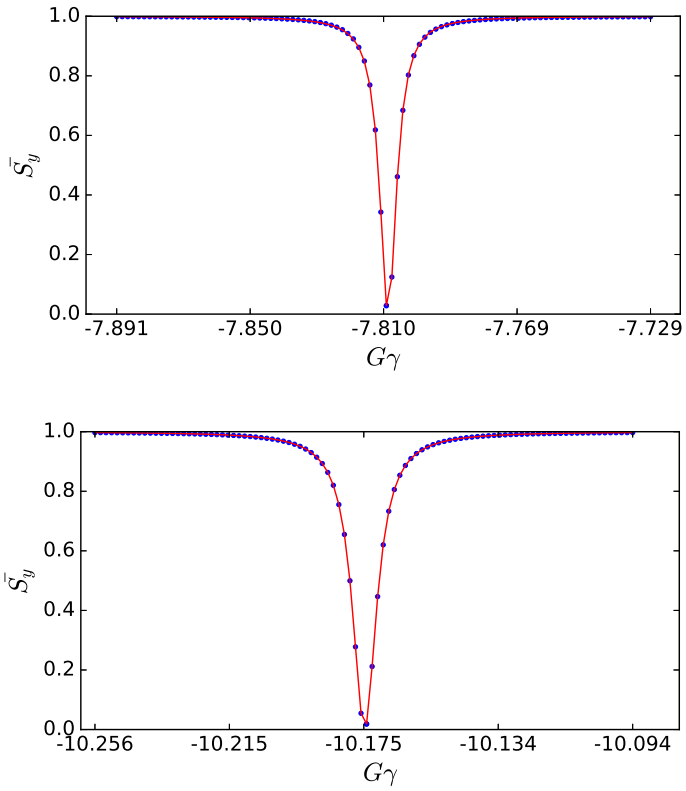

Figure B.1: A simulation of the component of the stable spin direction in the vicinity of the three resonances ($G\gamma = 12 - \nu_y$ (top), $G\gamma = 6 + \nu_y$ (bottom)) using the static depolarization method showing data points (blue) and the fit results using Eq. 1.3.30 (red). (top) $G\gamma = 12 - \nu_y$ resonance shown with a $\varepsilon_{\rm y} = 0.535$ μm particle yields $|G\gamma_R|$=7.8082 and $|\epsilon_K|$=0.003037. (bottom) $G\gamma = 6 + \nu_y$ resonance shown with a $\varepsilon_{\rm y} = 0.369$ μm particle yields $|G\gamma_R|$=10.1742 and $|\epsilon_K|$=0.004294.

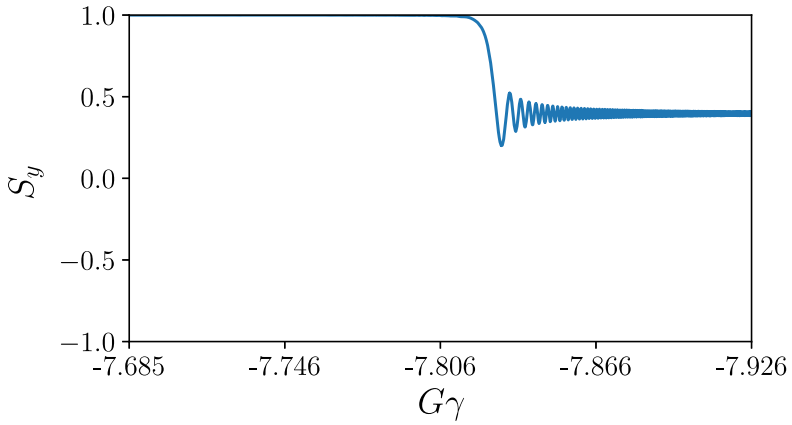

Figure B.2: A simulated measurement of the strength of the $|G\gamma| = 12 - \nu_y$ resonance with a $\varepsilon_y = 0.1\mu m$ particle using the Froissart-Stora.P_f=39.6%, $|\epsilon_K|$=0.001350

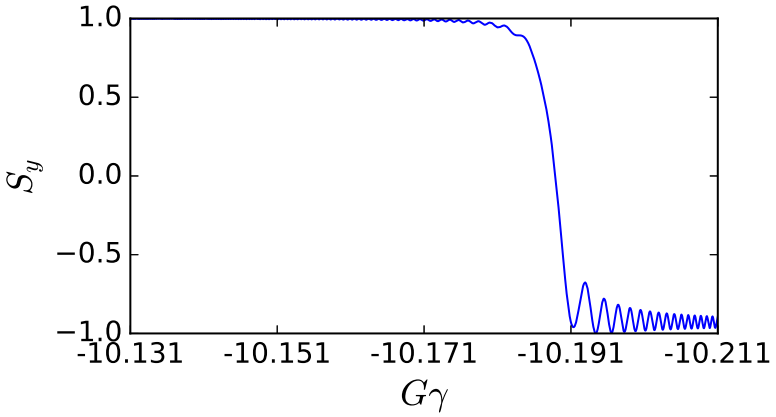

Figure B.3: A simulated measurement of the strength of the $|G\gamma| = 6 + \nu_y$ resonance with a $\varepsilon_y = 0.1\mu m$ particle using Froissart-Stora.P_f=-91.6%, $|\epsilon_K|$=0.002291

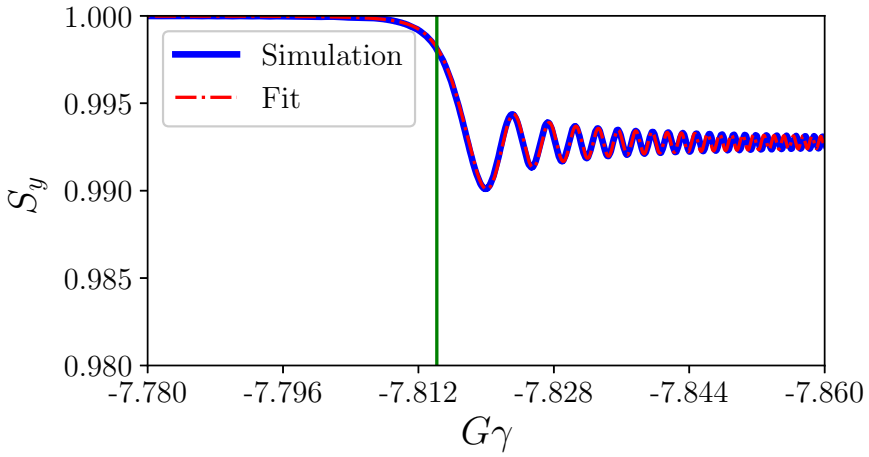

Figure B.4: A simulated measurement of the strength of the 12- resonance with a ε_y = 0.001 μm particle Fresnel integrals. Data points (blue) and the fit using Eq. 1.3.26 and 1.3.27 (red). $G\gamma$=-7.8079, $|\epsilon_K|$=0.000135

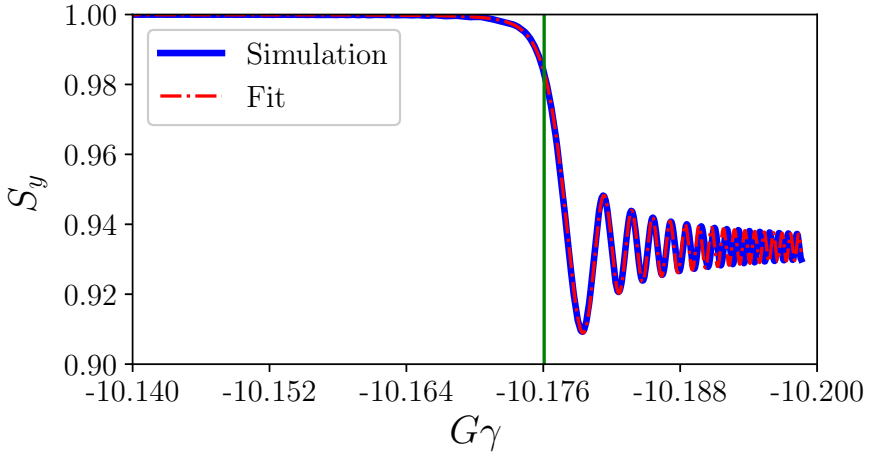

Figure B.5: A simulated measurement of the strength of the 6+ resonance with a ε_y = 0.001 μm particle Fresnel integrals. Data points (blue) and the fit using Eq. 1.3.26 and 1.3.27 (red). $G\gamma$=-10.1739, $|\epsilon_K|$=0.0000238

B.1.2 Imperfection Resonances

B.1.3 Helion Harmonic Scans

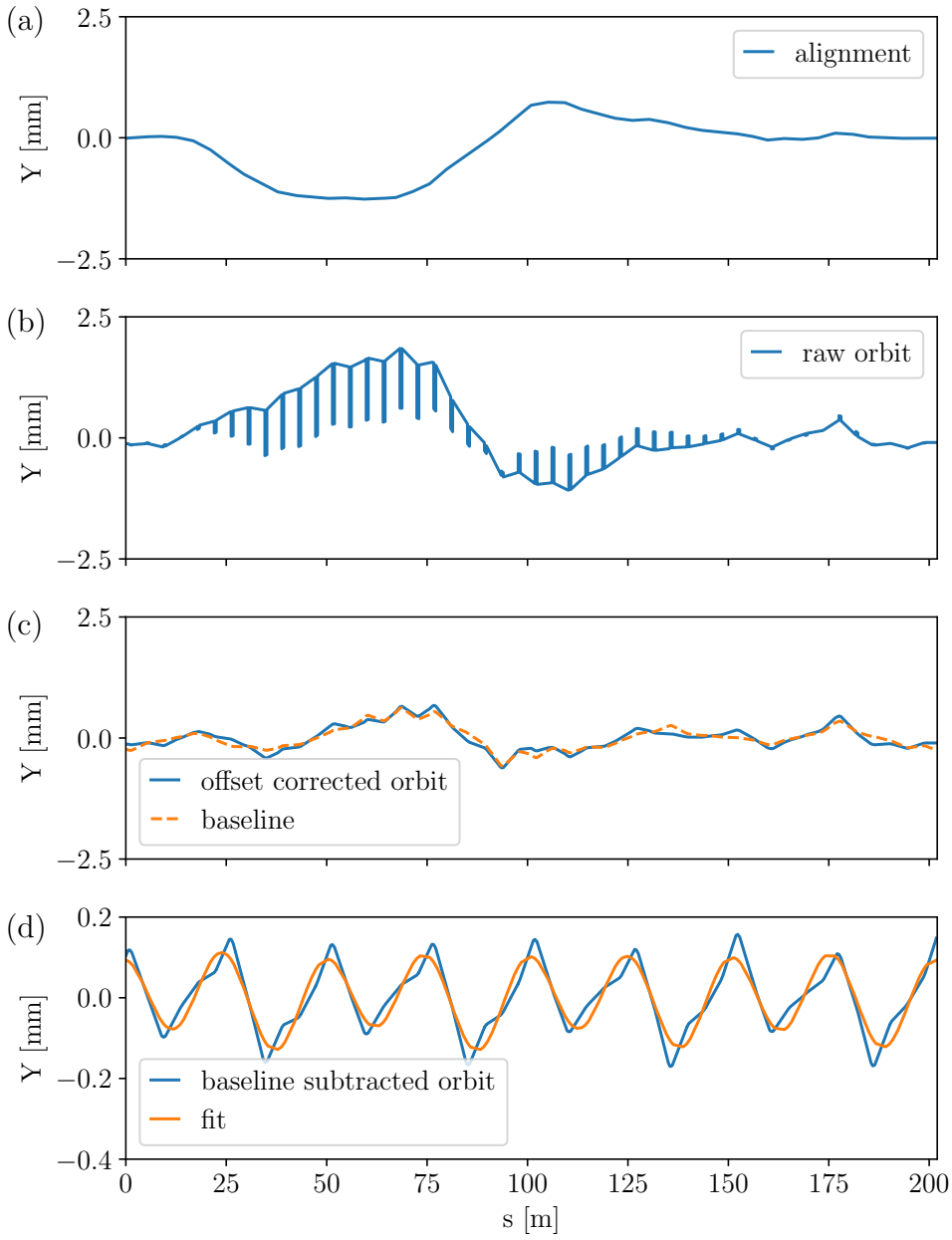

Figure B.6: a) Vertical quadrupole misalignments in the Booster scaled to 65% to match h=4 data; b) orbit output from Zgoubi where discontinuities result from the use of CHANGREF through quadrupoles; c) Orbit after incorporating misalignments; d) Baseline subtracted orbit for helions crossing the $|G\gamma| = 8$ resonance after the h=4, 5 harmonics have been corrected with the addition of h=8. This example has a corrector currents [sin4v, cos4v, sin5v, cos5v, sin8v, cos8v]=[2.097 $B\rho/B\rho(5)$, 0.669 $B\rho/B\rho(5)$, 0.520 $B\rho/B\rho(5)$, 4.296 $B\rho/B\rho(5)$, 4.0 ,-13.0]. The components of the fit results are: [sin4, cos4, sin5, cos5, sin8, cos8]=[0.000254, -0.000022, -0.000019, -0.000043, -0.000216, 0.000997].

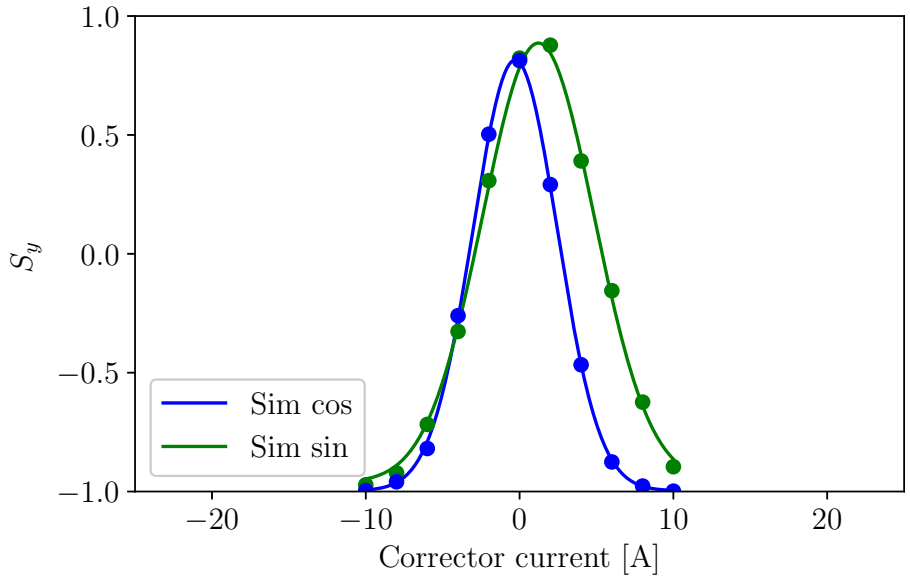

Figure B.7: Helion harmonic scan of current for h=6 after correcting for the h=4, 5 harmonics. Can achieve a full spin-flip with sin8v=6.2 A and cos8v=-10 A which results in I_{max}=18.44 A. Fit data found in Tab. 2.2.

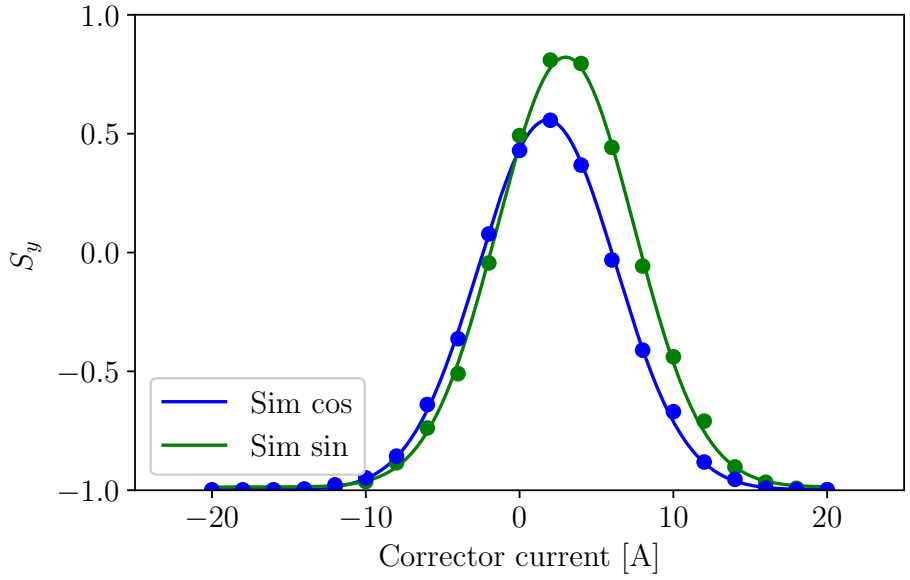

Figure B.8: Helion harmonic scan of current for h=7 after correcting for the h=4, 5 harmonics. Can achieve a full spin-flip with sin7v=-10 A and cos7v=-10 A which results in I_{max}=24.14 A. Fit data found in Tab. 2.2.

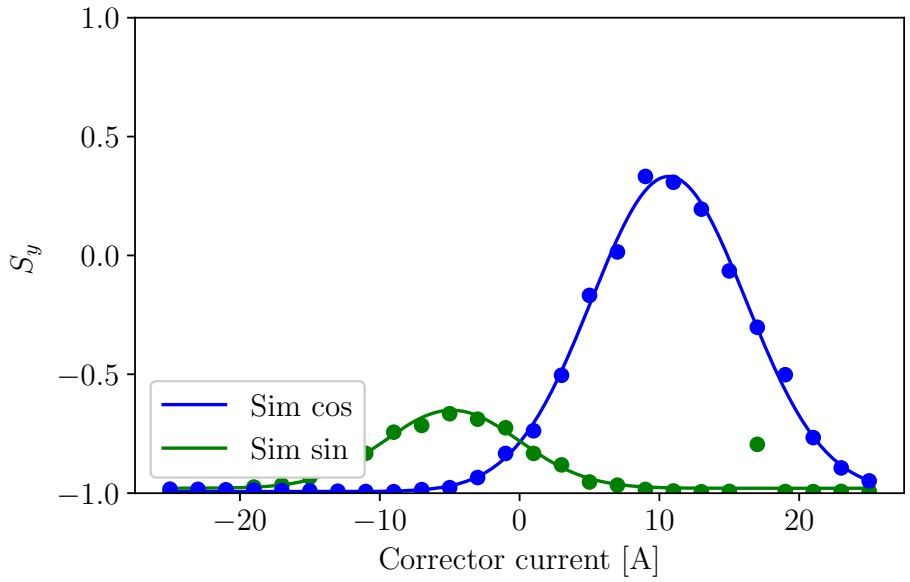

Figure B.9: Helion harmonic scan of current for h=8 after correcting for the h=4, 5 harmonics. Can achieve a full spin-flip with sin8v=2.9 A and cos8v=-18 A which results in I_{max}=24.92 A. Fit data found in Tab. 2.2.

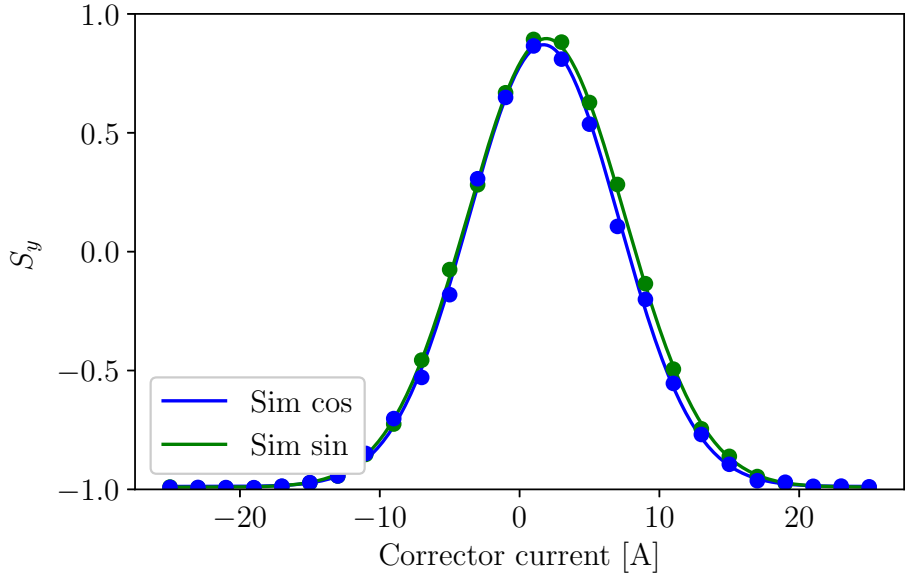

Figure B.10: Helion harmonic scan of current for h=8 after correcting for the h=4, 5 harmonics. Can achieve a full spin-flip with sin8v=2.9 A and cos8v=-18 A which results in I_{max}=24.92 A. Fit data found in Tab. 2.2.

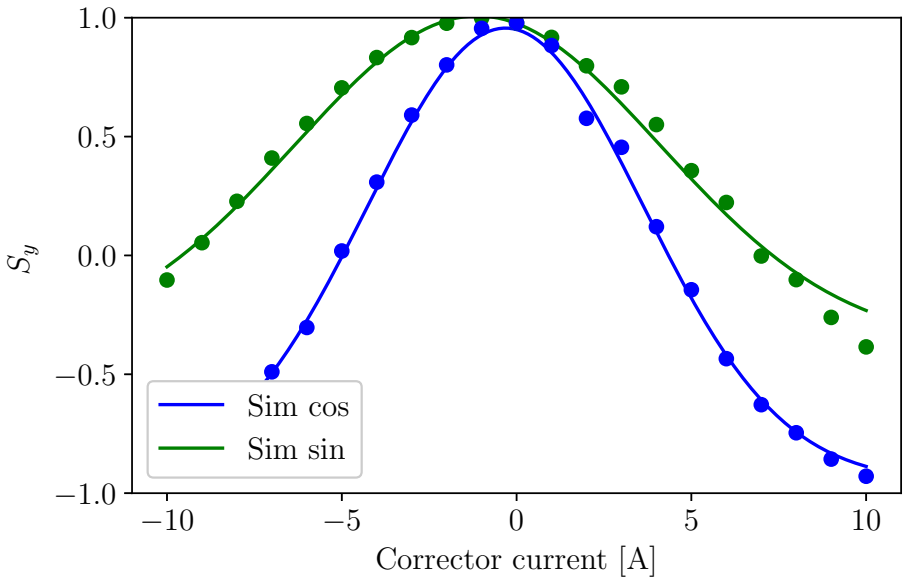

Figure B.11: Helion harmonic scan of current for h=9 after correcting for the h=4, 5 harmonics. Can achieve a full spin-flip with sin9v=-1.074 A and cos9v=0.0 A which results in I_{max}=17.92 A. Fit data found in Tab. 2.2.

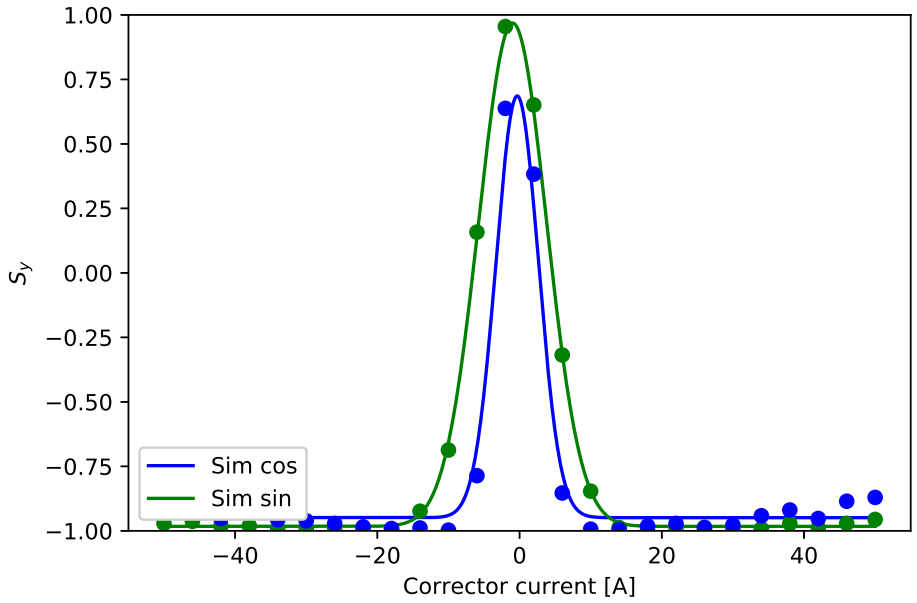

Figure B.12: Slow ramp helion harmonic scan of current for h=9 after correcting for the h=4, 5 harmonics. Can achieve a full spin-flip with sin9v=-20.0 A and cos9v=0.0 A which results in I_{max}=24.33 A. Fit data found in Tab. 2.2.

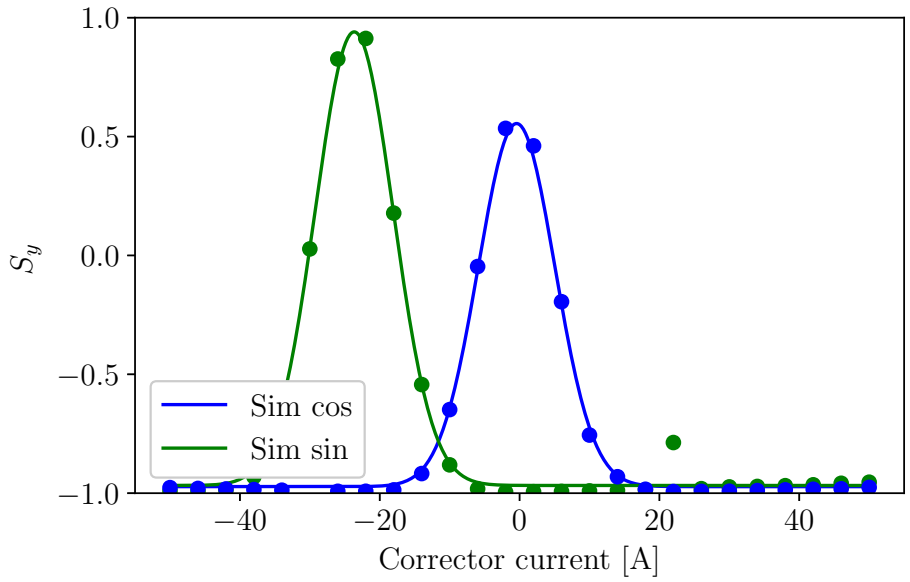

Figure B.13: Helion harmonic scan of current for h=10 after correcting for the h=4, 5 harmonics. Can achieve a full spin-flip with sin10v=9 A and cos10v=10 A which results in I_{max}= 24.94A. Fit data found in Tab. 2.2.

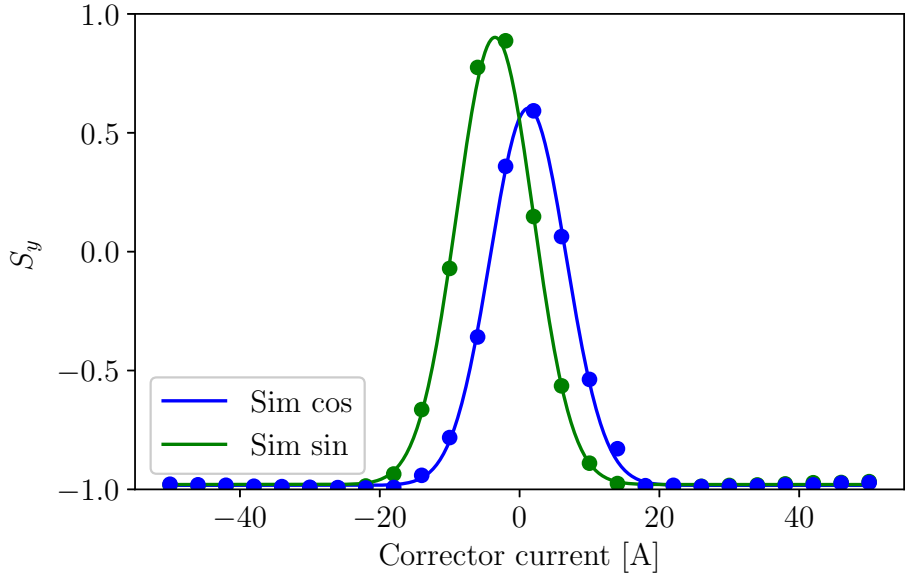

Figure B.14: Helion harmonic scan of current for h=10 after correcting for the h=4, 5 harmonics. Can achieve a full spin-flip with sin10v=9 A and cos10v=10 A which results in I_{max}= 24.94A. Fit data found in Tab. 2.2.

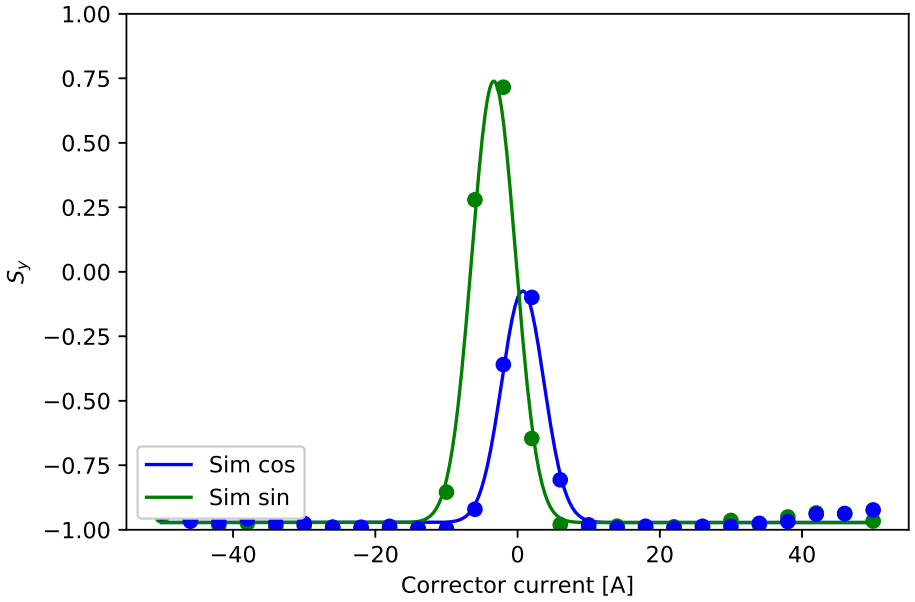

Figure B.15: Slow ramp helion harmonic scan of current for h=10 after correcting for the h=4, 5 harmonics. Can achieve a full spin-flip with sin10v=9 A and cos10v=10 A which results in I_{max}= 24.94A. Fit data found in Tab. 2.2.

B.1.4 Resonance Crossing

B.1.4.1 Static

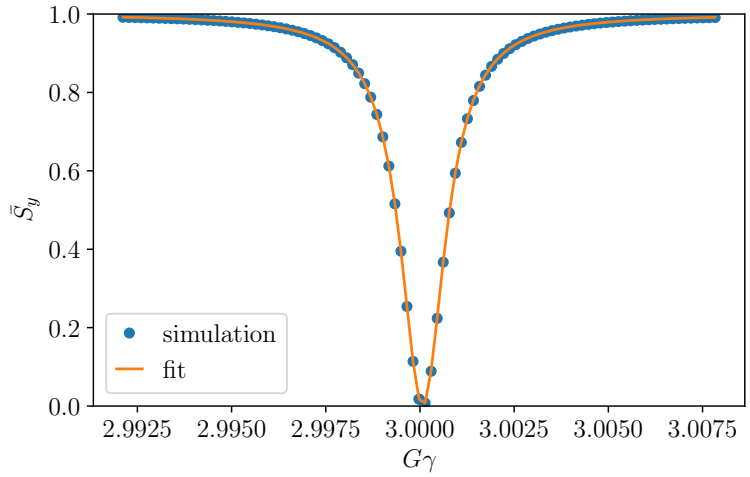

Figure B.16: Static depolarization of protons at $|G\gamma| = 3$, ϵ_K=0.000714.

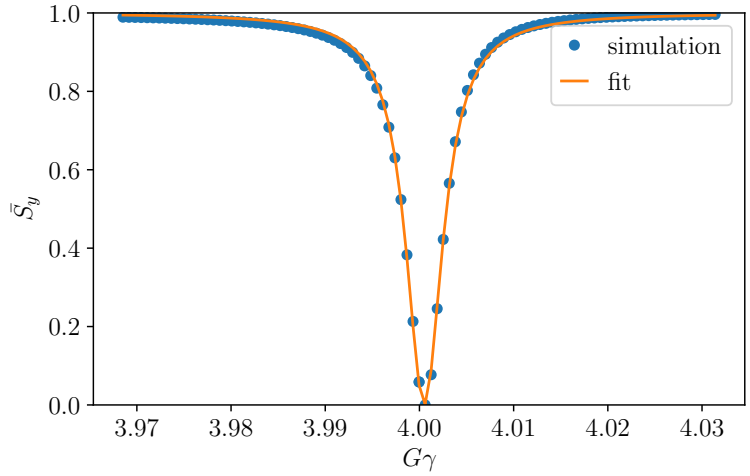

Figure B.17: Static depolarization of protons at $|G\gamma| = 4$, ϵ_K=0.002396.

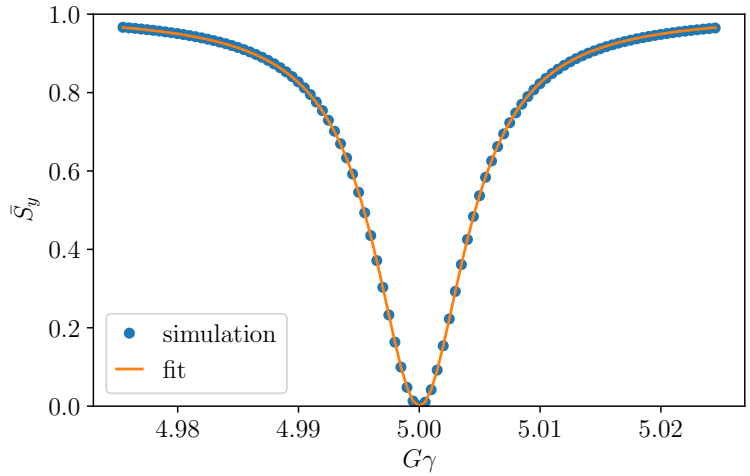

Figure B.18: Static depolarization of helions at $|G\gamma| = 5$, ϵ_K=0.004492.

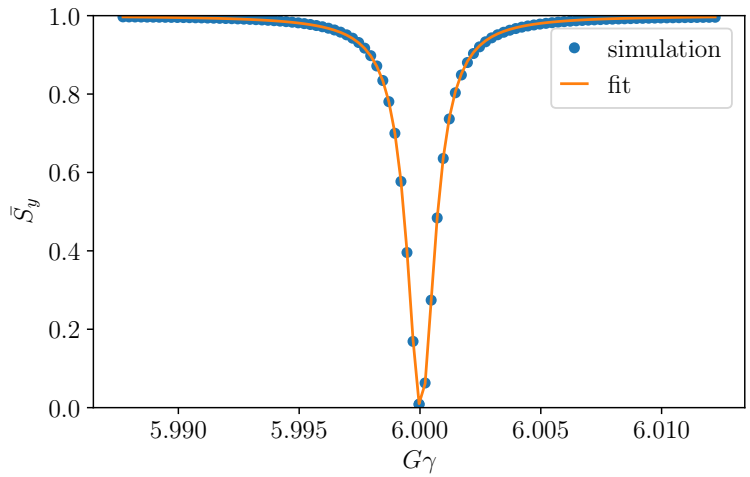

Figure B.19: Static depolarization of helions at $|G\gamma| = 6$, ϵ_K=0.000716.

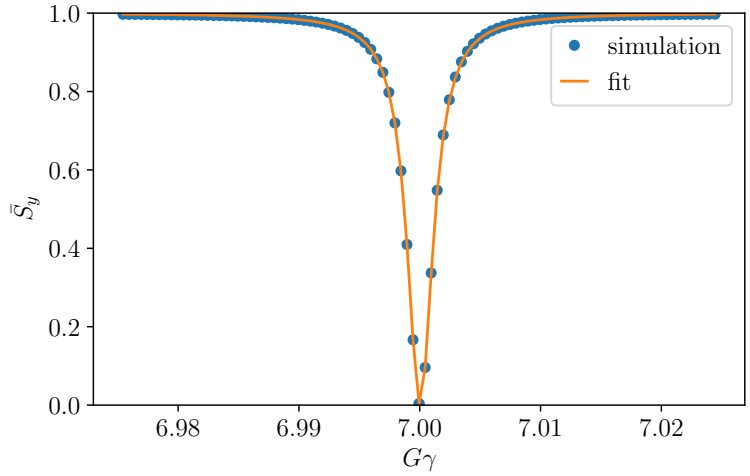

Figure B.20: Static depolarization of helions at $|G\gamma| = 7$, ϵ_K=0.001158.

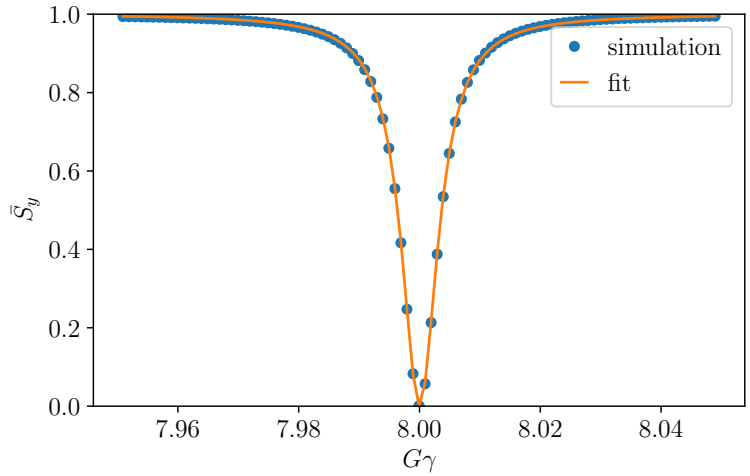

Figure B.21: Static depolarization of helions at $|G\gamma| = 8$, ϵ_K=0.003834.

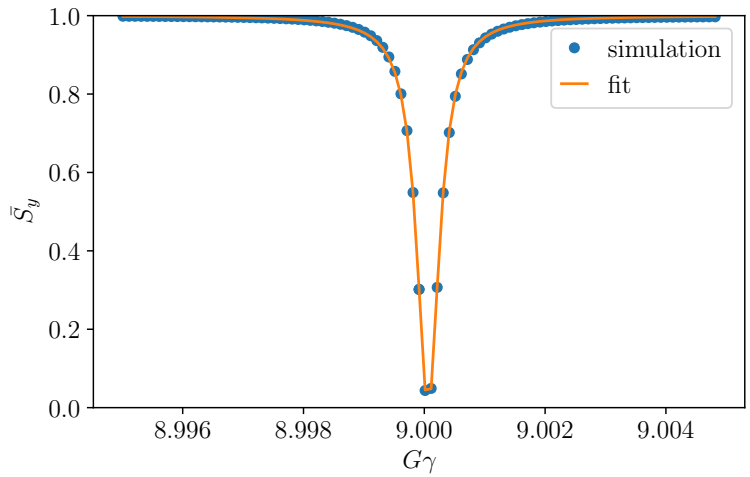

Figure B.22: Static depolarization of helions at $|G\gamma| = 9$, ϵ_K=0.000239.

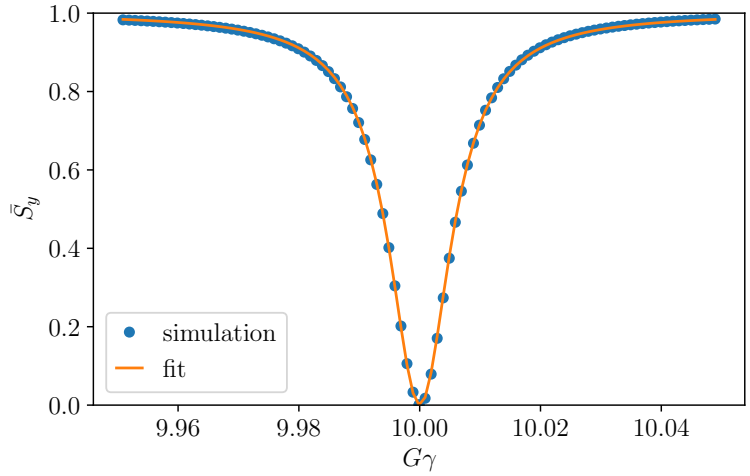

Figure B.23: Static depolarization of helions at $|G\gamma| = 10$, ϵ_K=0.006252.

B.1.4.2 Froissart-Stora

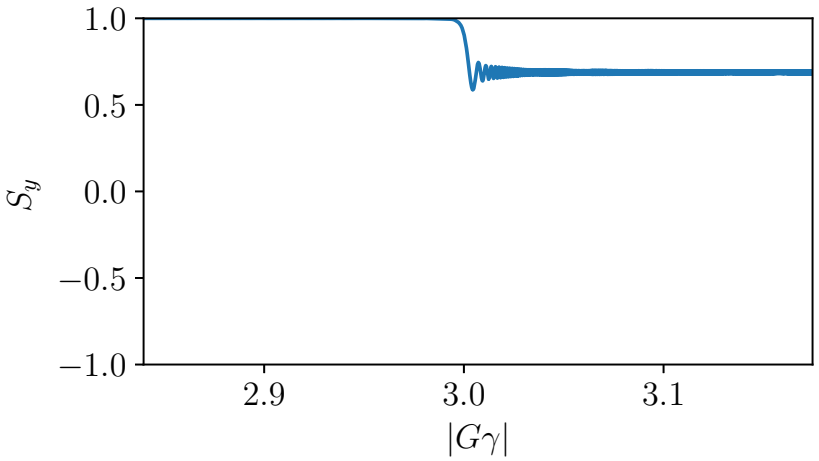

Figure B.24: Protons crossing the $|G\gamma| = 3$ resonance, $P_f = 69.55$.

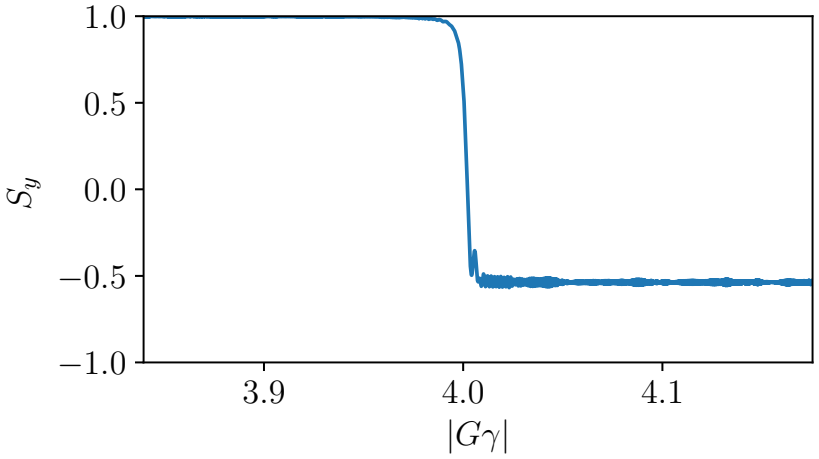

Figure B.25: Protons crossing the $|G\gamma| = 4$ resonance, $P_f = -53.50$.

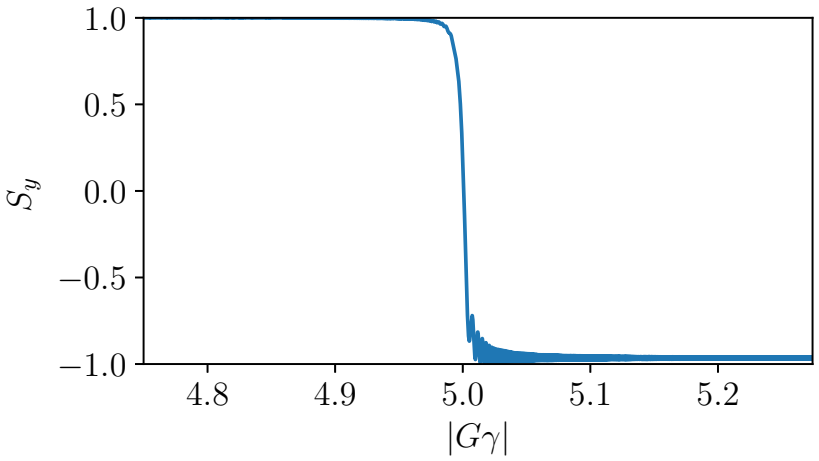

Figure B.26: Helions crossing the $|G\gamma| = 5$ resonance, $P_f = -96.86$.

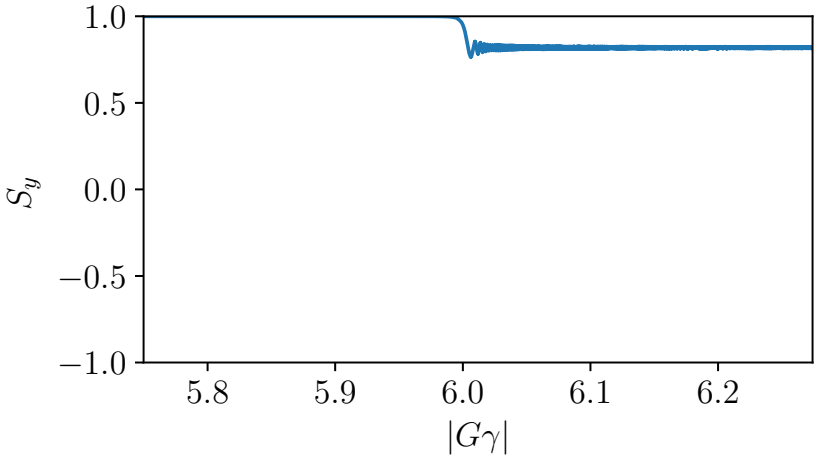

Figure B.27: Helions crossing the $|G\gamma| = 6$ resonance, $P_f = 81.49$.

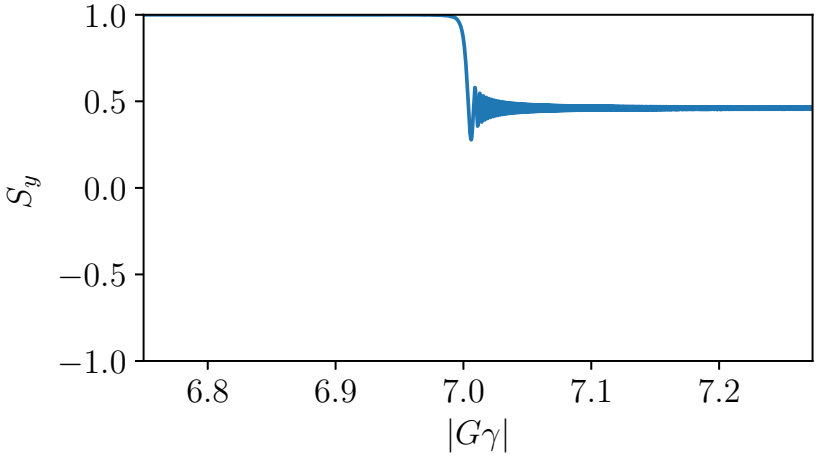

Figure B.28: Helions crossing the $|G\gamma| = 7$ resonance, $P_f = 45.94$.

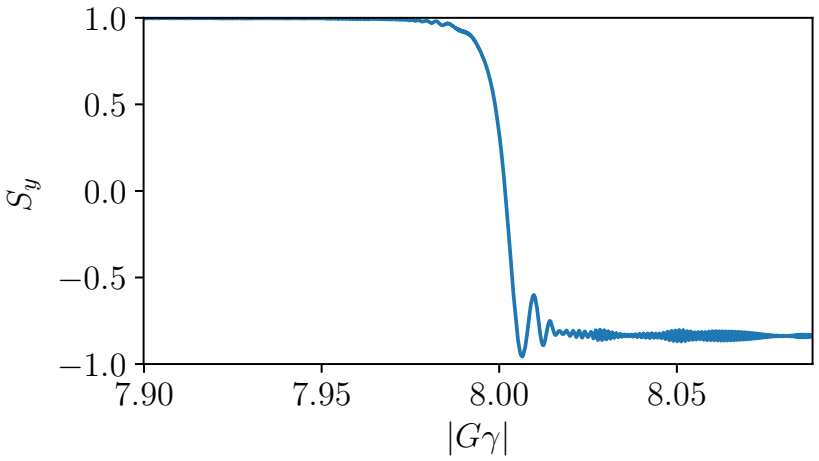

Figure B.29: Helions crossing the $|G\gamma| = 8$ resonance, $P_f = -83.36$.

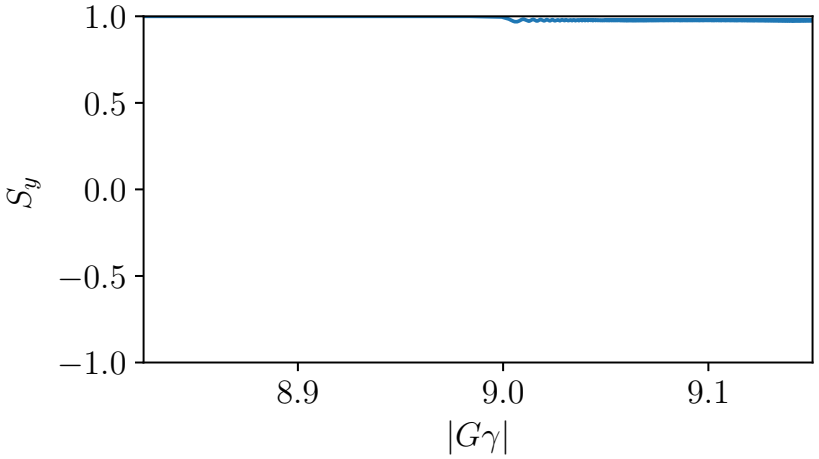

Figure B.30: Helions crossing the $|G\gamma| = 9$ resonance, $P_f = 97.91$.

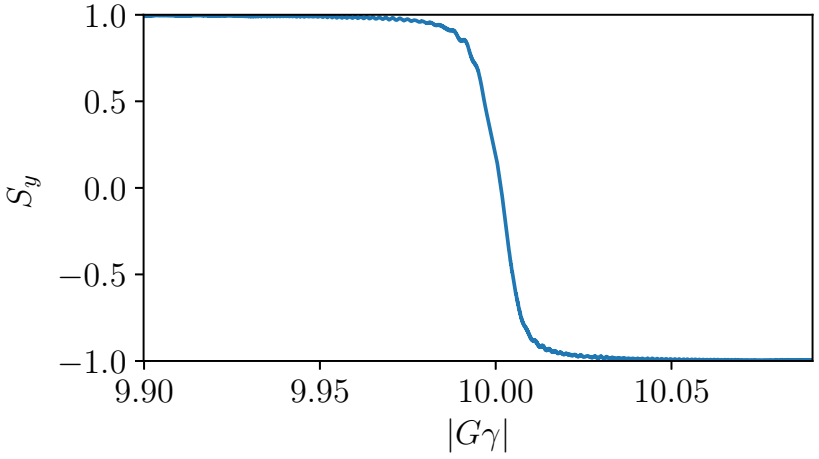

Figure B.31: Helions crossing the $|G\gamma| = 10$ resonance, $P_f = -99.42$.

B.1.4.3 With Harmonics

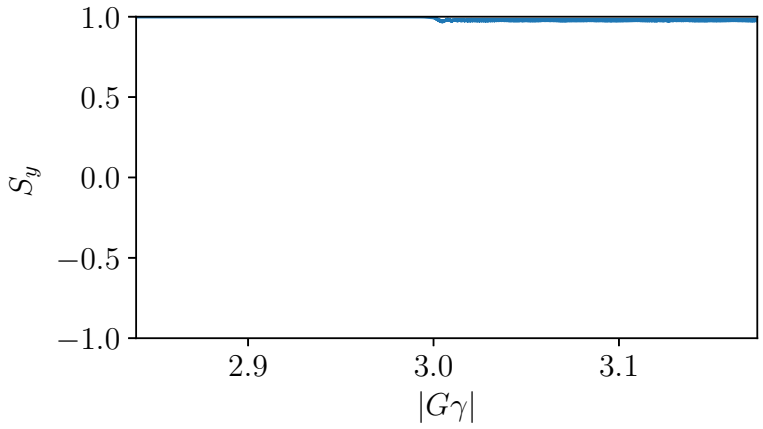

Figure B.32: Protons crossing the $|G\gamma| = 3$ resonance. Harmonic corrector family strengths found in Tab. 2.7.

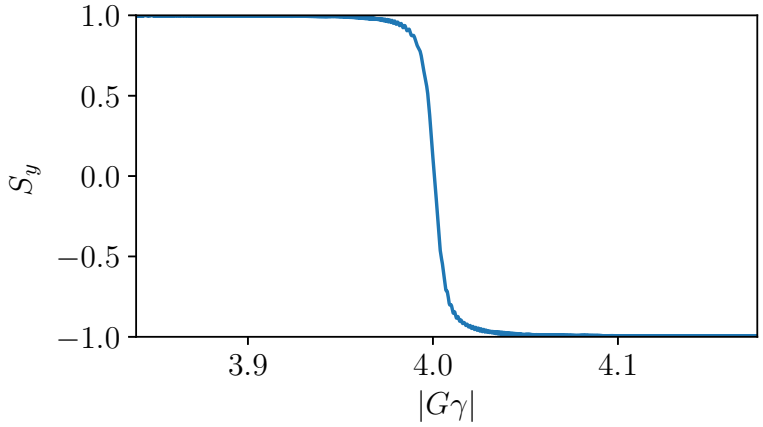

Figure B.33: Protons crossing the $|G\gamma| = 4$ resonance. Harmonic corrector family strengths found in Tab. 2.7.

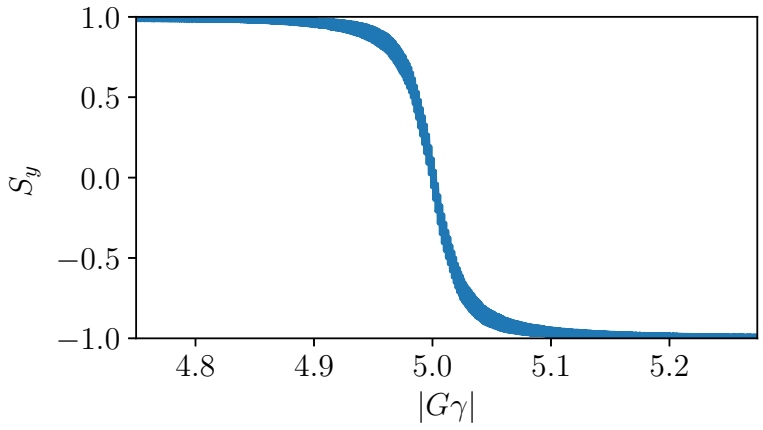

Figure B.34: Helions crossing the $|G\gamma| = 5$ resonance. Harmonic corrector family strengths found in Tab. 2.7.

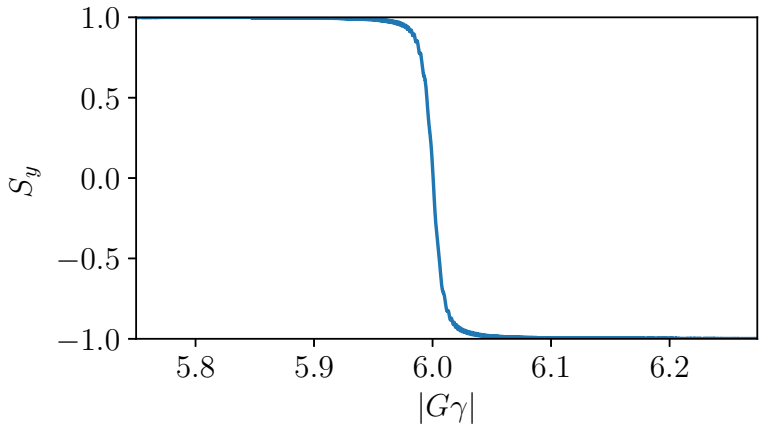

Figure B.35: Helions crossing the $|G\gamma| = 6$ resonance. Harmonic corrector family strengths found in Tab. 2.7.

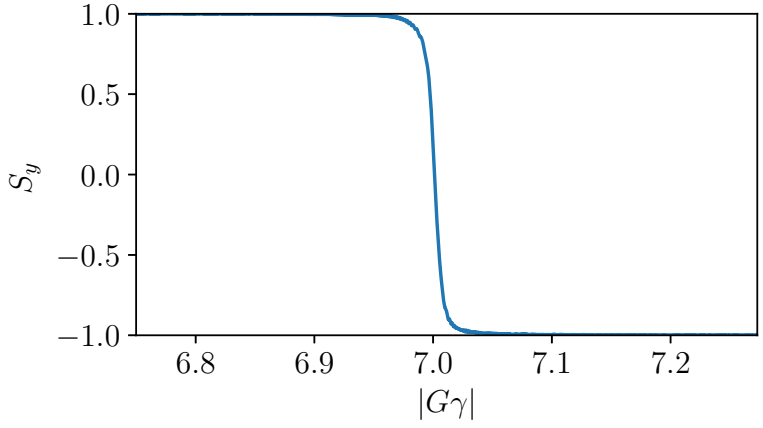

Figure B.36: Helions crossing the $|G\gamma| = 7$ resonance. Harmonic corrector family strengths found in Tab. 2.7.

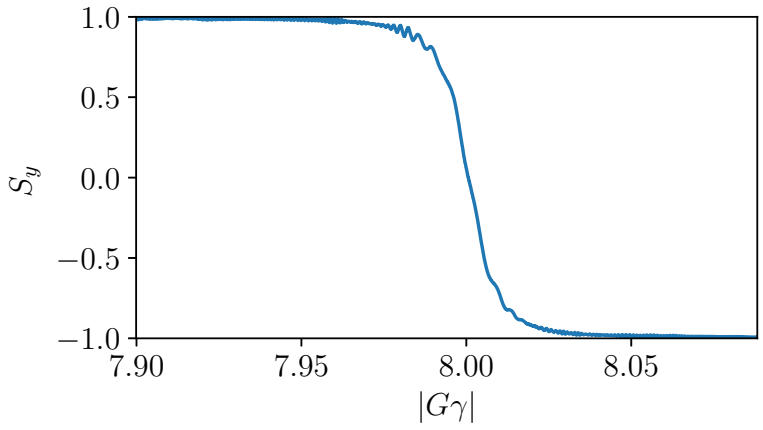

Figure B.37: Helions crossing the $|G\gamma| = 8$ resonance. Harmonic corrector family strengths found in Tab. 2.7.

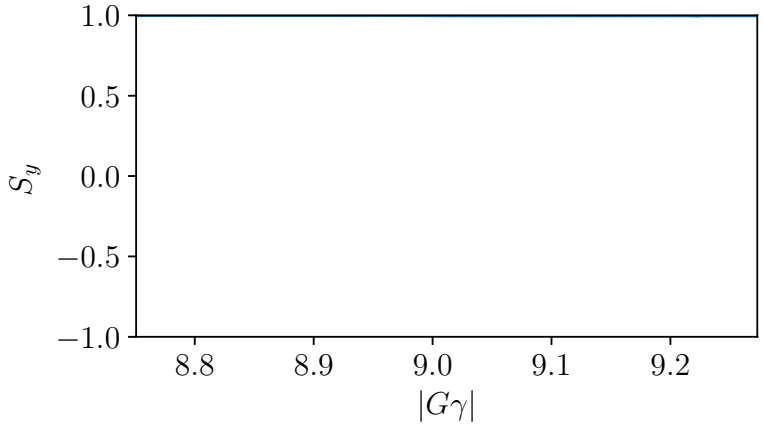

Figure B.38: Helions crossing the $|G\gamma| = 9$ resonance. Harmonic corrector family strengths found in Tab. 2.7.

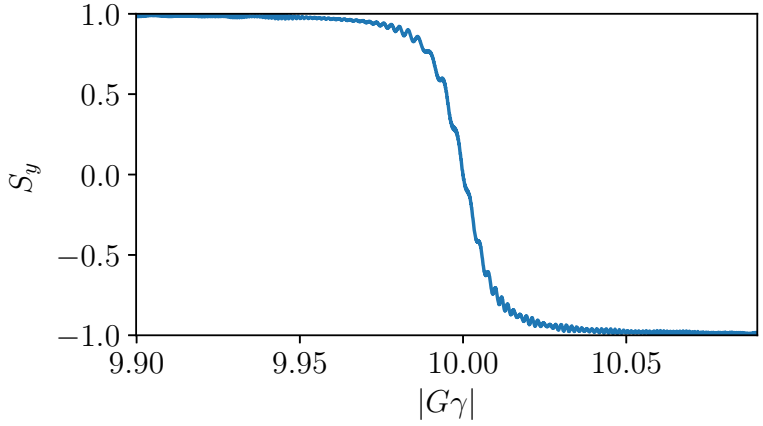

Figure B.39: Helions crossing the $|G\gamma| = 10$ resonance. Harmonic corrector family strengths found in Tab. 2.7.

Appendix C

Appendix III

C.1 Résumé en français

C.1.1 Reśumé général

Les collisions d'hélions polarisés font partie des futurs programmes de physique de l'EIC [1, 2]. L'hélion fournit un neutron polarisé lié à une paire de protons non polarisés. Cet état de spin facilite les collisions de neutrons polarisés pour permettre une étude plus approfondie de la contribution de spin des quarks au moment angulaire total du nucléon. Avec un moment magnétique anomal 2,34 fois plus grand que celui des protons, les hélions rencontreront beaucoup plus de résonances dépolarisantes à mesure qu'ils sont accélérés jusqu'à l'énergie de collision. Pour maximiser la transmission de polarisation à travers les injecteurs de RHIC, il est souhaitable d'extraire les hélions du Booster AGS à $|G\gamma| = 10.5$, évitant ainsi la résonance dépolarisante $|G\gamma| = 0 + \nu_y$ dans l'AGS et minimisant les perturbations optiques qui resultent de la présence de deux serpents partiels dans l'AGS.

L'extraction à $|G\gamma| = 10.5$ causera la traversée les résonances d'imperfection $|G\gamma|$=5, 6, 7, 8, 9, et 10, et des résonances intrinsèques $|G\gamma| = 12 - \nu_y$ et $|G\gamma| = 6 + \nu_y$. Un dipôle AC a été installé dans le Booster AGS pour induire un renversement du spin ("spin-flipping") à travers les deux résonances intrinsèques. Un dipôle AC augmente la force des résonances intrinsèques en induisant des oscillations verticales bêtatron qui provoquent une grande excursion verticale du paquet à travers les champs horizontaux des

quadripôles. Une étude expérimentale avec un faisceau d'Au a confirmé que l'ouverture disponible est suffisante pour accueillir ces oscillations bêtatron verticales de grande amplitude.

Des simulations d'hélions traversant les résonances susmentionnées ont été effectuées et montrent l'efficacité d'un dipôle AC pour exciter le spin-flipping dans le Booster. En raison de l'accélération rapide du Booster, la fréquence du dipôle AC variera jusqu'à 0.0028 (en unités de la fréquence de révolution, ω_0) au cours d'un cycle de dipôle AC, ce qui change l'amplitude de ces oscillations bêtatron au cours du cycle. Grâce à la simulation, il est montré que l'amplitude variable du mouvement bêtatron ne diminue pas l'efficacité de spin-flip du dipôle AC. Les sextupôles sont utilisés pour contrôler la chromaticité, tandis que l'harmonique 2 de la RF est utilisé pour contrôler la longueur du paquet et pour réduire la dispersion en moment.

Les protons polarisés peuvent être utilisés pour traverser une résonance intrinsèque qui impose des contraintes similaires à celles des hélions, permettant ainsi une expérience pratique de preuve de principe pour le dipôle AC Booster AGS pendant la construction de la source d'hélions polarisés. Des études de dynamique de faisceau ont été réalisées avec des protons non polarisés et ont montré un fort accord avec la théorie et avec les simulations. Ces études ont également montré que les protons pouvaient être entraînés à l'amplitude maximale autorisée par l'amplificateur de puissance sans générer de perte de faisceau avec une séparation nominale entre les fréquences du dipôle AC et du mouvement bêtatron, et n'entraînaient aucune dilution de l'émittance.

Les résultats expérimentaux de protons polarisés traversant $|G\gamma| = 0 + \nu_y$ ont montré que la force de la résonance correspond à celle du modèle numérique. En raison de l'utilisation des sextupôles à l'extraction, l'amplitude cohérente des oscillations des protons a été réduite. Cette amplitude réduite nécessitait une réduction verticale de la taille du faisceau pour atteindre un basculement de spin complet à travers la résonance. Le modèle a été ajusté pour refléter l'expérience et a montré un bon accord. Compte tenu des résultats de l'expérience, le modèle Booster est validé et ainsi le dipôle AC parametra de basculer le spin des hélions à travers les deux résonances intrinsèques.

C.1.2 Introduction

Les hélions polarisés font partie du futur programme de physique du spin au collisionneur électron-ion (EIC). Son schéma de polarisation comprend les collisions de neutrons polarisés au niveau des détecteurs EIC. Les asymétries entre les collisions de neutrons polarisés et de protons polarisés peuvent fournir plus de détails sur la contribution des quarks de valence au moment angulaire total de la particule.

L'EIC doit être construit sur le complexe RHIC existant. Celui-ci se compose de deux synchrotrons injecteurs (le synchrotron à gradient alterné (AGS) et le Booster AGS), de deux pré-injecteurs (la source d'ions à faisceau d'électrons (EBIS) et le LINAC). Les hélions polarisés proviendront d'une EBIS, quand les protons polarisés proviennent du LINAC. L'optimisation de la transmission de polarisation à travers la chaîne d'accélérateurs est impérative pour maximiser la figure de mérite (FOM).

Une introduction à la physique des accélérateurs pertinente pour le complexe d'accélérateurs RHIC est donnée. Cela inclut des paramètres clés tels que les nombres d'onde bêtatron, les fonctions bêta et de dispersion et la chromaticité. Les effets d'erreurs de champ dipolaire résultant de désalignements quadripolaires sont discutées. Ces désalignements excitent les harmoniques d'orbite qui peuvent être corrigées via la méthode de correction d'orbite harmonique. L'ouverture dynamique (DA) est l'amplitude maximale qui peut survivre un nombre de tours donné. L'admittance est l'équivalent du DA mais avec l'inclusion d'ouvertures physiques. Un dipôle AC entraîne des oscillations bêtatron de grande amplitude avec un champ magnétique oscillant qui est en phase avec le mouvement bêtatron des particules. La dynamique longitudinale régit les oscillations longitudinales des particules sous l'influence de la focalisation longitudinale des cavités radiofréquences.

La dynamique de spin en ce qui concerne les injecteurs RHIC est discutée. Les résonances d'imperfection proviennent d'une erreur d'orbite fermée verticale principalement causée par des désalignements quadripolaires. Ce type de résonance de spin dépolarisante se produit lorsque le nombre d'onde de spin ("spin tune") est égal à un entier. Les résonances intrinsèques sont causées par un mouvement bêtatron non nul et se produisent lorsque le spin tune est en phase avec le mouvement bêtatron. Les fortes résonances in-

trinsèques dépendent en plus de la superpériodicité du synchrotron. Dans l'AGS, l'étude de la dynamique de spin en présence de deux serpents partiels montre que la direction de rotation stable n'est verticale que lorsque $|G\gamma| = 3n + 1.5$ en raison de la séparation des deux serpents dans l'anneau et de leurs angles de rotation du spin. La méthode de saut rapide de nombre d'onde ("tune jump") utilise des aimants quadripolaires à pulsation rapide pour induire un changement rapide de l'emplacement de la résonance lorsqu'elle est traversée. Un dipôle AC est utilisé pour les hélions et les protons pour traverser les résonances intrinsèques. Les oscillations bêtatron de haute amplitude induites par le dipôle AC font que toutes les particules échantillonnent les champs hautement dépolarisants des quadripôles, induisant ainsi un spin-flip complet.

C.1.3 Modêl du Booster et Simulations

Un modèle du Booster a été développé dns le code d'optique Zgoubi, qui concorde étroitement avec les résultats du modèle "MADx" du Booster. Le modéle a ensuite été étendu à PyZgoubi, ce qui a permis une plus grande flexibilité. La force des résonances intrinsèques et des résonances d'imperfection est calculée en utilisant un certain nombre de méthodes et en utilisant à la fois les modèles Zgoubi et MADx.

Des simulations incluant un dipôle AC pour la traversée des résonances intrinsèques d'hélion, montrent qu'il y a une ouverture suffisante pour s'adapter aux oscillations de haute amplitude. La force maximale requise pour faire basculer les spins est de 20,5 $\mathrm{G \cdot m}$ et la force maximale du dipôle AC est de 25 $\mathrm{G \cdot m}$. Les simulations sont effectuées avec un nombre d'onde d'oscillation par le dipôle AC correspondant à 250 kHz.

La méthode de correction harmonique est implémentée dans le modèle Zgoubi et utilisée pour les simulations de résonances d'imperfection. Celles-ci sont effectuées initialement pour les protons, et les résultats de simulation correspondent étroitement aux données expérimentales. Elle est ensuite étendue aux hélion et montre qu'il y a suffisamment de courant disponible dans les alimentations des correcteurs d'orbite jusqu'à l'énergie d'extraction du Booster la plus élevée. Ces simulations montrent également que la traversée de certaines résonances peut être affectée par des harmoniques d'ordre

inférieur. Les simulations de dipôle AC montrent une interférence entre la résonance intrinsèque renforée (par le dipôle AC) et les résonances d'imperfection fortes voisines.

Des simulations de l'ouverture dynamique (DA) et de l'admittance de l'AGS à l'injection montrent que les défauts optiques dûs aux serpents sibériens partiels réduisent considérablement l'ouverture disponible. L'augmentation de l'énergie d'injection de l'AGS fournit plus d'ouverture, aux nombre d'onde bêtatron souhaités. A l'énergie d'extraction maximale souhaitée du Booster, il y a une amélioration de l'admittance d'un facteur quatre et une réduction d'un facteur 6 des défauts optiques dûs aux deux serpents sibériens, par rapport à l'énergie la plus faible.

C.1.4 Montage exprimental

L'ouverture verticale limite du Booster correspond à la largeur de la chambre à vide principale mesurée à 3,5 cm. Ceci a été mesuré lors d'une étude utilisant un faisceau d'Au. L'ouverture du dipôle AC (qui est placé à l'intérieur de la chambre à vide) est conçue pour être de 8,6 cm à la fois horizontalement et verticalement, ainsi supérieure à l'ouverture limite de la machine. Le circuit résonant est a une fréquence maximale de 250 kHz, qui est la fréquence maximale acceptée par l'amplificateur de puissance.

La minimisation de l'étalement du nombre d'onde bêtatron est essentielle car elle entraîne une réduction corrélée de la plage d'amplitudes cohérentes verticales des particules telles que générées par le dipôle AC. Ceci est fait en utilisant des sextupôles de correction de chromaticité. Cela peut également être fait par addition d'harmoniques 2 de la RF pour allonger un paquet, ce qui réduit à son tour l'étendue totale du paquet. Les simulations montrent que la réduction de la chromaticité à près de zéro et l'augmentation de la longueur du paquet réduisent l'intensité du champ nécessaire pour induire un retournement de spin. En raison du changement rapide de fréquence de révolution du Booster, le nombre d'onde du dipôle AC changera jusqu'à 25%, ce qui renforce l'importance d'atténuer la dispersion de nombre d'onde.

Une suite de logiciels propriétaires est utilisée pour contrôler les nombreux aspects de la machine et est décrite. Ces applications incluent : l'application BoosterMainMagnet,

qui est utilisée pour concevoir la fonction actuelle de l'alimentation électrique de l'aimant principal ; boosterOrbitControl, qui est utilisé pour manipuler les bumps d'orbite fermée et les bumps harmoniques ; et l'application Booster AC Dipole/Tune Meter, qui contrôle le nouveau dipôle AC.

C.1.5 Résultats Expérimentaux

Des études de dynamique de faisceau ont été réalisées à l'aide du dipôle AC. Un balayage du paramètre de proximité de la résonance du dipôle AC (δ_m), pour deux valeurs différentes de la chromaticité, a montré qu'avoir une chromaticité proche de zéro améliorait considérablement les conditions de fonctionnement du dipôle AC. Une analyse du paramètre de proximité a montré un fort accord avec les prédictions. De même, l'analyse de la force du dipôle AC a également confirmé nos attentes. Ces études n'ont également montré aucune croissance de l'émittance.

Les protons traversent la résonance $|G\gamma| = 0+\nu_y$ et voient les spin basculer complètement à travers la résonance. Plusieurs facteurs ont affecté les performances du dipôle AC : les bumps d'extraction et la synchro Booster à AGS (BtA). Une brève étude a montré que le fait d'avoir un paquet plus court augmentait la force requise pour induire un spin flip. C'est le résultat de la manipulation de la distribution longitudinale. Vers la fin de l'impulsion du dipôle AC, les bumps d'extraction ont commencé à augmenter. Ce grand changement dans la position horizontale a entraîné une grande erreur d'orbite fermée horizontale et une réduction de δ_m par l'alimentation des sextupôles. La réduction de δ_m a entraîné une décélération non adiabatique des oscillations cohérentes. Ceci a été résolu avec un balayage de synchronisation et un ajustement de synchronisation pour l'impulsion dipolaire AC et les bumps d'extraction. Le balayage temporel a permis de traverser une fenêtre de 0.8 ms où un spin-flip peut se produire.

En raison de contraintes de temps, le paquet est raccourci pour réduire la dispersion du nombre d'onde. Cela réduit l'efficacité du spin-flip et dans ce cas, un spin-flip complet n'a pas pu être réalisé dans la plage de fonctionnement du dipôle AC.

En raison du fonctionnement du dipôle AC près de l'extraction, la synchronisation

BtA ne peut être évitée. Cela maintient une fréquence fixe à des moments spécifiques du cycle du Booster. L'impulsion du dipôle AC provoque une modification de la longueur du trajet qui amènera les systèmes RF à modifier le rayon afin de maintenir la fréquence RF spécifiée. Ce changement radial a provoqué un changement de nombre d'onde bêtatron vertical qui a réduit l'amplitude cohérente verticale maximale réalisable. Pour essayer de séparer l'impulsion dipolaire AC de la synchro, l'extraction est déplacée au-dessus de $G\gamma$=5 ce qui impliquait de traverser la résonance d'imperfection $G\gamma$=5. Cette étude a été brève et a montré que les corrections utilisées étaient loin d'être optimales.

C.1.6 Conclusion

Les hélions dans le Booster voient un certain nombre de résonances dépolarisantes qui doivent être compensées pour assurer une transmission de polarisation élevée à l'EIC, car ils sont accélérés jusqu'à l'extraction correspondant à $|G\gamma| = 10,5$. Cette énergie d'extraction plus élevée permet également d'éviter l'AGS $|G\gamma| = 0 + \nu_y = 8.9$. Les simulations d'ouverture dynamique à $|G\gamma| = 10,5$ et $|G\gamma| = 7,5$ montrent que l'énergie d'injection AGS plus élevée a une admittance beaucoup plus grande en raison de la réduction des défauts optiques dûs aux serpents sibériens AGS [55]. Cette admission améliorée permettra à la fois aux nombres d'onde verticaux et horizontaux d'être placés dans l'espace de bande interdite de spin lors de l'injection.

Les simulations de balayages harmoniques aux résonances d'imperfection $|G\gamma|$ =3 et 4 pour les protons sont conformes aux données expérimentales. La méthode utilisée a été étendue aux hélions pour leurs six résonances d'imperfection. Ces simulations montrent qu'il existe un courant correcteur suffisant pour corriger ou exacerber chaque harmonique d'orbite [18, 56] pour chaque resonancee.

L'ouverture du Booster a été mesurée et confirmée comme étant la valeur documentée. Pour les hélions traversant les deux résonances intrinsèques, les simulations montrent qu'un basculement de spin complet se produira avec des oscillations cohérentes qui se situent dans les limites du tube de faisceau [16, 17, 57]. Un dipôle AC a été conçu et installé dans le Booster pour ces deux résonances [58, 59]. Des simulations de dipôles

AC ont montré que le contrôle de la chromaticité était impératif pour maintenir ces oscillations cohérentes sans perdre de particules.

Ces simulations montrent que le dipôle AC peut faire passer des protons à travers la résonance $|G\gamma| = 0 + \nu_y$ dans Booster. Le critère pour un basculement de spin complet des protons traversant $|G\gamma| = 0 + \nu_y$ est similaire à celui des hélions à $|G\gamma| = 12 - \nu_y$, fournissant une preuve de principe expérimentale. Ces simulations ont été faites avec une fréquence de modulation fixe du dipôle AC qui mime le mode de fonctionnement le plus réaliste. Il a été déterminé que le balayage du nombre d'onde qui en résulte ne dilue pas l'efficacité de spin-flip.

Les mesures ont montré un fort accord entre la théorie et la simulation. Ces mesures incluent un balayage de δ_m et $B_m l$. Les analyses de la perte de faisceau en fonction du paramètre de proximité de résonance ont montré qu'une chromaticité réduite minimisait le perte de particules en minimisant la dispersion de δ_m. Cette période de mesures a également montré que la croissance de l'émittance était minime lors du fonctionnement du dipôle AC.

L'expérience réalisée avec des protons traversant la résonance $|G\gamma| = 0 + \nu_y$ a montré que le dipôle AC était capable de réaliser un spin-flip complet. En raison du fonctionnement du dipôle AC près de l'extraction, deux processus ont interféré avec son fonctionnement : les bumps d'extraction et la synchronisation Booster to AGS. L'accélération des bumps d'extraction a entraîné une décélération non adiabatique de l'impulsion dipolaire AC, ce qui a entraîné la poursuite des oscillations cohérentes. Après un balayage temporel du début de l'impulsion dipolaire AC, l'impulsion dipolaire AC a été séparée des bumps d'extraction, éliminant l'interférence. Les oscillations de grande amplitude du dipôle AC ont provoqué une modification de la longueur du trajet, ce qui a amené le système RF à modifier le rayon afin de maintenir la fréquence correcte entre Booster et AGS. Ce changement radial a provoqué des excursions horizontales dans les sextupôles où l'alimentation a provoqué un décalage de ν_y, une augmentation correspondante de δ_m et une réduction de Y_{coh}. En raison de la réduction de Y_{coh}, le faisceau a d être collimaté pour réduire ε_y afin qu'un spin-flip puisse se produire. La valeur calculée de ϵ_K à

partir de ces mesures correspondait aux attentes de la théorie et de la simulation. Le modèle a été modifié pour refléter ces effets et l'accord entre la simulation et les données expérimentales a été rétabli.

Sur la base des résultats du dipôle AC des protons traversant la résonance $|G\gamma| = 0 + \nu_y$, les hélions polarisés seront capables de basculer à travers les résonances $|G\gamma| = 12 - \nu_y$ et $|G\gamma| = 6 + \nu_y$. Malgré la résonance $|G\gamma| = 6 + \nu_y = 10.174$, une petite réduction du taux de rampe permettrait à l'impulsion dipolaire AC d'être complètement séparée de la synchro. Des études utilisant des protons polarisés peuvent continuer à avoir lieu pour séparer l'impulsion dipolaire AC de la synchro et traverser la résonance d'imperfection d'ordre supérieur, ce qui favorisera le développement futur en hélions polarisés. L'installation de le source d'hélions polarises étant désormais prévue pour l'arrêt de 2022, des études sur l'hélion polarisé pourront bientôt avoir lieu dans les injecteurs en vue de l'EIC.

Bibliography

[1] E. Aschenauer et al. Opportunities for Polarized He-3 in RHIC and EIC. In *Proceedings of RIKEN BNL Research Center Workshop*, 2011. URL `https://www.bnl.gov/isd/documents/76833.pdf`.

[2] W. Fischer et al. eRHIC in electron-ion operation. In *10th International Particle Accelerator Conference (IPAC19) Conference. Melbourne, Australia*, 2019. URL `https://www.osti.gov/servlets/purl/1515151`.

[3] J. Ashman, B. Badelek, G. Baum, J. Beaufays, C.P. Bee, C. Benchouk, I.G. Bird, S.C. Brown, M.C. Caputo, H.W.K. Cheung, J. Chima, J. Ciborowski, R.W. Clifft, G. Coignet, F. Combley, G. Court, G. D'Agostini, J. Drees, M. Dren, N. Dyce, A.W. Edwards, M. Edwards, T. Ernst, M.I. Ferrero, D. Francis, E. Gabathuler, J. Gajewski, R. Gamet, V. Gibson, J. Gillies, P. Graftstrm, K. Hamacher, D. Von Harrach, P. Hayman, J.R. Holt, V.W. Hughes, A. Jacholkowska, T. Jones, E.M. Kabuss, B. Korzen, U. Krner, S. Kullander, U. Landgraf, D. Lanske, F. Lettenstrm, T. Lindqvist, J. Loken, M. Matthews, Y. Mizuno, K. Mnig, F. Montanet, J. Nassalski, T. Niinikoski, P.R. Norton, G. Oakham, R.F. Oppenheim, A.M. Osborne, V. Papavassiliou, N. Pavel, C. Peroni, H. Peschel, R. Piegaia, B. Pietrzyk, U. Pietrzyk, B. Povh, P. Renton, J.M. Rieubland, A. Rijllart, K. Rith, E. Rondio, L. Ropelewski, D. Salmon, A. Sandacz, T. Schrder, K.P. Schler, K. Schultze, T.-A. Shibata, T. Sloan, A. Staiano, H. Stier, J. Stock, G.N. Taylor, J.C. Thompson, T. Walcher, S. Wheeler, W.S.C. Williams, S.J. Wimpenny, R. Windmolders, W.J. Womersley, and K. Ziemons. A measurement of the spin asymmetry and determination of the structure function g1 in deep inelastic muon-proton scat-

tering. *Physics Letters B*, 206(2):364–370, 1988. ISSN 0370-2693. doi: https://doi.org/10.1016/0370-2693(88)91523-7. URL https://www.sciencedirect.com/science/article/pii/0370269388915237.

[4] A. Landé. Über den anomalen Zeemaneffekt (Teil I). *Zeitschrift fur Physik*, 5: 231–241, July 1921. doi: 10.1007/BF01335014.

[5] Walther Gerlach and Otto Stern. Der experimentelle nachweis der richtungsquantelung im magnetfeld. *Zeitschrift für Physik*, 9(1):349–352, Dec 1922. ISSN 0044-3328. doi: 10.1007/BF01326983. URL https://doi.org/10.1007/BF01326983.

[6] E. D. Cummins. Electron spin and its history. *Annual Review of Nuclear and Particle Science*, 62:133–157, November 2012.

[7] Ming Xiong Liu. Nucleon Structure Physics by Proton-Proton Collisions. In *8th International Conference on Quarks and Nuclear Physics (QNP2018)*, page 011009, January 2019. doi: 10.7566/JPSCP.26.011009.

[8] A. N. Zelenski, V. I. Davydenko, G. Dutto, A. A. Hamian, V. Klenov, C. D. P. Levy, I. I. Morozov, P. W. Schmor, W. T. H. van Oers, and G. W. Wight. Oppis development for precision experiments and high energy colliders. *AIP Conference Proceedings*, 421(1):372–380, 1998. doi: 10.1063/1.54990. URL https://aip.scitation.org/doi/abs/10.1063/1.54990.

[9] A. Chao et al. *Handbook of Accelerator Physics and Engineering*. World Scientific Publishing Company Incorporated, 2006.

[10] J. Collins et al. In *Proceedings of the Polarized Collider Workshop, AIP Conference Proceedings No. 223*NY, USA, 1990.

[11] A. Kponou, A. Zelenski, S. Kokhanovski, and V. Zubets. Sona transition studies in the rhic oppis. *AIP Conference Proceedings*, 980(1):241–247, 2008. doi: 10.1063/1.2888092. URL https://aip.scitation.org/doi/abs/10.1063/1.2888092.

[12] J. Maxwell, C. Epstein, R. Milner, J. Alessi, E. Beebe, A. Pikin, J. Ritter, and A. Zelenski. Development of a polarized helium-3 source for rhic and erhic. *International Journal of Modern Physics: Conference Series*, 40:1660102, 2016. doi: 10.1142/S2010194516601022. URL https://doi.org/10.1142/S2010194516601022.

[13] J.D. Maxwell, J. Alessi, G. Atoian, E. Beebe, C.S. Epstein, R.G. Milner, M. Musgrave, A. Pikin, J. Ritter, and A. Zelenski. Enhanced polarization of low pressure 3he through metastability exchange optical pumping at high field. *Nuclear Instruments and Methods in Physics Research Section A: Accelerators, Spectrometers, Detectors and Associated Equipment*, 2019. ISSN 0168-9002. doi: https://doi.org/10.1016/j.nima.2019.02.019. URL http://www.sciencedirect.com/science/article/pii/S0168900219301949.

[14] G. Zschornacka et al. Electron beam ion sources, 2014. URL https://arxiv.org/pdf/1410.8014.pdf.

[15] H.C. Hseuh. The ags booster vacuum systems. *Vacuum*, 41(7):1903 – 1906, 1990. ISSN 0042-207X. doi: https://doi.org/10.1016/0042-207X(90)94127-C. URL http://www.sciencedirect.com/science/article/pii/0042207X9094127C.

[16] K. Hock et al. *Intrinsic Resonances and AC-Dipole simulations of ^{3}He in the AGS-Booster*. C-AD Tech Note 597, 2017. URL https://www.osti.gov/servlets/purl/1436282.

[17] K. Hock et al. *Overcoming proton and ^{3}He Intrinsic Resonances in the AGS Booster with an ac dipole*. C-AD Tech Note 601, 2018. URL www.osti.gov/servlets/purl/1469789.

[18] K. Hock et al. *Imperfection resonance crossing in the AGS Booster*. C-AD Tech Note 633, 2020. URL https://www.osti.gov/servlets/purl/1661654.

[19] E.D Courant and H.S Snyder. Theory of the alternating-gradient synchrotron. *Annals of Physics*, 3(1):1 – 48, 1958. ISSN 0003-4916. doi: https://doi.org/10.1016/

0003-4916(58)90012-5. URL http://www.sciencedirect.com/science/article/pii/0003491658900125.

[20] E.D. Courant et al. *Acceleration of Polarized Protons in Circular Accelerators*. BNL Note 51270, 1980. URL https://www.osti.gov/servlets/purl/7034691.

[21] J. J. Aubert, U. Becker, P. J. Biggs, J. Burger, M. Chen, G. Everhart, P. Goldhagen, J. Leong, T. McCorriston, T. G. Rhoades, M. Rohde, Samuel C. C. Ting, Sau Lan Wu, and Y. Y. Lee. Experimental observation of a heavy particle j. *Phys. Rev. Lett.*, 33:1404–1406, Dec 1974. doi: 10.1103/PhysRevLett.33.1404. URL https://link.aps.org/doi/10.1103/PhysRevLett.33.1404.

[22] G. Danby, J-M. Gaillard, K. Goulianos, L. M. Lederman, N. Mistry, M. Schwartz, and J. Steinberger. Observation of high-energy neutrino reactions and the existence of two kinds of neutrinos. *Phys. Rev. Lett.*, 9:36–44, Jul 1962. doi: 10.1103/PhysRevLett.9.36. URL https://link.aps.org/doi/10.1103/PhysRevLett.9.36.

[23] J. H. Christenson, J. W. Cronin, V. L. Fitch, and R. Turlay. Evidence for the 2π decay of the k_2^0 meson. *Phys. Rev. Lett.*, 13:138–140, Jul 1964. doi: 10.1103/PhysRevLett.13.138. URL https://link.aps.org/doi/10.1103/PhysRevLett.13.138.

[24] L. G. Ratner and T. K. Khoe. Acceleration of polarized protons in the zero gradient synchrotron (zgs). *IEEE Transactions on Nuclear Science*, 20(3):217–220, 1973. URL https://accelconf.web.cern.ch/p73/PDF/PAC1973_0217.PDF.

[25] A.D. Krisch. *Gauge Theories, Massive Neutrinos and Proton Decay. Studies in the Natural Sciences*. Springer, Boston, MA, 1981. URL https://lib-extopc.kek.jp/preprints/PDF/1981/8104/8104289.pdf.

[26] F. Z. Khiari et al. Acceleration of polarized protons to 22 GeV/c and the measurement of spin-spin effects in $p_\uparrow + p_\uparrow \rightarrow$p+p. *Phys. Rev. D*, 39:45–85, Jan 1989. doi:

10.1103/PhysRevD.39.45. URL https://link.aps.org/doi/10.1103/PhysRevD.39.45.

[27] T. Roser. Polarized protons at the AGS and high P2 spin effects. In *AIP Conference Proceedings 150*, pages 1148–1152, 1986. URL http://hdl.handle.net/2027.42/87395.

[28] F. Lin. *Towards Full Preservation of Polarization of Proton Beams in AGS*. PhD thesis, Indiana University, December 2007. URL https://www.bnl.gov/userscenter/thesis/past-competitions/2008/files/FLin_Thesis.pdf.

[29] Y. Dutheil. *Spin dynamics modeling in the AGS based on astepwise ray-tracing method*. PhD thesis, University Grenoble-Alpes, April 2015. URL https://www.bnl.gov/isd/documents/94722.pdf.

[30] H. Huang et al. P-Carbon CNI Polarimetry in the AGS and RHIC. In *Proceedings of EPAC08*. Genoa, Italy, 2008. URL https://www.bnl.gov/isd/documents/43150.pdf.

[31] Gerald G. Ohlsen and P.W. Keaton. Techniques for measurement of spin-12 and spin-1 polarization analyzing tensors. *Nuclear Instruments and Methods*, 109(1):41–59, 1973. ISSN 0029-554X. doi: https://doi.org/10.1016/0029-554X(73)90450-3. URL https://www.sciencedirect.com/science/article/pii/0029554X73904503.

[32] J. Tojo et al. Measurement of analyzing power for proton-carbon elastic scattering in the coulomb-nuclear interference region with a 22-gev/c polarized proton beam. *Physical Review Letter*, 89:052302, Jul 2002. doi: 10.1103/PhysRevLett.89.052302. URL https://link.aps.org/doi/10.1103/PhysRevLett.89.052302.

[33] J.D. Jackson. *Classical electrodynamics*. Wiley, New York, NY, 3rd ed. edition, 1999. ISBN 9780471309321. URL http://cdsweb.cern.ch/record/490457.

[34] S. Y. Lee. *Spin Dynamics and Snakes in Synchrotrons*. World Scientific Publishing Company Incorporated, 1997.

[35] S. Y. Lee. *Accelerator Physics*. World Scientific Publishing Company Incorporated, 2012.

[36] M. Bai. *Overcoming the Intrinsic Spin Resonance by Using an RF Dipole*. PhD thesis, Indiana University, 1999. URL https://www.rhichome.bnl.gov/RHIC/Spin/papers/baithesis.pdf.

[37] L. H. Thomas. The calculation of atomic fields. *Mathematical Proceedings of the Cambridge Philosophical Society*, 23(5):542548, 1927. doi: 10.1017/S0305004100011683. URL https://www.equipes.lps.u-psud.fr/Montambaux/histoire-physique/Thomas-1927-Thomas-Fermi.pdf.

[38] L. Michel V. Bargmann and V. L. Telegdi. Precession of the polarization of particles moving in a homogeneous electromagnetic field. *Phys. Rev. Lett.*, 2:435–436, May 1959. doi: 10.1103/PhysRevLett.2.435. URL https://link.aps.org/doi/10.1103/PhysRevLett.2.435.

[39] F. Méot. *Spin Tracking simulations in AGS based on ray-tracing methods - bare lattice, no snakes*. C-AD Tech Note 452, 2009. URL https://www.bnl.gov/isd/documents/77465.pdf.

[40] M. Froissart, R. Stora. Depolarisation d'un faisceau de protons polarises dans un synchrotron. *Nuclear Instruments and Methods*, 7:297-305, 1959. URL https://www.sciencedirect.com/science/article/pii/0029554X60900331?via%3Dihub.

[41] M. Bai et al. *Overcoming the Intrinsic Spin Resonance using Resonance Island created by RF Dipole*. C-AD Spin Note 055, 1997. URL https://technotes.bnl.gov/PDF?publicationId=27713.

[42] F. Méot. *Zgoubi User's Guide*, 2012. URL https://sourceforge.net/p/zgoubi/code/HEAD/tree/trunk/guide/Zgoubi.pdf.

[43] H. Grote. *The MAD-X Program*, 2016. URL http://mad.web.cern.ch/mad/releases/5.02.08/madxuguide.pdf.

[44] K. Brown et al. *A high precision model of Booster Tune Control.* C-AD Tech Note 69, 2002. URL https://technotes.bnl.gov/PDF?publicationId=31923.

[45] E. Bleser. *Booster Short Quadrupole Measurements.* Booster Tech Note 174, 1990. URL https://technotes.bnl.gov/PDF?publicationId=28693.

[46] V. Ranjbar et al. Mapping out the full spin resonance structure of RHIC. In *Proceedings of Particle Accelerator Conference 2001.* Chicago, USA, 2001. URL https://www.osti.gov/servlets/purl/782948.

[47] R. Thern. *Booster Dipole Production Measurements.* Booster Tech Note 190, 1991. URL https://technotes.bnl.gov/PDF?publicationId=28791.

[48] S. Tygier et al. The PyZgoubi Framework and the Simulation of Dynamic Aperture in Fixed-Field Alternating Gradient Accelerators. *Nuclear Instruments and Methods in Physics*, 775:15–26, 2015. URL https://www.sciencedirect.com/science/article/pii/S0168900214013552?via%3Dihub.

[49] A. Luccio et al. *Cold AGS Snake Optimization by Modeling.* C-AD Tech Note 128, 2003. URL https://technotes.bnl.gov/PDF?publicationId=32092.

[50] A. Luccio. *Booster Chamber Aperture.* Booster Tech Note 202, 1991. URL https://technotes.bnl.gov/PDF?publicationId=28844.

[51] C. Yu et al. AGS Booster Adjustment Report, 2015. Unpublished.

[52] N. Tsoupas et al. An AC Dipole for the AGS Booster to overcome spin resonances. In *Proceedings CAARI 2018 Conference.* Dallas, USA, 2018. URL https://aip.scitation.org/doi/pdf/10.1063/1.5127684.

[53] II Pelaia, Thomas. Parameter Estimation of Gaussian-Damped Sinusoids from a Geometric Perspective. *arXiv e-prints*, art. arXiv:1604.05167, April 2016.

[54] Rhodri Jones. Measuring Tune, Chromaticity and Coupling. Technical Report arXiv:2005.02753, CERN, May 2020. URL https://cds.cern.ch/record/

2723973. 19 pages, contribution to the CAS - CERN Accelerator School: Beam Instrumentation, 2-15 June 2018, Tuusula, Finland.

[55] K. Hock et al. AGS Dynamic Aperture at Injection of Polarized Protons and helions. In *Proc. 11th International Partile Accelerator Conference (IPAC'21), Campinas, Brazil, 24-28 May 2021*, May 2021.

[56] K. Hock et al. Simulations of AGS Boosters Imperfection Resonances for Protons and helions. In *Proc. 11th International Partile Accelerator Conference (IPAC'21), Campinas, Brazil, 24-28 May 2021*, May 2021.

[57] K. Hock et al. Scanning the AC Dipole Resonance Proximity Parameter in the AGS Booster. In *Proc. 10th International Particle Accelerator Conference (IPAC'19), Melbourne, Australia, 19-24 May 2019*, number 10 in International Particle Accelerator Conference, pages 2179–2181, Geneva, Switzerland, Jun. 2019. JACoW Publishing. ISBN 978-3-95450-208-0. doi: doi: 10.18429/JACoW-IPAC2019-TUPTS110. URL http://jacow.org/ipac2019/papers/tupts110.pdf. https://doi.org/10.18429/JACoW-IPAC2019-TUPTS110.

[58] K. Hock et al. Status of AC Dipole Project at Rhic Injectors for Polarized 3He, Update. In *Proc. 10th International Partile Accelerator Conference (IPAC'19), Melbourne, Australia, 19-24 May 2019*, number 10 in International Partile Accelerator Conference, pages 2177–2178, Geneva, Switzerland, Jun. 2019. JACoW Publishing. ISBN 978-3-95450-208-0. doi: doi: 10.18429/JACoW-IPAC2019-TUPTS109. URL http://jacow.org/ipac2019/papers/tupts109.pdf. https://doi.org/10.18429/JACoW-IPAC2019-TUPTS109.

[59] K. Hock et al. Status of AC-Dipole Project at RHIC Injectors for Polarized Helions. In *9th International Particle Accelerator Conference*, 6 2018. doi: 10.18429/JACoW-IPAC2018-TUPAF005. URL https://www.osti.gov/servlets/purl/1434780.